

**Fluidelastic Instability of Finned Tube Bundles
in Normal and Parallel Triangular Arrays**

**FLUIDELASTIC INSTABILITY OF FINNED TUBE BUNDLES
IN NORMAL AND PARALLEL TRIANGULAR ARRAYS**

By

Jing Wang, B.Eng.

A Thesis

Submitted to the School of Graduate Studies

in Partial Fulfillment of the Requirements

for the Degree

Master of Applied Science

McMaster University

©Copyright by Jing Wang, December 2008

MASTER OF APPLIED SCIENCE (2008)

(Mechanical Engineering)

McMaster University

Hamilton, Ontario

TITLE: Fluidelastic Instability of Finned Tube Bundles in Normal and Parallel Triangular
Arrays

AUTHOR: Jing Wang, B.Eng.

(Huazhong University of Science and Technology, P. R. of China)

SUPERVISOR: Professor D.S. Weaver

NUMBER OF PAGES: XVI, 52, -39-

To my wife Hao Zhou, two sons ZeXi and DongLe

ABSTRACT

Experimental study was conducted to investigate fluidelastic instability in finned tube bundles with normal and parallel triangular arrays. Three arrays of each geometry type were studied experimentally: two arrays with serrated, helically wound finned tubes of different fin densities, and a bare tube array with the same base diameter as the finned tubes.

The finned tubes under consideration were commercial finned tubes typically used in the fossil and process industries. For the purpose of the present investigation, the concept of “effective diameter” of a finned tube, as used to predict the vortex shedding, was used to compare the finned tube results with the existing bare tube world data and some theoretical predictions for fluidelastic instability.

The finned tube arrays in this study have the same tube pitch and have been scaled to have the same mass ratio and tuned to have the same natural frequency. A low speed wind tunnel, Betz micro manometer and HP 35670a dynamic signal analyzer were employed to conduct the experiments.

Experimental results for the triangular arrays show that the fin's structure strongly influences the fluidelastic stability of finned tube bundles and the fin pitch is demonstrated to reduce the difference in the fluidelastic instability between the tube arrangements as the fin density increases. The results also suggest that there might be an optimum fin pitch value at which the threshold reduced velocity for a finned tube array is much higher than the one for its corresponding bare tube array, due to the influence of fin geometry.

In the appendix, an analytical model produces a new correlation of critical reduced velocity

against mass damping parameter to predict the fluidelastic instability of tube bundles. Its predictions are in reasonable agreement with the experimental data. Since negative damping is one of the mechanisms of fluidelastic instability of a tube array, "Lift effect" was applied to explain the negative damping in an inviscid flow. An experiment is suggested to test the relationship between the pitch flow velocity and a tube velocity dependent "lift effect". Accordingly, two duct structure designs are suggested which may alleviate the negative damping by using the energy of oncoming flow to reduce the "lift effect" on the tubes.

ACKNOWLEDGEMENT

The author would like to sincerely thank his supervisor Dr. D. S. Weaver, for his considerate advice, guidance, and patient encouragement throughout the entire period of this project.

Appreciation also goes to the department technicians, Mr. Ron Lodewyks, Jim McLaren, and Joe Verhaeghe.

Special thanks are also expressed to Mr. Robert H. Lumsden , Dr. Honda Wang, and Dr. Kareem Awny Aly for their kind help and advice in the preparation of experiments.

The author is also grateful for the FIV group members: Dr. S. Ziada, Dr. S. Tullis, Ahmed Khalifa, Kevin McLaren, and many more, for their questions and suggestions for his presentation and thesis.

Acknowledgement is also due to the financial support of NSERC, and Frank Eisinger & Foster Wheeler Power Group, Inc. for supplying the tubes for this study.

TABLE OF CONTENTS

CHAPTER 1	Introduction.....	1
CHAPTER 2	Literature Review on Fluidelastic Instability	6
2.1	Fluidelastic Instability.....	6
2.2	Previous Finned Tube Studies.....	10
CHAPTER 3	Experiment on Fluidelastic Instability in Finned Tube Bundles.....	19
3.1	Finned Tubes and Tube Arrangements.....	19
3.2	Dynamic Similarity.....	21
3.3	Calibration of Strain Gages.....	29
3.4	Measurement and Calculation of Damping and Natural frequency.....	31
3.5	Instruments and Procedures of Experiment.....	35
CHAPTER 4	Results and Discussion.....	41
4.1	Experimental Results.....	41
4.2	Comparisons with World Data.....	42
CHAPTER 5	Conclusions and Recommendations.....	50
	References.....	51
Appendix A	Modeling of FluidElastic Instability in Finned Tube Bundles in Staggered Arrangement.....	-1-
	A1 One Dimension Unstable Flow of Incompressible Ideal Fluid.....	-1-
	A2 Fluidelastic Instability Simulation.....	-2-

A3 Fluidelastic Vibration Equation (FVE).....	-3-
A4 Fluidelastic Instability in Finned Tube Bundle in Staggered Arrangement ...	-13-
A5 Numerical Method to FVE.....	-19-
A6 Comparisons with Present Analytical Model and Other Empirical Formula	-22-
A7 Lift Effect and Negative Damping Alleviation Experiments.....	-25-
A8 Conclusions and Recommendations.....	-27-
Appendix B C Code for FVE.....	-29-
Appendix C APDL Mac Code for Modal Analysis of Finned Tubes.....	-33-
Appendix D Calibrations for Strain Gages.....	-37-

Table of Figures

Figure 1-1 Phenomenon of Fluidelastic Instability.....	2
Figure 1-2 Fluidelastic Stability Thresholds for Heat Exchanger Tubes.....	3
Figure 2-1 Tube Array Pattern Definitions.....	7
Figure 2-2 Structures of Finned Tubes.....	12
Figure 2-3 Photos of Finned Tubes Under Investigation.....	13
Figure 2-4 a) In-Line Square Arrangement.....	18
Figure 2-4 b) Rotated Square Arrangement.....	18
Figure 3-1 Triangle Arrangements.....	22
Figure 3-2 Base Plate Structure.....	23
Figure 3-3 Finned Tube Structure in ANSYS.....	25
Figure 3-4 Hybrid Mesh.....	27
Figure 3-5 Fundamental Mode of Finned Tube.....	28
Figure 3-6 Determination of Frequency And Rod Height.....	28
Figure 3-7 Test Tube Support and Monitored Tubes.....	29
Figure 3-8 Strain Gage Calibration.....	30
Figure 3-9 Peak Fitting for Damping Factor Calculation.....	32
Figure 3-10 Natural Frequency.....	33
Figure 3-11 Schematic Diagram for Tuning Tubes.....	34
Figure 3-12 Correction Between Betz And Pressure Transducer.....	35
Figure 3-13 Betz Reading.....	36
Figure 3-14 Hp 35670a Dynamic Signal Analyzer.....	37
Figure 3-15 Wind Tunnel System for FEI.....	40
Figure 4-1 Rms Amplitude/ D_{eff} vs. Reduced Velocity of Bare Tubes.....	43
Figure 4-2 Rms Amplitude/ D_{eff} vs. Reduced Velocity of Coarse Finned Tubes.....	44
Figure 4-3 Rms Amplitude/ D_{eff} vs. Reduced Velocity of Fine Finned Tubes.....	45

Figure 4-4 Normal Triangle Array in World Data.....	46
Figure 4-5 Parallel Triangle Array in World Data.....	47
Figure 4-6 Critical Reduced Velocity vs. Effective Pitch Ratio.....	48
Figure 4-7 Schematic Velocity Profile of Finned Tube.....	49
Appendix:	
Figure A-1 Fluidelastic Instability Simulation.....	-3-
Figure A-2 Sub-Domains of Left and Right Channels.....	-4-
Figure A-3 Lift Effect Due to Tube Velocity.....	-15-
Figure A-4 Influence of Tube Array Geometry on Coefficient β	-17-
Figure A-5 Triangular Tube Array	-21-
Figure A-6 Some Numerical Computation results.....	-22-
Figure A-7 Experimental Data vs. Analytical Model and Empirical Equations.....	-24-
Figure A-8 Schematic Diagram of Lift Effect Experiment.....	-25-
Figure A-9 Test Section of Platen Finned Tube Array.....	-26-
Figure A-10 Critical Velocities of Smooth Tubes and Platen Finned Tubes.....	-26-
Figure A-11 Duct Jet Flow	-27-
Figure C-1 Calibration of Strain Gages for Bare Tubes.....	-37-
Figure C-2 Calibration of Strain Gages for Coarse Finned Tubes.....	-38-
Figure C-3 Calibration of Strain Gages for Fine Finned Tubes.....	-39-

Table of Tables

Table 3-1 Geometry and Mass Parameters of Tubes.....	20
Table 3-2 Fin Geometries.....	20
Table 3-3 Specifications of Triangle Arrangements.....	21
Table 3-4 Mass Parameters of Tubes.....	24
Table 3-5 Tube Mass, Material Property and Geometry in ANSYS.....	26
Table 3-6 Frequency and Rod Height Evaluated by Concentrated Mass.....	26
Table 3-7 Summary of ANSYS Model.....	27
Table 3-8 Frequency and Rod Height Computed by ANSYS.....	27
Table 3-9 Converting Coefficients of Amplitude vs. Voltage.....	31
Table 3-10 Natural Frequency and Damping of Tube.....	33
Table 4-1 Critical Reduced Velocity vs. Damping Parameter.....	42
Appendix:	
Table A-1 Specifications for Numerical Computation.....	-20-
Table A-2 Equations for Prediction.....	-22-
Table A-3 Parameters for Current Analytical Model.....	-23-
Table A-4 Model Predictions.....	-23-

Nomenclature

A	Cross sectional area or amplitude of vibration
a	$D/(P-D)$
b	$(P-D\cos(\theta))/P-D$
C	Damping or time dependent constant
c	Damping of tube, $c=2m\zeta\omega$, $kg/m.s$ or constant
D	Characteristic length, diameter, m
D_b	Base or bare tube diameter, m
D_{eff}	Effective diameter, m
D_f	Fin diameter, m
Dis	Fluidelastic force component
E	Young's Modulus, or related constant
F	Force on tube
f	Natural frequency of the tube, Hz , or function
H	Longitudinal tube pitch, m , or tube height, m
H/D_{eff}	Streamwise tube pitch ratio
h	Fin height, m , or internal tube height, m
I	Second moment, m^4
K	Proportionality constant
k	Stiffness or spring constant of tube per unit length, $kg/m.s^2$ or N/m^2
k	Dimensionless displacement
k_f	Dimensionless stiffness of fluid
\tilde{l}	Total length of path line, m
l_m	Straight length of path line, m
l_θ	Arc length of path line, m
m	Tube mass per unit length, kg/m

p	Fin pitch, m
P	Pressure, Pa or Transverse tube pitch, m
P	Function related to harmonic linearization method
P/D_{eff}	Transverse tube pitch ratio
Q	Mass flux, kg/s or function related to harmonic linearization method
r	Tube radius, m
s	A tiny constant
t	Fin thickness, m , or time, s
U	Flow velocity, m/s
U_{crit}	Critical velocity, m/s
U_g	Gap velocity of air flow, m/s
U_p	Pitch velocity, m/s
U_u	Upstream velocity, m/s
v	Voltage value of strain gage, v
Vel	Dumping component
w	Fin serration width, m
X	Tube coordinate in x direction, m
x	Tube velocity, m/s
x, y	Tube displacements of x, y direction, m , or function variable
x_c/D_{eff}	Tube amplitude ratio

Greek

ψ	Gravity potential or (τ - ϕ)
ϕ	Initial phase
β	Coefficient
ν	Frequency of fluidelastic force, Hz
λ	Ratio of frequency of fluidelastic force vs. frequency of tube, ν/ω

τ	Dimensionless time, $t\omega$
σ	Poisson ratio
θ, ϑ	Pressure acting angle, rad
$\hat{\alpha}, \hat{\beta}$	Dimensionless generalized displacements
ΔP	Pressure drop, Pa
δ	Logarithmic decrement of damping
ζ	Damping factor, $\zeta = \delta/2\pi$
ρ	Fluid density, kg/m^3
ω	Natural frequency of tube in radians per second, $\omega = 2\pi f = \sqrt{k/m}$, $1/s$

Subscript and Superscript

\wedge	Dimensionless item
\cdot	First order derivative
0	Initial or reference point
$1, 2, 3, 4$	Number
a	Added mass
b	Bare
C	Center
c	Coarse tube finned tube
CE	Center east
$crit$	Critical
CW	Center west
d	Damping
E	East
eff	Effective
f	Fin or Fine finned tube or function
g	Tube gap or strain gage

<i>l</i>	Left
<i>m</i>	Mean
<i>N</i>	North
<i>n</i>	Natural frequency or iteration number
<i>NE</i>	North east
<i>NW</i>	North west
<i>p</i>	Pitch
<i>r</i>	Right or rod
<i>t</i>	Thickness
<i>vol</i>	Volume
<i>W</i>	West
<i>x, y</i>	Directions in x and y

Chapter 1

INTRODUCTION

Heat exchangers are widely used in space heating, refrigeration, air conditioning, petrochemical plants, automotive, natural gas processing, and nuclear power plants, etc. The types of heat exchangers are multifarious as well, including compact heat exchangers, plate heat exchangers, heat pipes, shell and tube heat exchangers, and so on. Investigations have studied almost all aspects of them, including thermodynamics, fluid mechanics, materials, and manufacturing, etc. Amongst these studies are some specifically focusing on fluid induced vibration in shell and tube heat exchangers, which has been paid increased attention particularly in nuclear power generation and oil processing industries over the last forty years.

In the study of flow-induced vibrations, fluidelastic instability plays a vital role due to its destructive potential to heat exchangers, like the CANDU steam generators. Were a failure to occur, damage to the security and operation of the nuclear equipment would be huge and the repair would be expensive and time consuming for there are thousands of tubes. The phenomenon of fluidelastic instability is characterized by an abrupt rise in dynamic response of tubes for a small increment in flow velocity across tube bundles. Figure 1-1 illustrates the relationship between the tube vibration response and fluid flow velocity. The x-axis is flow velocity while the y-axis is the RMS vibration response amplitude of tube. When the fluid passes by the tube, the tube will be subjected to unsteady fluid-dynamic forces and prone to vibrations. The turbulent buffeting response will increase as the fluid velocity increases. Once the velocity reaches a critical value, the fluidelastic instability will occur. Above this critical velocity, failure of the tube may be rapid and catastrophic. Therefore, fluidelastic instability should be strictly avoided by designers of tube and shell heat exchangers.

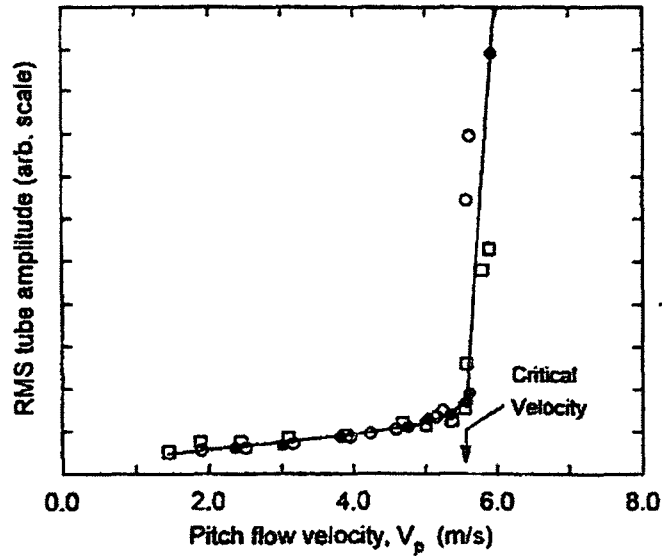


Figure 1-1 Phenomenon of Fluidelastic Instability^[1]

A full understanding of the mechanisms involved in fluidelastic instability is still not available even though investigation in tube arrays has been ongoing for four decades and much research has been conducted. Currently, most designers must depend on experience and empirical data from laboratory studies to design their heat exchangers. Once their new designs differ from those of experimental facilities, there is an increased risk of failure due to fluidelastic instability. Although several theoretical models have been developed, their predictions of the critical velocity are imperfect and do not provide reliable design guidance. On the other hand, numerical techniques have not proven capable of solving general, fully coupled flow-induced vibration problems at practical Reynolds numbers at the present time^[1]. Therefore, the prediction of critical velocity, in most cases, still depends on the available experimental data. Figure 1-2 shows the ASME design guideline^[2]. Based on published data and some analytical models, a semi-empirical relationship generalized from that suggested by Connors^[3].

$$\frac{U_g}{fD} = K \left(\frac{m\delta}{\rho D^2} \right)^\alpha \quad (1-1)$$

where U_g is the so-called pitch velocity, $U_g = [P/(P - D)]U_u$, P is the tube pitch, U_u is the flow

velocity upstream of the tube bundle, f is the natural frequency of the tube, D is the tube diameter, m is the mass per unit length of the tube including fluid added mass, ρ is the density of the fluid in cross flow and δ is the logarithmic decrement of damping. The empirical constant, K , has a mean value of 4.0 and a suggested lower-bound value of 2.4 based on world data. The exponent constant, α , is assigned a value of 0.5 in the ASME guideline.

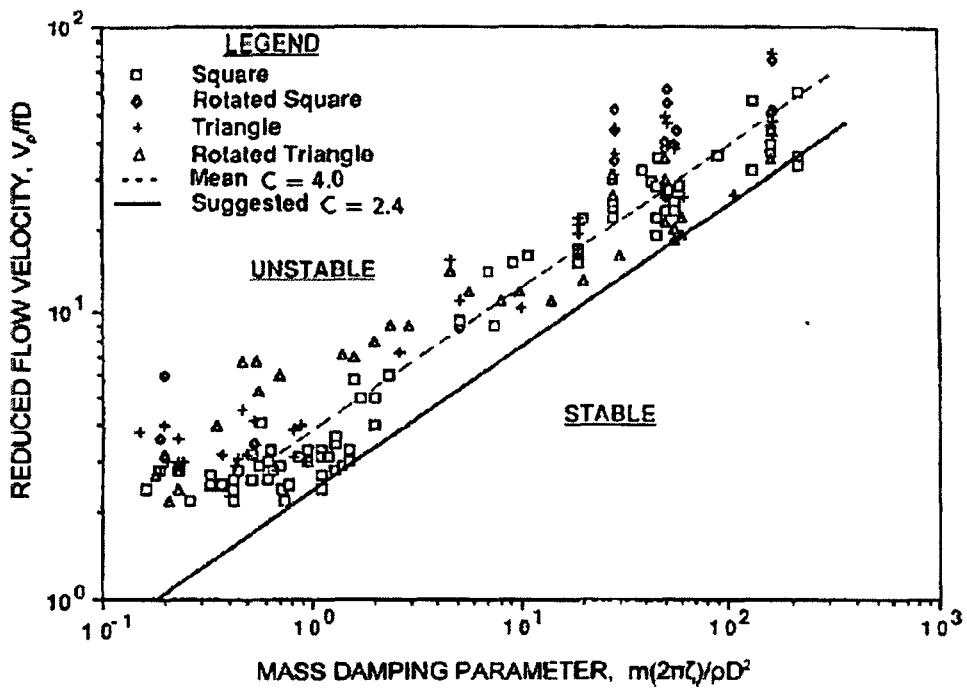


Figure 1-2 Fluidelastic Stability Thresholds for Heat Exchanger Tubes [2]

For most practical applications, the Connors' equation and its variants will provide conservative estimates of critical velocity for fluidelastic instability. The world data are under continuous revision as more and more data is published.

The present study deals with fluidelastic instability in finned tube bundles, which have rarely been investigated in the past. This thesis presents experimental and theoretical studies on the fluidelastic instability of finned tube bundles in normal and parallel triangular arrays. Three

arrays of each geometry type were studied, two arrays with serrated, helically wound finned tubes of different fin densities, and a bare tube array with the same base diameter as the finned tubes. The finned tubes under consideration were commercial finned tubes typically used in the fossil and process industry. The addition of fins to tubes in heat exchangers augments heat transfer as the total surface area is increased and the turbulence in the tube bundle. In the case of flow-induced vibration, since the serrated fins interrupt the boundary layer which otherwise tends to develop from laminar layers to thicker turbulent layers, one might expect suppression of vortex shedding.

Almost no studies, however, investigating the influence of fin structure on the fluidelastic instability of tube bundles, have been published. This study was undertaken to overcome this deficiency. For the purpose of the present investigation, the “effective diameter” of a finned tube, as applied to predict the vortex shedding, is also used to compare the finned tube results with the existing bare tube world data for fluidelastic instability. The finned tube arrays in the present study have the same tube pitch, and have been scaled to have the same mass ratio and tuned to have the same natural frequency. A low speed wind tunnel, Betz micro manometer and HP 35670a digital signal analyzer were employed in this experiment of fluidelastic instability.

This thesis consists of five chapters. The first chapter, the introduction, gives the motivation and an overview of the thesis. The second chapter is a literature review, which introduces papers investigating fluidelastic instability and related research results for finned tubes. Chapter three describes the experiment preparation and the testing procedure. The testing equipment employed in the experiments and the methods used to obtain and analyze the results are also introduced in this chapter. Chapter four presents the experimental results. Comparisons between these results and the world data, as well as comparisons between these results and predictions by the newly developed correlation and other available semi-empirical equations are included in this chapter. Related discussions are also presented there. Chapter five contains conclusions based on the

experimental and analytical results from this project and recommendations for future work.

In the appendix, the author also developed a simplified mathematical model for predicting the fluidelastic stability of finned tube bundles based on the fluid inertia assumption suggested by Lever and Weaver^[4]. Finned tubes are taken into account in the model by applying the concept of effective diameter. A new fluidelastic vibration equation was derived and the characteristics of this equation were analyzed in a tube array with a single flexible tube. Consequently, a new correlation is developed to predict the threshold reduced velocity of tube bundles. The comparison between the experimental data and the current prediction is also conducted. "Lift effect" was applied to explain the negative damping in an inviscid flow. Experiments were recommended to validate this "lift effect" and related alleviation methods

Chapter 2

LITERATURE REVIEW ON FLUIDELASTIC INSTABILITY

There are many ways for fluid to cause structural vibration. Turbulence buffeting, vortex shedding, oscillating flow, and many other fluid flow behaviors may produce structural vibrations. Basically these vibration behaviors are generated by a particular fluid flow feature which can be clearly observed in practical conditions. However, there is a vibration phenomenon which can hardly be observed from the fluid flow but which can be clearly demonstrated by the dynamic response of structure. This phenomenon, caused by fluid-structure interaction, is called fluidelastic instability. Fluidelastic instability occurs once a critical flow velocity is exceeded in relation to a structure, like a cross-flow tube bundle. Periodic fluid forces cause by the structural response feed energy into the structure and this feedback mechanism can cause rapid growth of the vibration amplitude. In practical applications, flow induced vibration can cause minor damage in tube bundles over a long period of time, due to turbulent buffeting or vortex shedding, or they can produce high levels of noise because of acoustic resonance. But, none of these compare to the failures caused by fluidelastic instability. Fluidelastic instability causes the vibration amplitudes of the tubes to dramatically increase with slightly increasing flow velocity. The destructive potential of this instability to tube bundles is serious and rapid. Consequently, studies of this catastrophic instability have increased over the past forty years.

2.1 Fluidelastic Instability

Connors^[3] (1970) published experiments on a single row of cylinders. He examined the dynamic response of one of the cylinders to the applied fluid loading change due to the displacement of the cylinder and its immediate neighbors from their original positions. This “displacement mechanism” is now thought to be one of the mechanisms of fluidelastic instability.

Connors' experiments yielded the relationship for this mechanism shown in equation 1-1. Different from the empirical constants in Chapter One, Connors suggested $K = 9.9$ and $\alpha = 0.5$ at the very beginning of his study, as a result of his experiments on a single row of cylinders and using the upstream velocity (U_u) as the critical velocity. But Chen and Jendrzejczyk [5] emphasized the importance of negative damping as a component of the fluidelastic excitation mechanism. Much subsequent research has been conducted to examine fluidelastic instability and its prevention in various tube pattern arrangements, which are widely applied in commercial heat exchangers as shown in figure 2-1 [2].

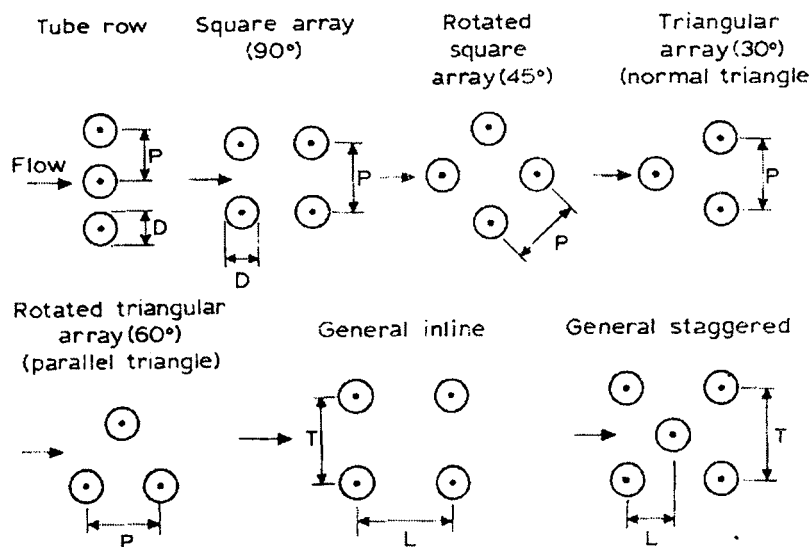


Figure 2-1 Tube Array Pattern Definitions [2]

In 1981, research by Weaver and ElKashlan [6] studied the number of rows required to simulate fluidelastic instability in a heat exchanger. The results suggested the number of rows to be 5~6 in depth, which indicated that the early results of Connors did not really reflect the fluidelastic effect in a tube bundle. Further, after an investigation on the use of Connors' equation to predict fluidelastic instability in cylinder arrays, Price [7] concluded that there were many deficiencies associated with Connors' equation and that more emphasis must be put on examining the physics of fluidelastic instability. Although the exact form of Connors' equation has been a subject of much debate, the non-dimensional parameters used by Connors are still used today for

the study of fluidelastic instability in tube arrays. The critical velocity commonly used for tube arrays is the gap velocity (U_g), which is the mean velocity in the gap between tubes:

$$U_g = U_u \frac{P}{P - D}$$

where U_u is the upstream velocity, P is the tube pitch, and D is the tube diameter.

In 1988, Weaver and Fitzpatrick^[8] reviewed the state of understanding of the cross flow excitation mechanisms and presented design guidelines. They concluded that flow induced vibrations are widely recognized as a major concern in the design of modern tube and shell heat exchangers. Tube failures caused by excessive vibrations are relatively commonplace and often very expensive to repair. They admitted that although considerable progress has been made in the development of predictive tools, many uncertainties still remained.

Theoretical Models of Fluidelastic Instability

Besides the Connors' equation, which is called as the quasi-static-flow theory used by Connors and Blevins, Weaver and his co-authors^[1] summarized other efforts in modeling fluidelastic instability, including quasi-steady-flow theory and unsteady-flow theory.

In 1986, Lever and Weaver^[4] published a theoretical model from first principles for cross flow induced fluid elastic instabilities in heat exchanger tube bundles. Their theory was reported to have been modified and extended from their previous studies to treat static divergence as well as fluidelastic stability in both stream wise and transverse directions to the flow. The mechanism responsible for transverse dynamic instability was proposed to be one of flow redistribution with a phase lag. The model includes the effects of tube array pattern and pitch. Theoretical descriptions of heat exchanger instability mechanisms developed by other authors are compared and contrasted with their model. This model was developed based on a tube array with one single flexible tube.

In 1993, Yetisir and Weaver ^[9] published an unsteady theoretical model for fluidelastic instability in an array of tubes in cross-flow. The model is based on concepts developed by Lever and Weaver, but is extended to overcome some of the problems encountered with that earlier work. A perturbation decay function is introduced to account for decay of disturbances away from a moving tube, and the theory includes the effects of neighboring tube motion. The theory is applicable to all standard array geometries and is shown to reduce to a model of a single flexible tube in a rigid array which includes static instability as a special case.

S.J. Price ^[10] reviewed all known theoretical models of fluidelastic instability for cylinder arrays subject to fluid cross-flow in 1995. Particular emphasis was given to the physics of the different instability mechanisms, and the assumptions made are analyzed and discussed. The comparisons are made between the models, and with available experimental data; these comparisons are in terms of the critical flow velocity at which instability occurs and of the sub-critical response of cylinders in the array. Despite the considerable differences in the theoretical models, there is some agreement in the general conclusions obtained. In particular, it is shown that the most important parameter for predicting fluidelastic instability is the unsteady nature of the interstitial flow in the array, specifically, the phase-lag between cylinder motion and fluid forces generated thereby. The author evaluates methods appropriate for using the analyses, which are predominantly two-dimensional in nature, to predict the stability of three-dimensional heat exchanger spans subject to non-uniform flow. Finally, the effect of nonlinearities, both structural and fluid, on the post-instability behavior is discussed.

New design equations were presented by K. Schröder and H. Gelbe ^[11] in 1999 to determine the critical velocities for the occurrence of fluidelastic instability in uniform single-phase cross flow. Six existing guidelines for fluidelastic instability were tested and compared with approximately 300 experimental data from 34 papers. Schröder and Gelbe's new design equations

for the stability factor K and mass damping parameter exponents as a function of the pitch ratio for different tube configurations were derived using statistical methods. They found that the pitch ratio has the strongest influence on the normal triangular array and the influence becomes less for the rotated square configurations as well as for the in-line square configurations. This significant gradation of the stability constants as a function of the pitch ratio and the tube bundle configuration enables a reasonable interpolation for non-standard configurations.

CFD Modeling for Fluidelastic Instability

CFD methods involving the numerical solution of the Navier-Stokes equations with moving boundary conditions and their interactions with structures have also been applied to simulate fluid-induced vibrations. However, according to Weaver and his coauthors ^[1], commercial CFD codes have not proven capable of solving general, fully coupled flow-induced vibration problems at practical Reynolds numbers at the present time.

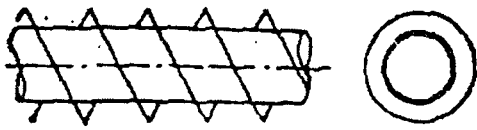
2.2 Previous Finned Tube Studies

The history of studies on fluidelastic instability spans forty years and most research focuses on the fluidelastic instability of arrays of bare tubes. Experimental fluidelastic threshold studies for finned tubes seem to be rare, and accordingly, few papers for finned tubes are to be found. However, a significant number of industrial heat exchangers are composed of finned tubes in order to enhance heat transfer. As finned tubes have been adopted for their increased heat transfer performance, researchers have attempted to use the concept of “effective diameter” which will allow the users of finned tubes to convert their finned tube into an equivalent bare tube. This would permit the heat exchanger designers to make use of the existing bare tube data available to predict the response of finned tubes. However the heat exchanger designers may still take a risk because of the lack of direct experimental data for finned tubes if the finned tube bundles have lower stability than the bare tubes. Alternatively, they may design heat exchangers with excessive conservatism if the finned tubes have higher stability than the corresponding bare tubes.

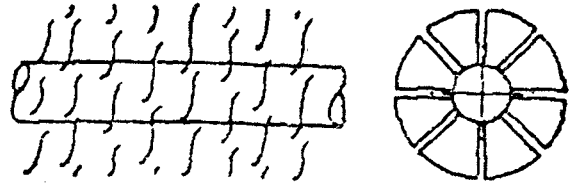
Serrated, Helically Wound Finned Tubes

Warren M. Rohsenow, et al. ^[12] introduced various finned tubes in their handbook of heat transfer applications shown in figure 2-2. The heat transfer and flow friction characteristics of these finned tubes including plate finned tubes, offset strip finned tubes, perforated finned tubes, waved finned tubes, and spiral wired tubes are discussed by introducing related published literature. Kays and London ^[13] provided heat transfer factor, j , and flow friction factor, f , for eight sets of bare tubes and fourteen sets of plate finned tubes in different arrangements. But neither paper mentioned the concept of effective diameter.

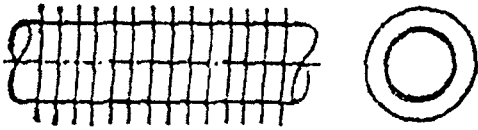
In the early 1970s, ESCOA (Extended Surface Company of America, now part of Fintube Corp.) introduced the serrated, helically wound finned tube to the American marketplace. The tubes use high frequency resistance welding which reduces the overall weld size and therefore allows for tighter fin pitches to be produced. The pre-serration of the strip of fins means no crimping or stretching of the strip before welding is required so the maximum fin height is much less restricted by the manufacturing process, unlike plain helical finned tubes. Heat Recovery Steam Generators (HRSG) are major users of this technology. The fin pitch used depends on the fluid used in cross flow; the decision is based on the amount of particulate in the flow which can clog up the gap between fins during operation. According to Reid and Taborek ^[14], the finned tubes are suggested for: heavy oil combustion (8.4mm or 3.3 fins per inch), and natural gas and light oil combustion (4.2mm or 5.7 fins per inch) as shown in Figure 2-3. These two types of finned tubes are investigated in this study.



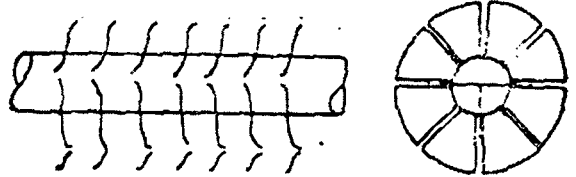
helical plane fin



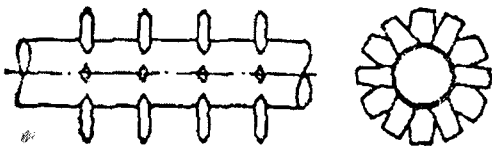
helical and fully serrated fin



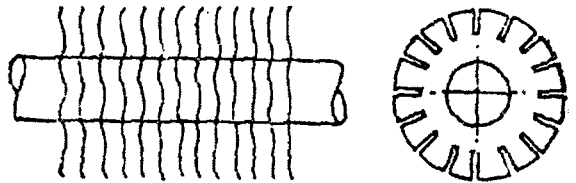
plane fin



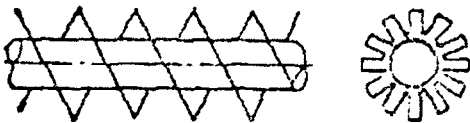
waved and fully serrated fin



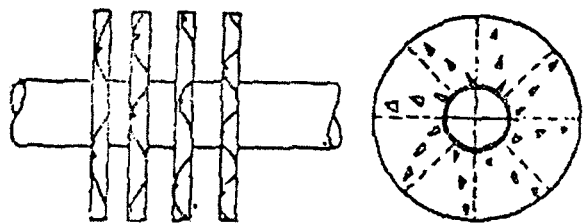
stud fin



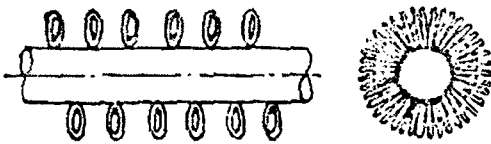
waved and half-serrated fin



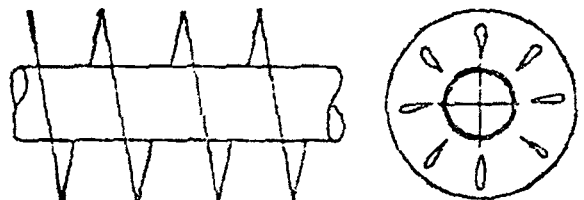
offset strip fin



waved fin with wedge holes

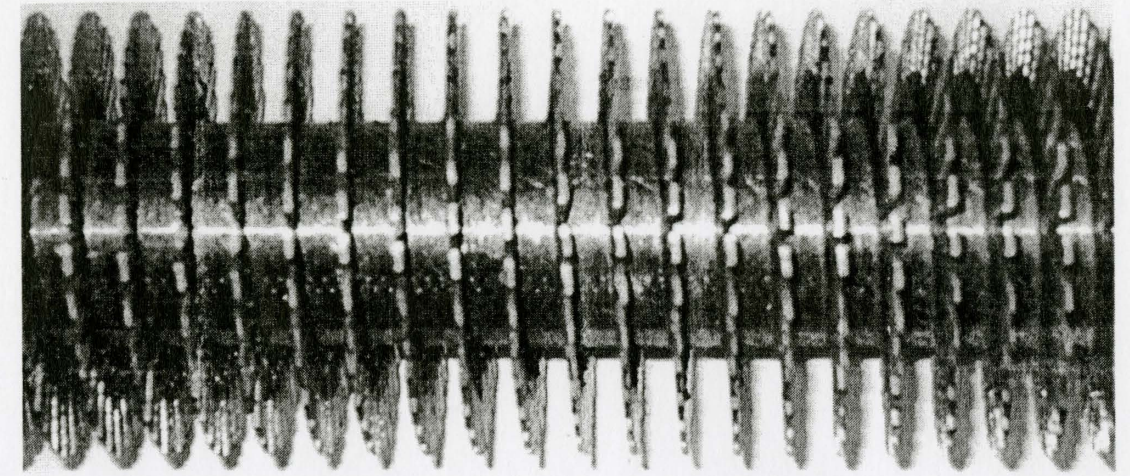


spiral wired fin

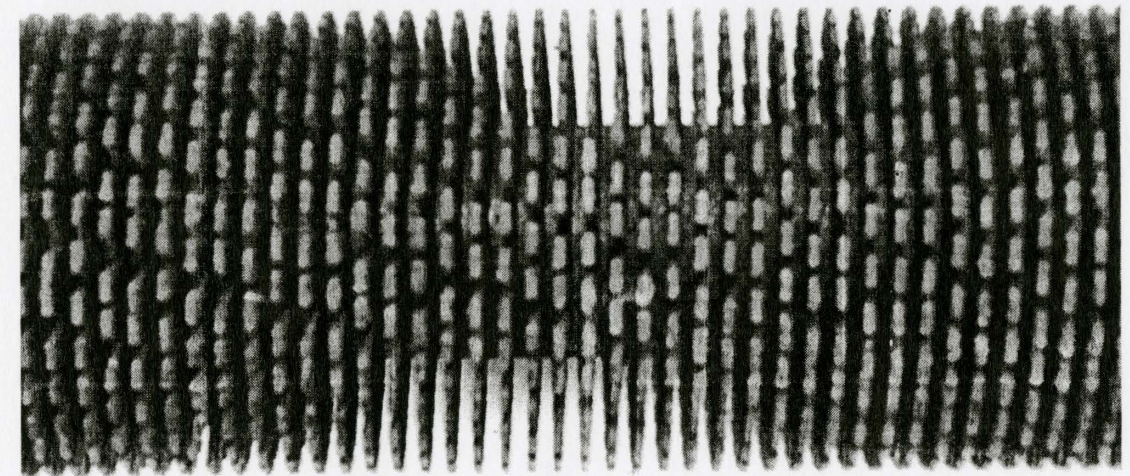


helical perforated fin

Figure 2-2 Structures of Finned Tubes ^[12]



a) Coarse Finned Tube (8.4mm/3.3 fpi)



b) Fine Finned Tube (4.2mm/5.7 fpi)

Figure 2-3 Photos of Finned Tubes under Investigation

Effective Diameter

There are at least two different models suggested for the effective diameter, D_{eff} , of finned tubes. The first is based on the projected area of the finned tube. This model was at the earliest suggested by Mair and his coworkers^[15]. In their paper, the finned tube was regarded as an equivalent bare tube, the effective diameter of which is given by this equation.

$$D_{eff} = D_b + \frac{t(D_f - D_b)}{p}$$

where p is the fin pitch, t is the fin thickness, D_f is the fin diameter, and D_b is the base tube diameter.

The second model is recommended by Hirota and his coworkers^[16]. They suggested using a volumetrically-based effective diameter, as the characteristic length for fluidelastic instability in the form of:

$$D_{vol} = \sqrt{\left(D_f^2 - D_b^2\right) \frac{t}{p} + D_b^2}$$

Effect of Serrated Fins on Vortex Shedding from Circular Cylinder

An experimental study was performed by Ryu and his coworkers^[17] to investigate the characteristics of near wake flow behind a circular cylinder with serrated fins using constant temperature anemometer and flow visualization. Various vortex shedding modes were observed. Fin height and pitch are closely related to the vortex shedding frequency after a certain transient Reynolds number. The through-velocity across the fins decreases with increasing fin height and decreasing fin pitch. Vortex shedding is affected strongly by the velocity distribution just on top of the finned tube studied. The weaker gradient of velocity distribution is shown as increasing the free stream velocity and the fin height, while decreasing the fin pitch. The weaker velocity gradient delays the entrainment flow and weakens its strength. As a result of this phenomenon, vortex shedding is decreased. The effective diameter is defined as a virtual circular cylinder diameter taking into account the volume of fins, while the hydraulic diameter is proposed to cover the effect of friction by the fin surfaces. The Strouhal number based upon the effective diameters seems to correlate well with that of a circular cylinder without fins. After a certain transient Reynolds number, the trend of the Strouhal number can be estimated by checking the ratio of effective diameter to inner diameter. The normalized velocity and turbulent intensity distributions with the hydraulic diameter exhibit the best correlation with the circular cylinder's data.

The investigation conducted by Mair *et al.* shows that the effective diameter predicts vortex shedding over plain finned tubes (no helical winding, no serration) quite well, and the model is also proven by Ryu to be sufficient for predicting vortex shedding from serrated, helically wound finned tubes.

Fluidelastic Instability in Finned Tubes

Studies relating to fluidelastic instability in actual finned tube bundles are rare. Kienböck^[18] and Halle *et al.*^[19] conducted investigations into this issue but the finned tubes used had very short fins compared to their diameter ($h/D_b = 6.6\%$ and 10% respectively, where h is the fin height). The most recent published papers which represent an array of modern industrial finned tubes are from Lumsden and Weaver^{[20][21]} in 2006 and 2007. They investigated tubes with an $h/D_b = 50\%$. The experiments were conducted to study fluidelastic instability in in-line and rotated square finned tube arrays. Coarse finned tubes (8.4mm/3.3fpi), fine finned tubes (4.2mm/5.7fpi), and bare tubes were considered. The tube pitch and mass ratio were kept constant. In these papers, fluidelastic instability was demonstrated in in-line and rotated square arrays of modern finned tubes for the first time. Figure 2-4 shows Lumsden and Weaver's results compared to the world data (critical reduced velocity vs. mass damping parameter). Figure 2-4-a) for the in-line square arrangement shows that the finned tubes have much higher critical reduced velocity than the bare tubes: the critical reduced velocity for the referenced bare tube is below twenty, but the one for the finned tubes is around fifty. Figure 2-4-b), however, which is for the rotated square arrangement, shows that the referenced bare tube has a higher value of around sixty while the finned ones have regular values from thirty to forty.

Although the Hirota's definition for the volumetric effective diameter is different from the effective diameter suggested by Mair *et al.*, the difference between the two values is between four and six percent for the finned tubes under Lumsden and Weaver's investigation (note that both

definitions were derived for plain finned tubes, and more detailed specifications, like fin serration width and height, are not included). In their paper, Lumsden and Weaver concluded that the effective diameter suggested by Mair et al. appears appropriate in the scaling of fluidelastic instability in finned tube arrays. The critical velocity in in-line arrays is substantially delayed by the addition of serrated fins, even though their effect is to significantly reduce the effective pitch ratio, P/D_{eff} . The stability threshold also becomes less clearly defined as the fin density increases. In rotated square finned tube arrays, the addition of fins appears to increase the coupling between neighboring tubes and the stability threshold is reduced and becomes more clearly defined. This could be accounted for in part by the reduction in the effective pitch ratio. Lumsden and Weaver's investigation suggests that the effect of fins on fluidelastic instability is strongly dependent on tube array geometry, and more research is called for to determine the effect of tube array pitch and pattern.

Prediction of Fluidelastic Instability in Finned Tube Arrays

In the appendix of this thesis, a theoretical model is introduced to analyze the fluidelastic instability of finned tube bundles. As noted in the previous section, there is no theoretical model to predict the stability of finned tube bundles. To address this lack, the author developed a mathematical model to predict the critical velocity of finned tube bundles in staggered arrangement. This fluidelastic instability theory was transcribed from the author's project report for the course, Flow Induced Vibrations (ME723), at McMaster University in 2008. The origin of the methodology is from the semi-analytical model developed by Lever and Weaver^[4], but there are significant differences between these two models: in the new model all the tubes are flexible and oscillate only in transverse direction; the tube array is a staggered arrangement; the fluid flow channel is composed of several simple sub-domains where fluid flow is treated using different strategies; and tube fins are taken into account in terms of an effective diameter. The analytical model produces a new correlation of critical reduced velocity against mass damping parameter to predict the fluidelastic instability of tube bundles. Its predictions are in reasonable agreement

with the experimental data. Since negative damping is one of the mechanisms of fluidelastic instability of a tube array, "Lift effect" was applied to explain the negative damping in an inviscid flow. An experiment is suggested to test the relationship between the pitch flow velocity and a tube velocity dependent "lift effect". Accordingly, two duct structure designs are suggested which may alleviate the negative damping by using the energy of oncoming flow to reduce the "lift effect" on the tubes.

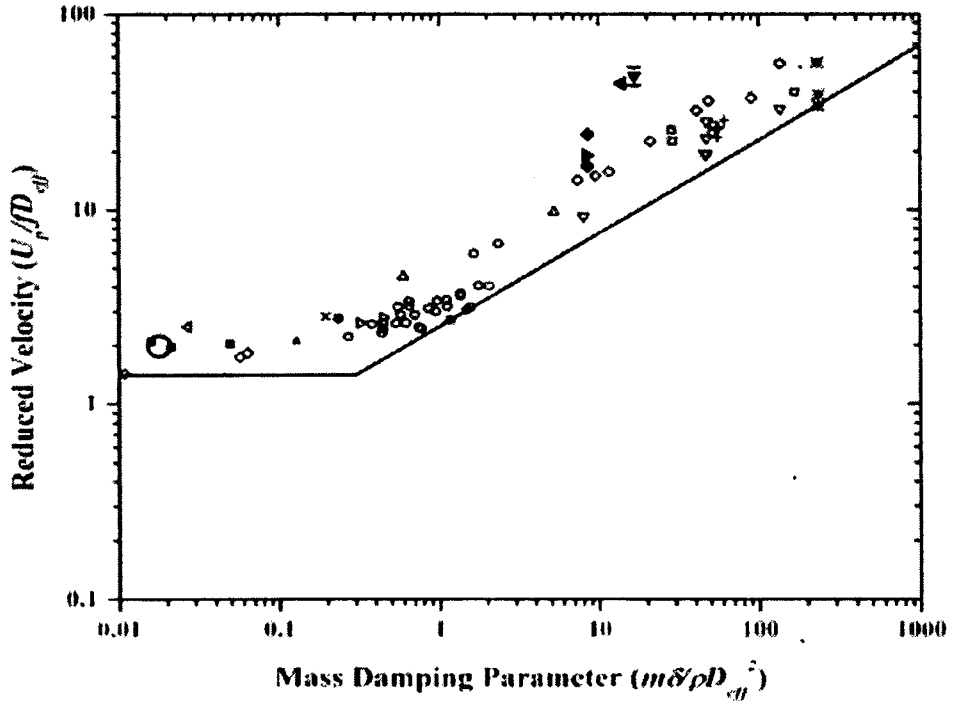
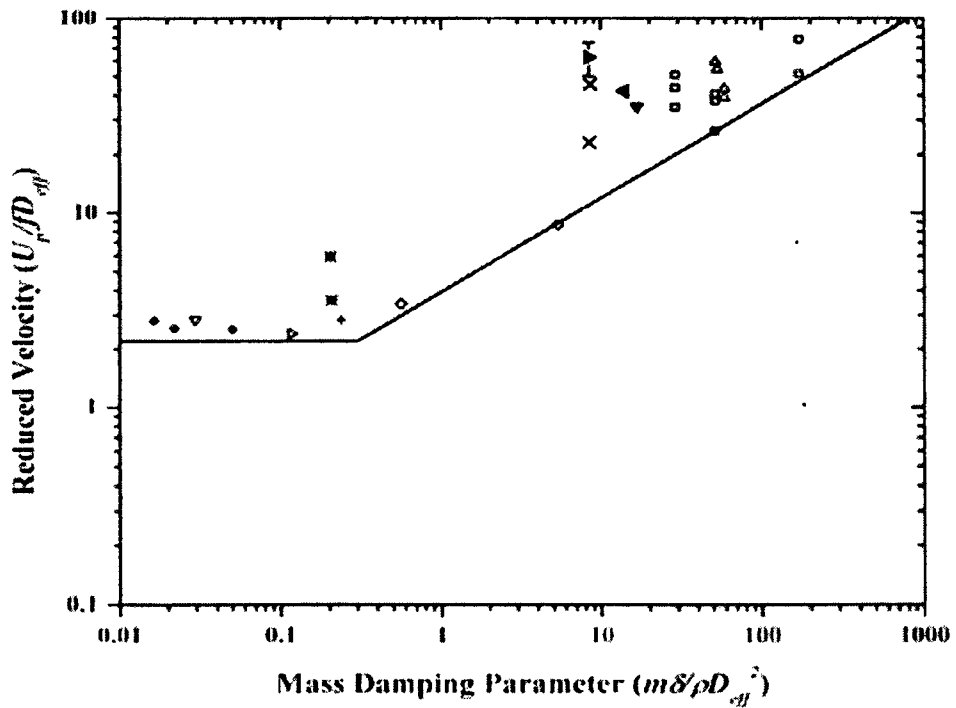


Figure 2-4 a) In-Line Square Arrangement



► Bare, ◄ 3.3 fpi, ▼ 5.7 fpi

Figure 2-4 b) Rotated Square Arrangement ^[21]

Chapter 3

EXPERIMENT ON FLUIDELASTIC INSTABILITY IN FINNED TUBE BUNDLES

3.1 Finned Tubes and Tube Arrangements

The two kinds of steel finned tubes under investigation in this study are manufactured by Biraghi Canada (a subsidiary of Fintube Corp.) of Bécancour, Quebec, Canada. The fin pitches of the coarse finned tube and fine finned tube are 8.4mm (3.3 fins per inch) and 4.2mm (5.7 fins per inch) respectively. As a reference, a bare tube with the same base diameter (38.4mm) as the finned tube is also studied. The complete tube structure consists of a tube with a threaded rod at one end and a steel cap at the other end. The threaded rod is used to fix the tube into the base plate of the test section. The rod length is one of two adjustable factors (the other is added end mass) used to tune the tube to the desired natural frequency. In addition, the slender rod will reduce the stiffness of the tested tube to simulate a real longer tube. The steel cap is applied to provide added end mass for the bare tube and the coarse finned tube to establish the dynamic similarity of experiments which will be discussed in a later section of this chapter. The related geometry and mass parameters of tubes are shown in Table 3-1. The detailed geometries of the serrated, helically wound fins are shown in Table 3-2. According to the definition of the recommended effective diameter, the fin serration width and serration height are not taken into account.

Tube Array Geometries

Two sorts of tube geometries are examined, one is normal triangular array and the other is parallel triangle array (Figure 3-1). In this figure, the flow is vertical from top to bottom. The four marked tubes are those monitored. The apparent misalignment of the tubes in these photos is due to their being taken from a video of the tubes undergoing fluidelastic instability. Since the

arrangements affect the dimensions of the test section, the positions of tubes in both transverse and stream-wise directions should be carefully designed to fit all the tubes into the test section which is a cube space with 686mm in length, 618mm in width and 616mm in height. According to Weaver and ElKashlan^[6], the number of rows required to simulate fluidelastic instability in a heat exchanger should be 5~6 in depth. Based on this suggestion, and considering the fin diameter of the tubes, the number of rows for the normal triangle tube array is designed to be 5 rows and the tube pitch is defined as 89.2mm. As the normal triangle array can be rotated at 90 degrees to become a parallel array, the base plate where all the tubes are mounted need only be designed for the normal arrangement. The base plate structure, which is a 25.4mm thick steel plate, is shown in Figure 3-2. The accuracy of tube pitch depends on the position accuracy and diameter size of each hole drilled in the base plate, which is $\pm 0.425\text{mm}$. Compared to the 89.2mm tube pitch, the relative error is $\pm 0.5\%$.

Table 3-1 Geometry and Mass Parameters of Tubes

	Total tube mass (kg)	Tube length(m)	Rod mass (kg)	Rod length (m)	Net tube mass(kg)
BT	2.548	0.606	0.082	0.190	2.460
CFT	3.996	0.608	0.127	0.295	3.863
FFT	5.169	0.608	0.108	0.250	5.055
	D_b (m)	D_f (m)	Fin thickness(mm)	Fin pitch (mm)	D_{eff} (m)
BT	0.0384	NA	NA	NA	0.0384
CFT	0.0384	0.0758	1.37	8.52	0.0444
FFT	0.0384	0.0767	1.48	4.34	0.0515

The mass of nut (5~7g) and rod should be subtracted from the total tube mass to obtain the net tube mass.

The dimensions and weights of tubes are based on the average results of the actual measurements.

The weight scale is calibrated to $\pm 0.001\text{kg}$; the precision of the vernier caliper is $\pm 0.02\text{mm}$.

Table 3-2 Fin Geometries

Tube	Fin height	Fin serration width	Serration height
CFT	18.5mm	4.4mm	12.7mm
FFT	19.1mm	4.5mm	12.7mm

The test section has a nearly square cross section of $0.618 \times 0.616 \text{ m}^2$. The normal triangle arrays (see Figure 3-1-a) consist of 32 flexible tubes, and the parallel triangle arrays (see Figure

3-1-b) consist of 24 flexible tubes. It is noted that the normal triangle array is rotated at 90 degree to become the parallel triangle array. Thus, only one test section and support structure had to be manufactured. The tube pitch is 89.2 mm for all arrays. The test section is designed to be adjustable for the different tube types and array geometries. Half tubes are used as the boundaries of the test section on both sides. The dimensions of the triangle arrangements are given in Table 3-3.

Table 3-3 Specifications of Triangle Arrangements

	Tube pitch (mm)	Effective diameter(mm)			Pitch ratio P/D _{eff}			row	Tube number
		BT	CFT	FFT	BT	CFT	FFT		
Normal array	89.2	38.4	44.4	51.5	2.323	2.009	1.732	5	32
Parallel array	89.2	38.4	44.4	51.5	2.323	2.009	1.732	7	24

3.2 Dynamic Similarity

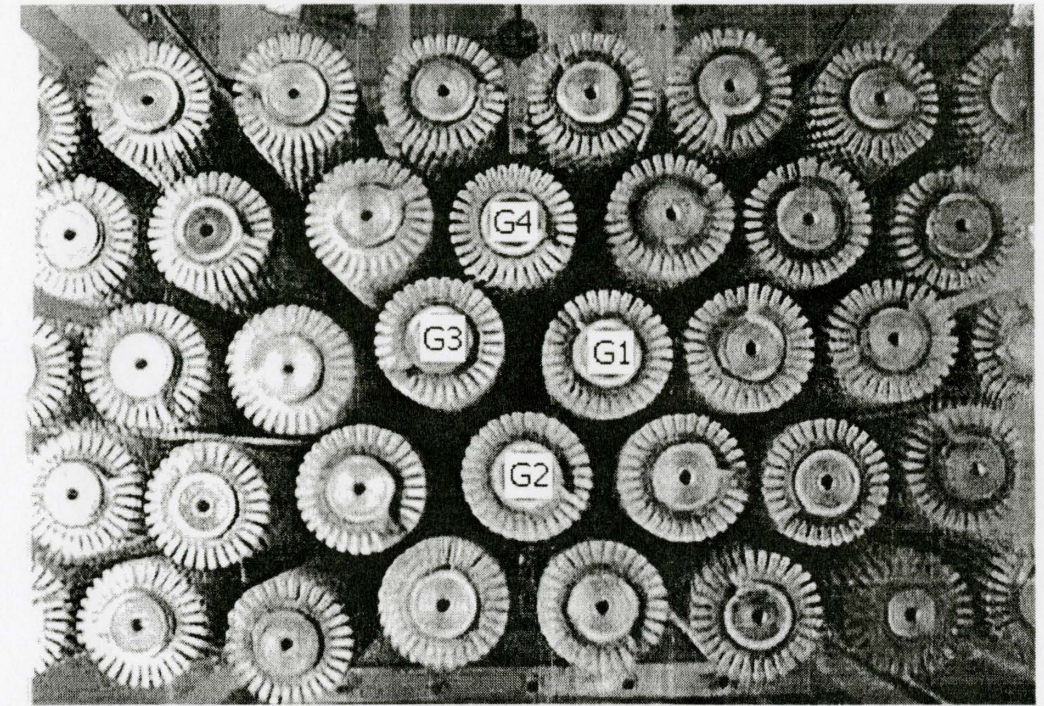
The dynamic similarity between the fine finned tube array and the coarse finned tube array is maintained through the mass ratio and the natural frequency of the tubes. Since the fine finned tube has the higher mass per unit length, the coarse finned tube must have an end mass added to keep the same mass ratio. The natural frequencies of both sorts of finned tubes should be tuned to the same frequency during the experiment.

Similarity of Mass Ratio

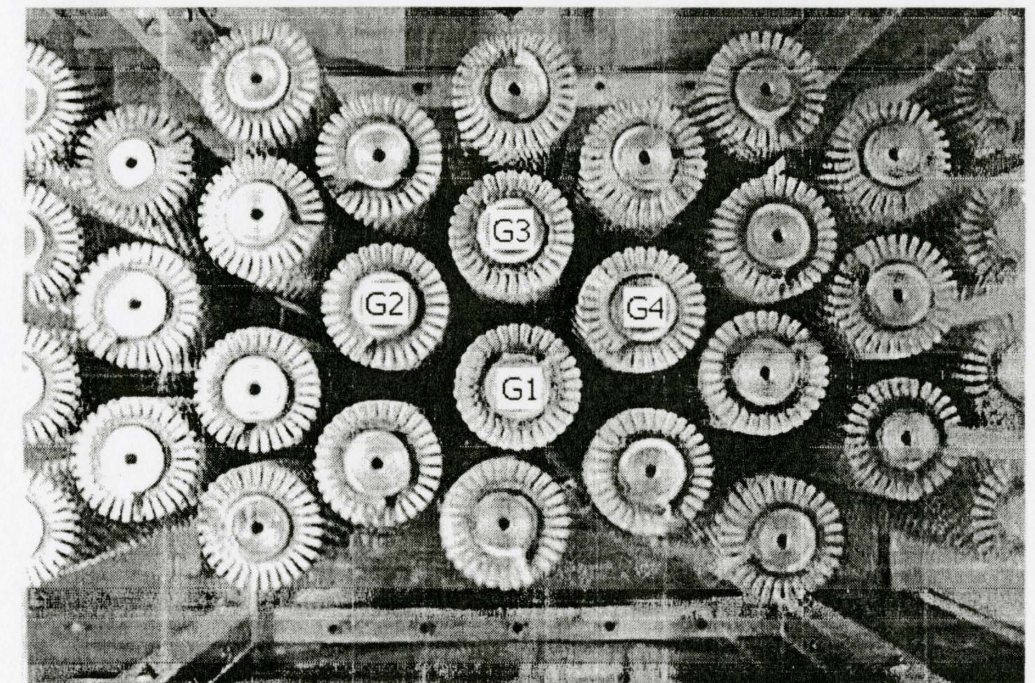
Mass ratio is defined by $\frac{m}{\rho D_{eff}^2}$. Since the mass ratio of the coarse finned tube should be as close as possible to the mass ratio of fine finned tube, the end mass added to the coarse finned tube can be calculated using the following equations:

$$\frac{m_f}{\rho D_{eff-f}^2} = \frac{m_c + m_a}{\rho D_{eff-c}^2} \quad \text{and} \quad m_a = m_f \frac{D_{eff-c}^2}{D_{eff-f}^2} - m_c$$

where subscript f refers to fine finned tubes, c refers to coarse finned tubes and a refers to added end mass.



a) Normal Triangle Array



b) Parallel Triangle Array

Figure 3-1 Triangle Arrangements

Flow Vertically Downwards

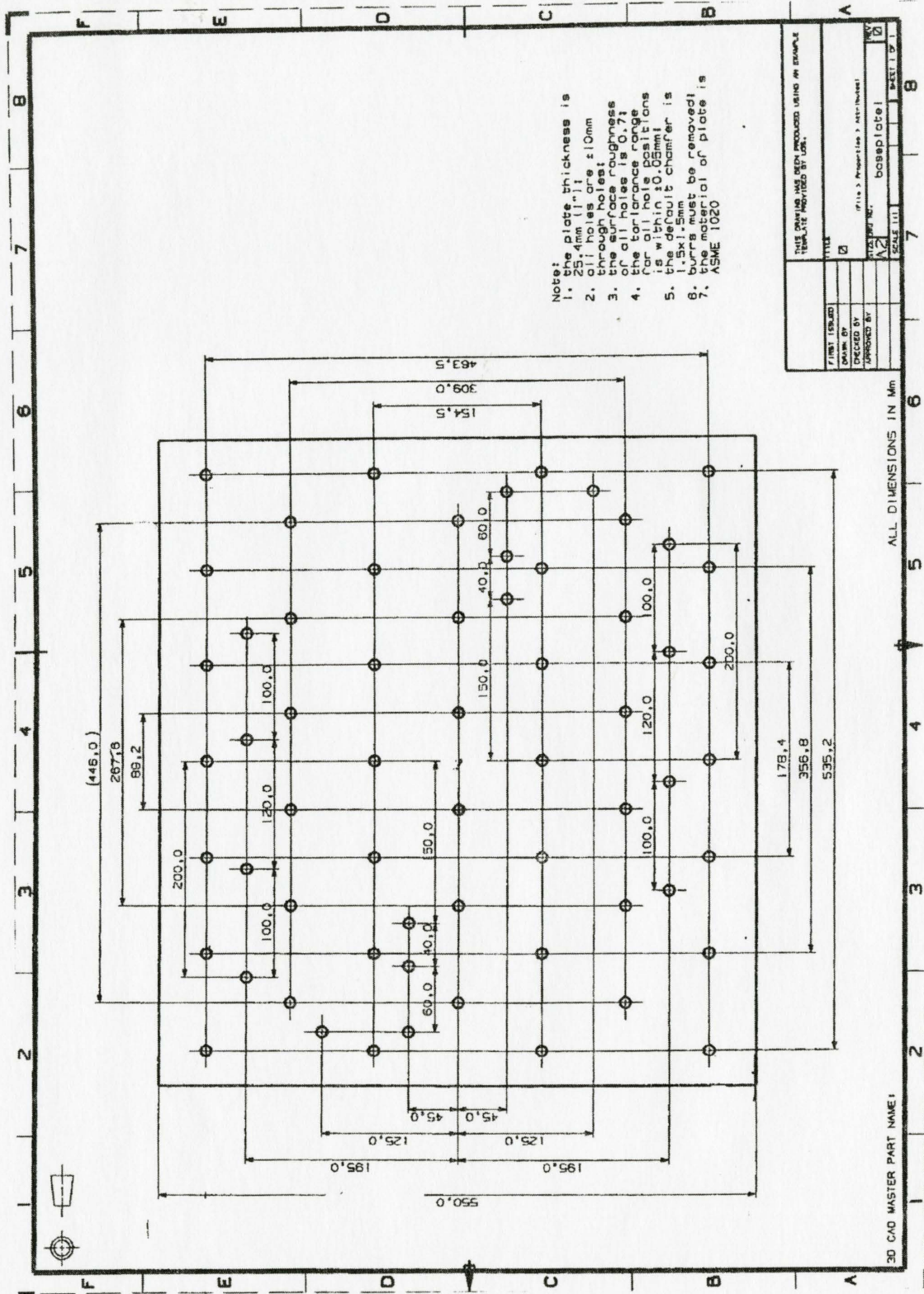


Figure 3-2 Base Plate Structure

Table 3-4 shows the mass parameters of each tube:

Table 3-4 Mass Parameters of Tubes

	Net tube mass(kg)	End mass (kg)	m (kg/m)	mass ratio
BT	2.460	0.420	4.059	2337.9
CFT	3.863	0.103	6.354	2737.5
FFT	5.055	0	8.314	2662.4
The density of air is 1.1774 kg/m ³ at 300K;				
The relative error of mass ratio between the finned tubes is $\pm 1.4\%$.				

In this study, the bare tube did not have sufficient end mass added to ensure the same mass ratio.

Similarity of Natural Frequency

Natural frequencies for both finned tubes should be tuned to be the same. The tube frequency is determined primarily by the rod length and tube mass. When the tube mass is determined, the rod length will be the only factor affecting the natural frequency of tube. The rod length has an influence on the assembly height of the base plate of the test section, which then affects most other assemblies and the supporting structure of the test section. Therefore, the rod length should be carefully calculated to get an ideal natural frequency range of tube and a suitable range of rod length before conducting the test.

ANSYS is applied to predict the fundamental natural frequencies and lengths of the tubes. To simplify the FEM simulation, the finned tube is reduced to a hollow circular cylinder with an effective diameter and an added mass at its end (see Figure 3-3). It is a cantilever fixed at the bottom of the flexible rod. The tube mass, material properties and geometry are listed in Table 3-5.

The natural frequency and rod height are what we want to determine in ANSYS. But before we figure out the final accurate results the estimated values must be calculated to reduce the cut and try process in ANSYS. The simplest approach to evaluate the fundamental natural frequency of the cantilever-like tube structure is to assume it is a single degree of freedom cantilever with

its mass concentrated at its free end (as shown in Figure 3-3). The cantilever length is supposed to be the rod height plus the half tube height; the concentrated mass is equal to the mass of the tube.

The natural frequency is then given by:

$$f = \frac{1}{2\pi} \sqrt{\frac{k}{m + m_a}}$$

where $k = \frac{3EI}{(h_r + 0.5H)^3}$, $I = \frac{\pi D_r^4}{64}$, E , m , m_a , h_r and D_r are the same in Table 3-5.

The results are calculated and listed in Table 3-6. Table 3-7 summarizes the basic information of ANSYS modeling of the finned tubes. Since the cut and try process is applied to calculate the tube's natural frequency, the geometry modeling, mesh generation, material property and load definition are introduced automatically by using ANSYS Parametric Design Language (APDL) in order to make the simulation easier.

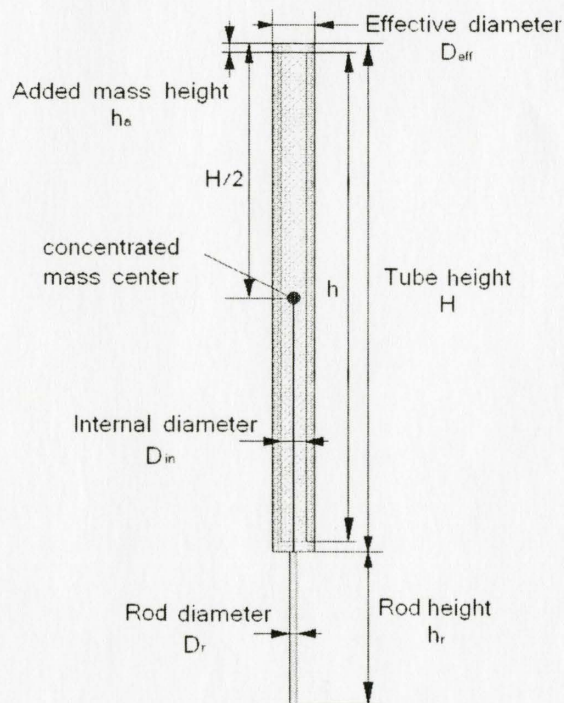


Figure 3-3 Finned Tube Structure in ANSYS

Table 3-5 Tube Mass, Material Property and Geometry in ANSYS

	Coarse Finned Tube	Fine Finned Tube	Note
Net tube mass $m(kg)$	3.863	5.055	Not including rod mass
Rod mass $m_r(kg)$	To be determined	To be determined	$m_r = \rho_r \frac{\pi D_r^2 h_r}{4}$
Added end mass $m_a(kg)$	0.103	0	$m_a = \rho_{eff} \frac{\pi D_{in}^2 h_a}{4}$
$D_{eff} (m)$	0.0444	0.0515	
Internal diameter $D_{in} (m)$	0.0303	0.0303	
Rod diameter $D_r (m)$	0.0082	0.0082	3/8" threaded rod
Tube height $H (m)$	0.608	0.608	
Internal height $h (m)$	0.584-0.020=0.564	0.584	End cap thickness of fine finned tube is 0.012
Added end mass height $h_a (m)$	0.020	0	
Rod height $h_r (m)$	To be determined	To be determined	Cut and try method
*Effective density $\rho_{eff} (kg/m^3)$	7218	5982	$\rho_{eff} = \frac{4m}{\pi D_{eff}^2 H - \pi D_{in}^2 h}$
Rod density $\rho_r (kg/m^3)$	7800	7800	
Young's Modulus $E (GPa)$	205	205	
Poisson ratio σ	0.27	0.27	

* Since the finned tube is treated as an equivalent bare tube, its equivalent density should be calculated by using the net tube mass divided by its equivalent volume.

Table 3-6 Frequency and Rod Height Evaluated by Concentrated Mass

	Coarse Finned Tube		Fine Finned Tube	
	Rod Height (m)	Frequency (Hz)	Rod Height (m)	Frequency (Hz)
1	0.244	2.3	0.202	2.3
2	0.215	2.5	0.174	2.5
3	0.189	2.7	0.150	2.7

Table 3-7 Summary of ANSYS Model

Element Types	Solid 92, 3-d 10-node tetra solid Solid 95, 3-d 20-node brick solid
Material Types	See Table 4-5
Mesh Types	Hex, tetra, mesh tool smart size 3
Analysis Types	Modal, Block Lanczos Method
Load Define	Displacement all DOF 0
APDL	See appendix C

Figure 3-4 and Figure 3-5 show the mesh and first order mode of fine finned tube. Table 3-8 lists the results computed by ANSYS

Table 3-8 Frequency and Rod Height Computed by ANSYS

	Coarse Finned Tube		Fine Finned Tube	
	Rod Height (m)	Frequency (Hz)	Rod Height (m)	Frequency (Hz)
1	0.230	2.432	0.195	2.437
2	0.220	2.509	0.185	2.528
3	0.210	2.598	0.175	2.628

From Figure 3-6, we can determine a range of frequency and rod installation height for each finned tube. The actual installation positions are also plotted in the figure.

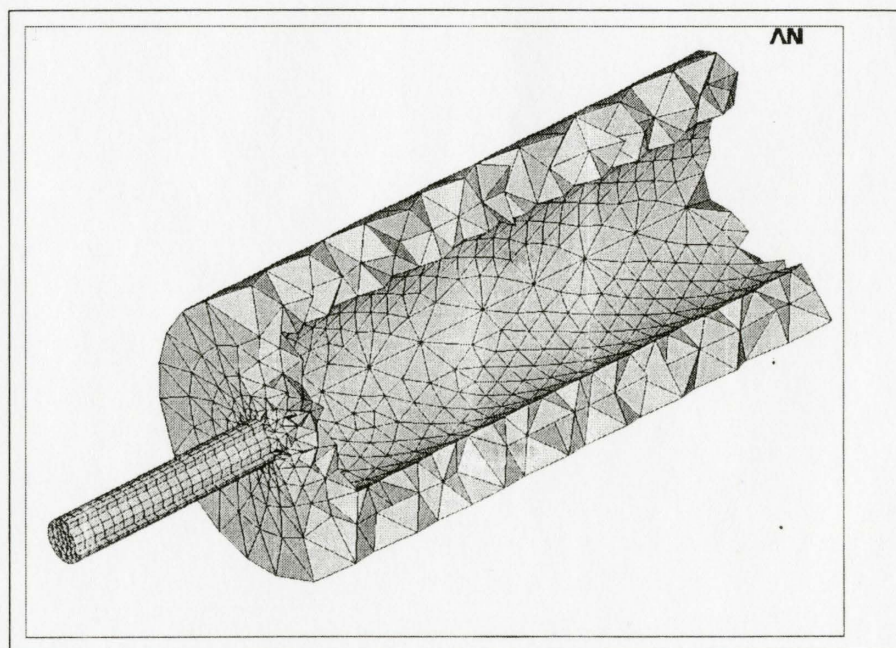


Figure 3-4 Hybrid Mesh

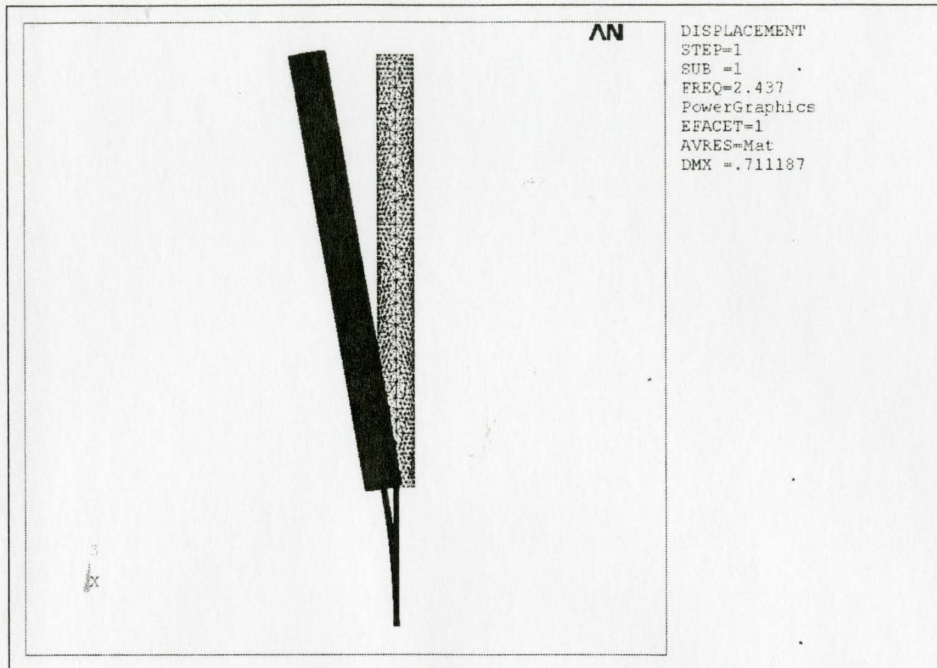


Figure 3-5 Fundamental Mode of Finned Tube

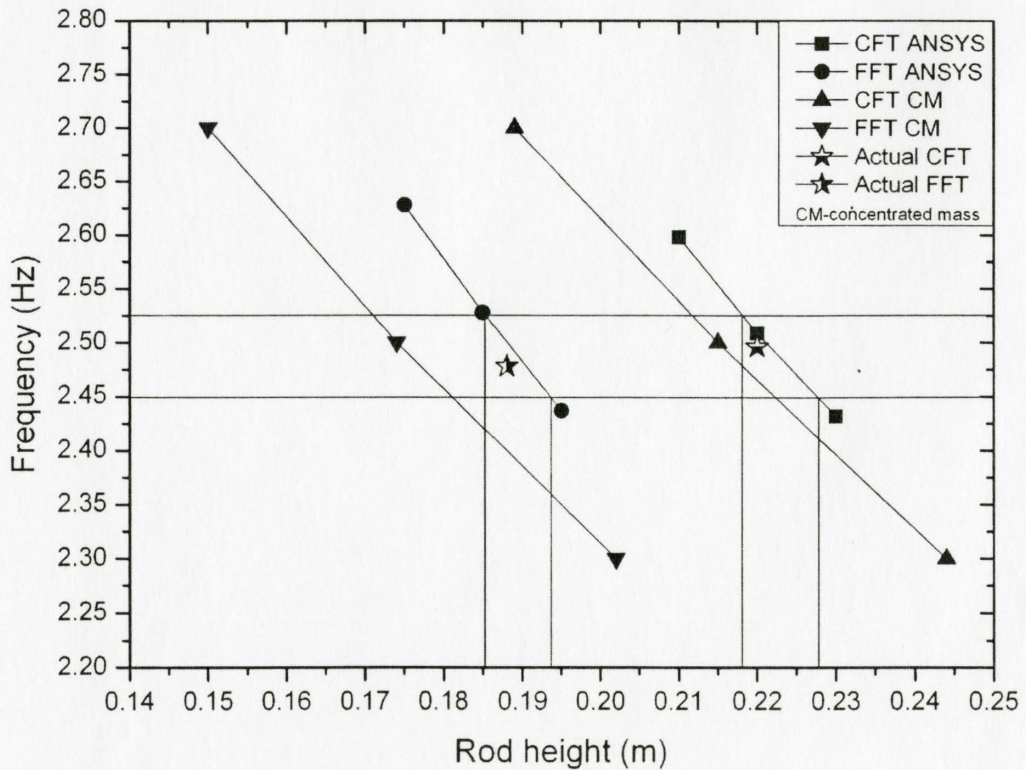


Figure 3-6 Determination of Frequency and Rod Height

3.3 Calibration of Strain Gages

The tubes are 0.608 m in height, with a threaded support rod welded to the bottom of each tube in a cantilever fashion. Four tubes are monitored in each array using strain gages attached to the support rod in the stream-wise and transverse flow directions to capture their respective amplitudes of vibration. VISHAY strain gages are applied to measure the tube amplitudes. Two gages are located near the fixed end of each tube rod, glued at right angles to one another (see Figure 3-7). The support rods are affixed to a base support structure with a nut and washer above and below. All nuts are torqued to the pre-load value of 20.4 Nm.

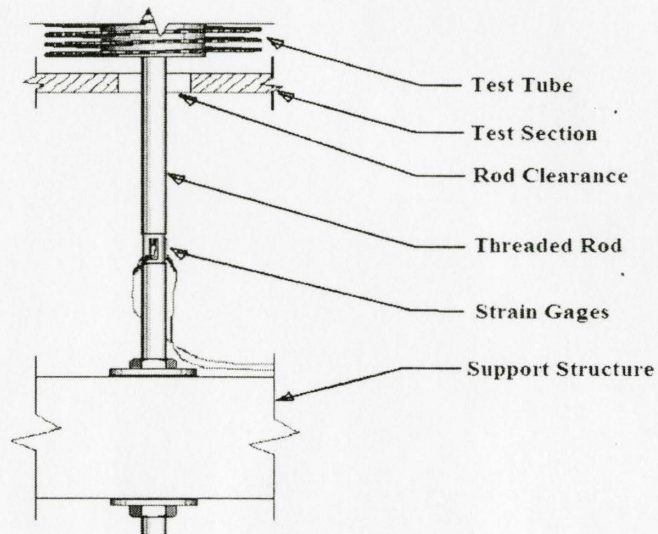


Figure 3-7 Test Tube Support, Monitored Tubes

The displacement of the top end of the tube from its original point is defined as the amplitude of the tube. The relationship between the amplitude and the output voltage of the strain gages were calibrated before the experiments. The calibration was conducted after the whole test section was set into the wind tunnel. Ideally, the strain gages are expected to be located exactly in the transverse and stream-wise directions. But practically, the strain gages are very difficult to keep identical with the x and y directions of test section because of tuning the tube, base plate installation, and test section assembling. If there is an angle between the coordinate of the strain

gage and the coordinate of the test section shown in figure 3-8, the calibrations in x and y directions will produce 4 voltage signals noted as v_{x1} , v_{y1} , v_{x2} , and v_{y2} . If assuming the coefficients for the voltage vs. the displacement to be K_x and K_y respectively, these four voltage signals will be converted to corresponding displacements by:

$$x_{g1} = K_x \times v_{x1}$$

$$y_{g1} = K_y \times v_{y1}$$

$$x_{g2} = K_x \times v_{x2}$$

$$x_{g2} = K_y \times v_{y2}$$

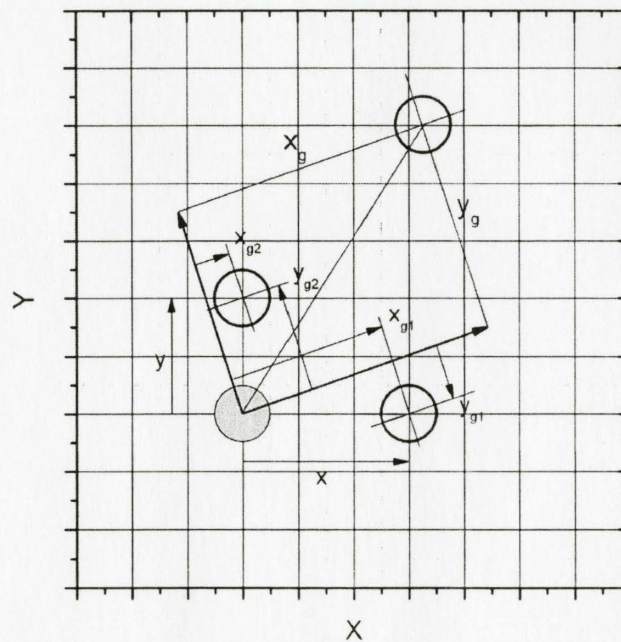


Figure 3-8 Strain Gage Calibration

The actually recorded displacements in X and Y coordinates of the test section can be written as:

$$x = \sqrt{(K_x \times v_{x1})^2 + (K_y \times v_{y1})^2}$$

$$y = \sqrt{(K_x \times v_{x2})^2 + (K_y \times v_{y2})^2}$$

Therefore the coefficients K_x and K_y can be solved from the above equations as follows:

$$K_x = \sqrt{\frac{(xv_{y2})^2 - (yv_{y1})^2}{(v_{x1}v_{y2})^2 - (v_{x2}v_{y1})^2}}$$

$$K_y = \sqrt{\frac{(xv_{x2})^2 - (yv_{x1})^2}{(v_{x2}v_{y1})^2 - (v_{x1}v_{y2})^2}}$$

Once the converting coefficients K_x and K_y are determined, the tube amplitude at any position (see figure 3-8) can be calculated by:

$$RMS \text{ Amplitude} = \sqrt{x_g^2 + y_g^2} = \sqrt{(K_x v_x)^2 + (K_y v_y)^2}$$

The positions and numbers of the four monitored tubes are shown as Figure 3-1. The calibration results can be seen in Appendix D. The converting coefficients are seen in Table 3-9:

Table 3-9 Converting Coefficients of Amplitude vs. Voltage unit (mm/V)

	BT				CFT				FFT			
	G1	G2	G3	G4	G1	G2	G3	G4	G1	G2	G3	G4
K_x	33.07	33.07	30.22	33.00	72.33	65.95	65.20	61.51	44.69	48.67	47.52	44.96
K_y	32.73	32.38	32.40	32.36	64.17	64.93	63.47	63.29	48.44	48.99	50.51	50.26

3.4 Measurement and Calculation of Damping and Natural frequency

The damping decay curve can be obtained by plucking the tube and recording its vibration signals. The decaying profile consists of the peak points of vibration signals and can be described by an exponential function. Meanwhile, the natural frequency and amplitude can also be obtained by a Fast Fourier Transformation method, which transforms the signals from the time domain into the frequency domain. The Fast Fourier Transformation can be conducted by the signal analyzer HP 35670a, as well as by other mathematical software. In the present work, Origin (student version) was used to perform the signal analysis.

The decaying behavior is shown graphically in Figure 3-9 as oscillations with diminishing amplitude. The signal recording period is 127 seconds. The curve of damping decrement usually is described in this form:

$$y = Ae^{-\zeta\omega_n t} \sin\left[(1-\zeta^2)^{1/2} \omega_n t + \phi\right]$$

The damped oscillation frequency, ω_d , is seen to be:

$$\omega_d = (1-\zeta^2)^{1/2} \omega_n$$

When the damping is small, $\omega_d \approx \omega_n$, then the damping decay curve (the peak profile) can be written as:

$$y = Ae^{-\zeta\omega_n t} + y_0$$

This curve can be obtained by exponentially fitting the peak points of the damping oscillations as seen in Figure 3-9. The natural frequency can be obtained by Origin (seen in Figure 3-10).

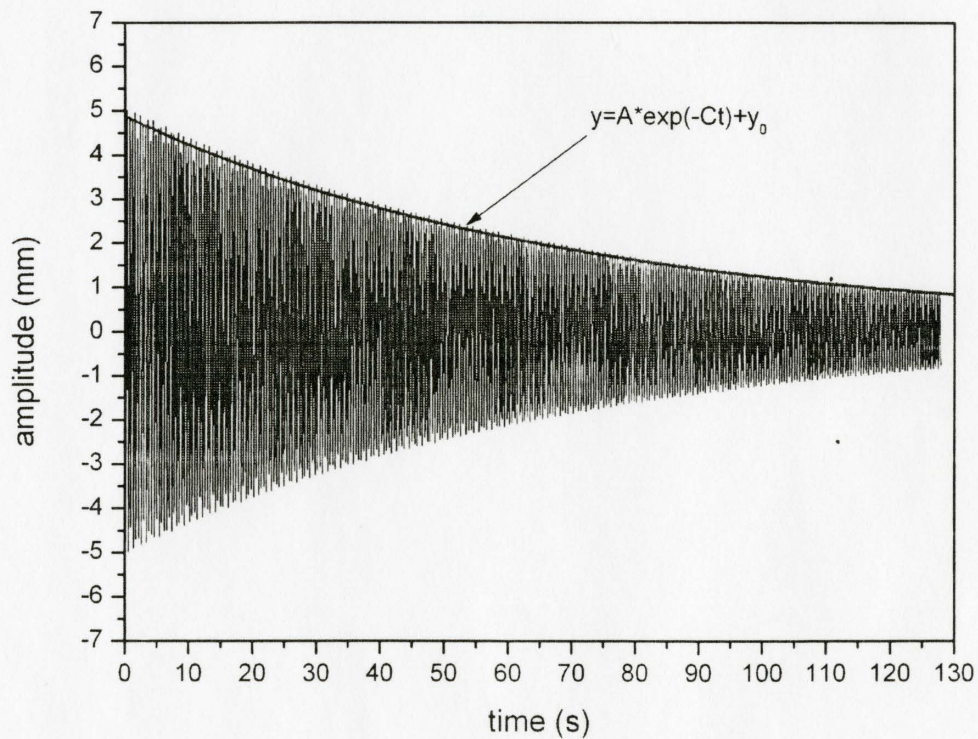


Figure 3-9 Peak Fitting for Damping Ratio Calculation

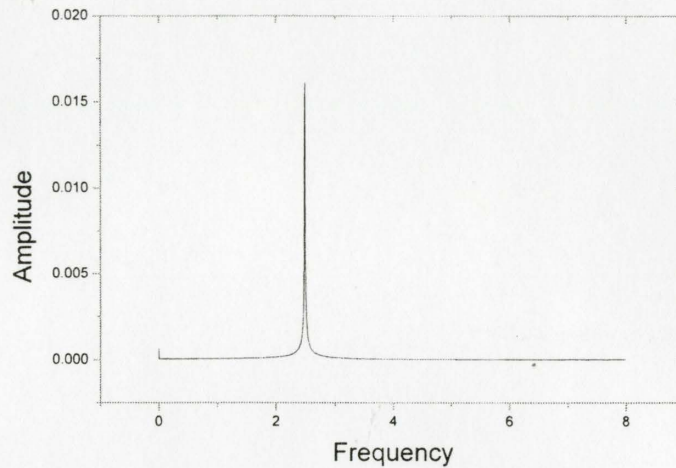


Figure 3-10 Natural Frequency

From Figure 3-9 and 3-10, we know that:

$$\zeta = \frac{C}{\omega_n} = \frac{C}{2\pi f}$$

where C is the exponential coefficient of the peak fitting curve in Figure 3-9, and f is the natural frequency read from Figure 3-10. Each strain gage produces an exponential peak fitting function and a frequency reading. Corresponding damping factor and logarithmic decrement of damping are listed in Table 3-10:

Table 3-10 Natural Frequency and Damping of Tube

Strain Gages	Natural Frequency f (Hz)			Damping Ratio ζ ($\times 10^4$)			Logarithmic decrement of damping δ ($\times 10^3$)		
	BT	CFT	FFT	BT	CFT	FFT	BT	CFT	FFT
G1	4.253	2.486	2.478	4.6	9	13.4	2.88	5.6	8.44
G2	4.254	2.496	2.502	5.2	8	10.5	3.25	5.0	6.56
G3	4.235	2.497	2.472	5.4	9	11.8	3.41	5.7	7.43
G4	4.286	2.505	2.461	4.3	10	12.2	2.67	6.0	7.66
mean	4.257	2.496	2.478	4.9	9	12.0	3.05	5.6	7.52
error	$\pm 0.3\%$	$\pm 0.2\%$	$\pm 0.5\%$	$\pm 9\%$	$\pm 5\%$	$\pm 7\%$	$\pm 9\%$	$\pm 5\%$	$\pm 7\%$

Structural damping is dominant, the aerodynamic component being small. The lowest measured damping value is for the bare tubes and the damping of a finned tube increases with the fin density, which can be attributed to increasing aerodynamic damping component.

Software Package

The damping calculations and frequency analysis are completed by the mathematical software Origin pro 8.0 (student version). Origin can provide many data processing tools, such as FFT, peak analyzer, nonlinear fitting, 2D plotting and so forth. Origin plays a vital role in this current study.

Tuning Tubes

Except the four monitored tubes of each array, the other tubes in the array should also be tuned to the designed frequency as discussed above. An accelerometer was used to collect the vibration signals for tuning. The schematic diagram seen in Figure 3-11 illustrates the tuning procedure. The accelerometer is fixed to the tube using a magnet. The cable of the accelerometer is connected with the HP35670a, which is employed to analyze the signals. When plucking the tube, the oscillating signals are recorded and analyzed by HP and then the tube frequency is obtained. If the frequency is not the desired value, the rod length is varied until the correct frequency is achieved. The whole routine is repeated until all tubes in the array have the same frequency within a relative error of $\pm 1\%$.

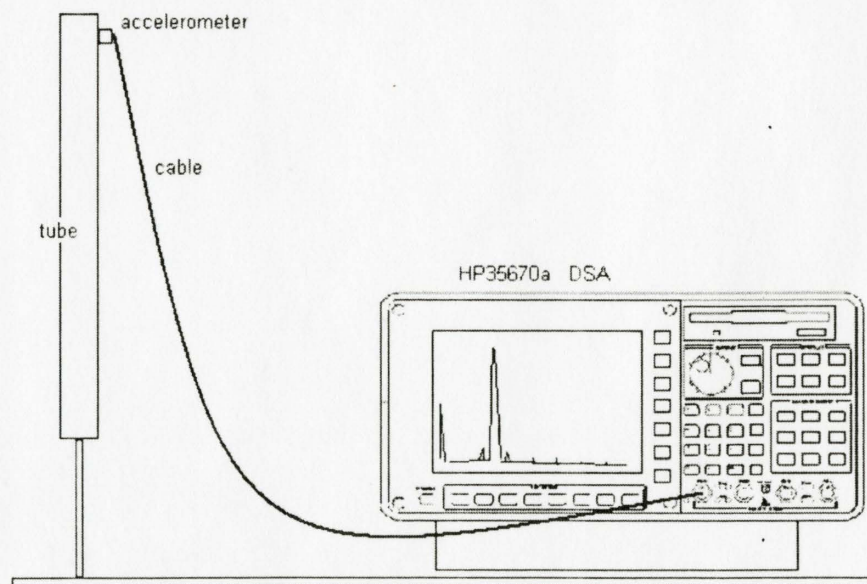


Figure 3-11 Schematic Diagram for Tuning Tubes

3.5 Instruments and Procedures of Experiment

Micro Manometer and Velocity Measurement

The Betz micro-manometer is an instrument used to measure low air pressures or gas pressures with very high accuracy. The Betz micro-manometer is principally a J-tube manometer in which the fluid level is measured by a floating glass scale. A pressure change results in a change of the fluid level. A light source projects an image of the glass scale on the display screen. The Betz micro-manometer is used for measurement of very small pressure differences of sensors like Pitot tubes; its standard calibration and scale unit is Pascal (Pa). Before the test, the Betz is corrected by a pre-calibrated pressure transducer, as seen in Figure 3-12, which shows that the maximum error is 5% at a pressure of 100Pa.

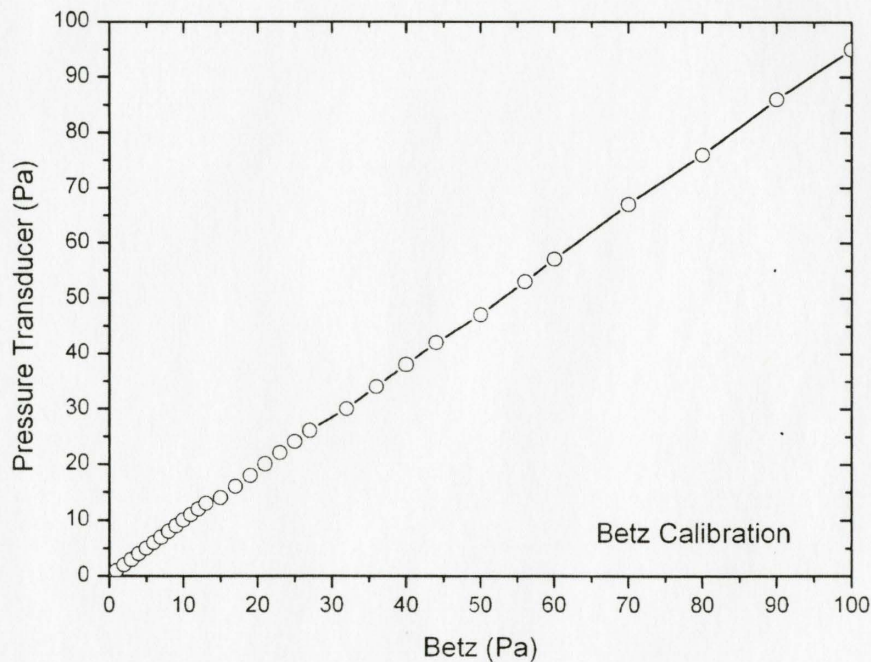


Figure 3-12 Correction between Betz and Pressure Transducer

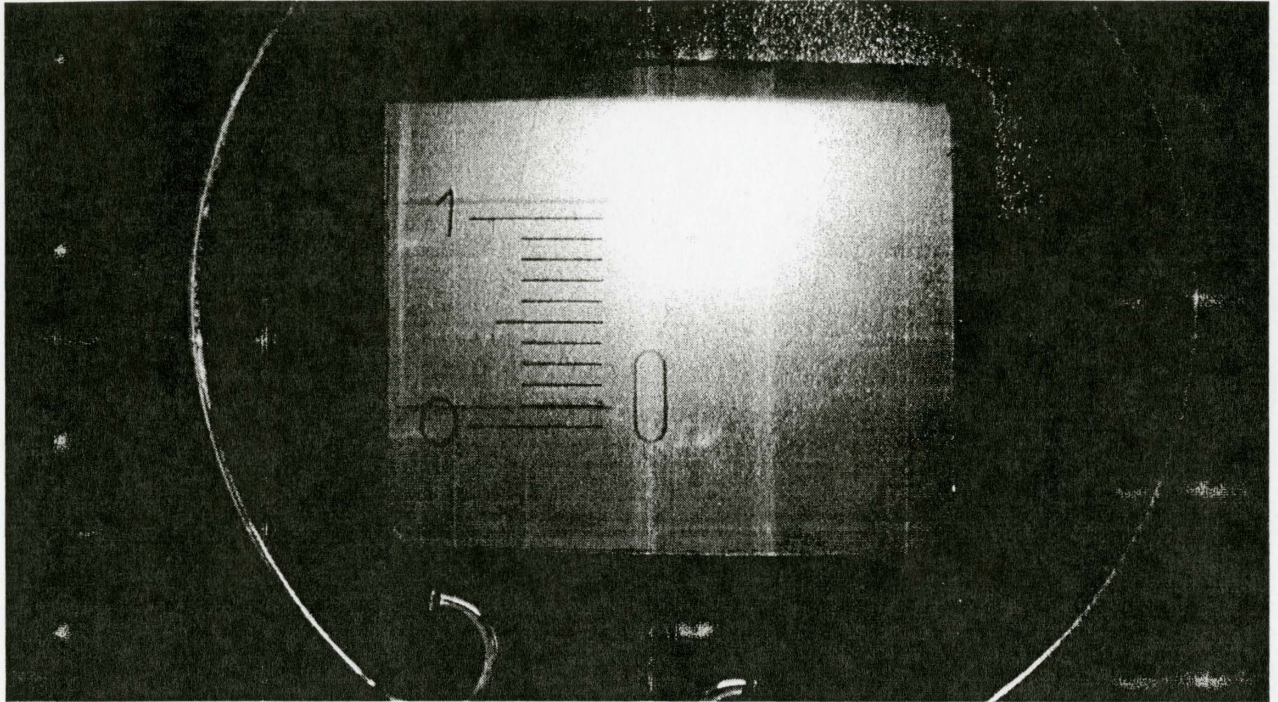


Figure 3-13 Betz Reading

The velocity of the upstream fluid flow in the wind tunnel is measured by Pitot tube. The pressure difference between the dynamic pressure and static pressure of the Pitot tube is read from the Betz (see Figure 3-13). The velocity is calculated by:

$$U = \sqrt{\frac{2\Delta p}{\rho}}$$

where Δp is the pressure drop between static pressure and dynamic pressure of Pitot tube, Pa, ρ is the air density, kg/m^3 , and U is mean upstream velocity, m/s.

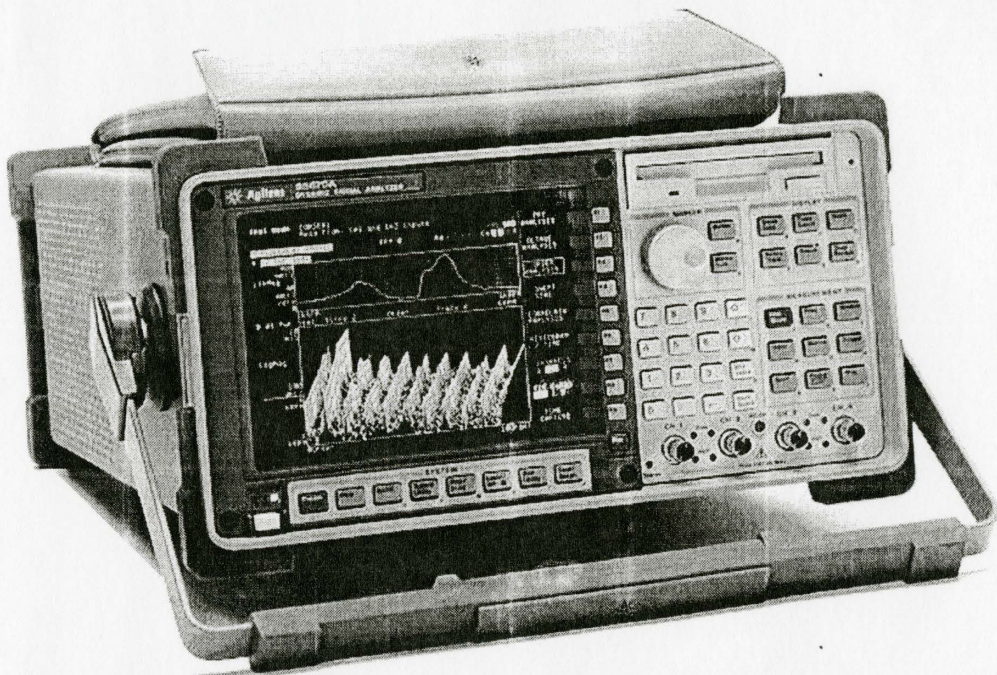
HP Dynamic Signal Analyzer and Signal Conditioning Amplifier

To obtain the experimental results, the signal from each calibrated strain gage is analyzed using a Hewlett-Packard 35670A Dynamic Signal Analyzer, with a Vishay 2310 Signal Conditioning Amplifier.

The 2310A Conditioner/Amplifier modules accept inputs from the strain gages and amplify the low-level signals to high-level outputs for multiple-channels. In this study, the filter is set to

10Hz, as the vibration signal is a low frequency source. The amplifier gain is set to 7×100 .

The Agilent 35670A is a portable four-channel dynamic signal analyzer for mechanical vibration and noise problems (see Figure 3-14). The key specifications are also listed in the figure. A detailed guideline can be found in the manual of HP 35670a [23]. In this study, the DSA is applied to analyze the tuning vibration signals, calibrate the strain gages, and record the time trace data during the damping tests and experiments for fluidelastic instability.



Frequency Range: 102.4 kHz 1 channel 51.2 kHz 2 channel 25.6 kHz 4 channel
Dynamic Range: 90 dB typical
Accuracy: ± 0.15 dB
Channel Match: ± 0.04 dB and ± 0.5 degrees
Real-time Bandwidth: 25.6 kHz/1 channel
Resolution: 100, 200, 400 & 800 lines
Time Capture: 0.8 to 5 M samples
Source Types: Random, Burst random, Periodic chirp, Burst chirp, Pink noise, Sine, Swept-Sine (option 1D2), Arbitrary (option 1D4)

Figure 3-14 HP 35670a Dynamic Signal Analyzer

Low Speed Wind Tunnel

Experiments were conducted in the low speed wind tunnel at McMaster University. The wind tunnel is composed by an inlet section, test section, axial fan and motor section, control system, velocity testing system including a Pitot tube and a Betz micro-manometer, and vibration testing system including a signal amplifier and a HP dynamic signal analyzer, as shown in Figure 3-15. The upstream turbulence intensity for the tunnel has been found to be 1% in previous studies. As the tubes are full scale, the test section is quite heavy compared to previous studies of fluidelastic instability. The total test section, including support structure and tubes, weighs approximately 350 kg for the normal triangle array of fine finned tubes.

Experimental Procedure

The procedure is the same for all the bundles studied. The wind tunnel velocity is increased to a set value and measurements are commenced after a time period sufficient to reach a steady state response (8 minutes for bare tubes and 10 minutes for finned tubes). The amount of time is longer for the finned tubes due to their lower natural frequency. The velocity is determined using the Pitot-static probe. Measurements of the tube response for each of the monitored tubes in the stream-wise and transverse directions are recorded by strain gages. In total there are eight sets of signals recorded. Since the HP 35670a has only 4 channels, each test has to be conducted twice to record the eight sets of signals. The vibration responses are collected and transferred from the strain gages through the signal amplifier into the HP analyzer, which can write the data onto a 3.5" floppy disk. The vibration signal data are processed in the computer after finishing the whole experiment.

Once this measurement is complete, the flow velocity is increased and another data point is captured in the same manner as previously described. Measurements would be terminated for two different conditions:

- 1) A tube within the array collided with another tube (fin-to-fin contact for finned tubes, this

is not necessarily a monitored tube).

2) If the amplitude of vibration is large (above 10% D_{eff}) and a significant change in slope of the amplitude versus velocity plot is observed.

The second condition is only used for the bare tubes, since larger amplitudes of vibration can potentially cause plastic deformation of the tube support.

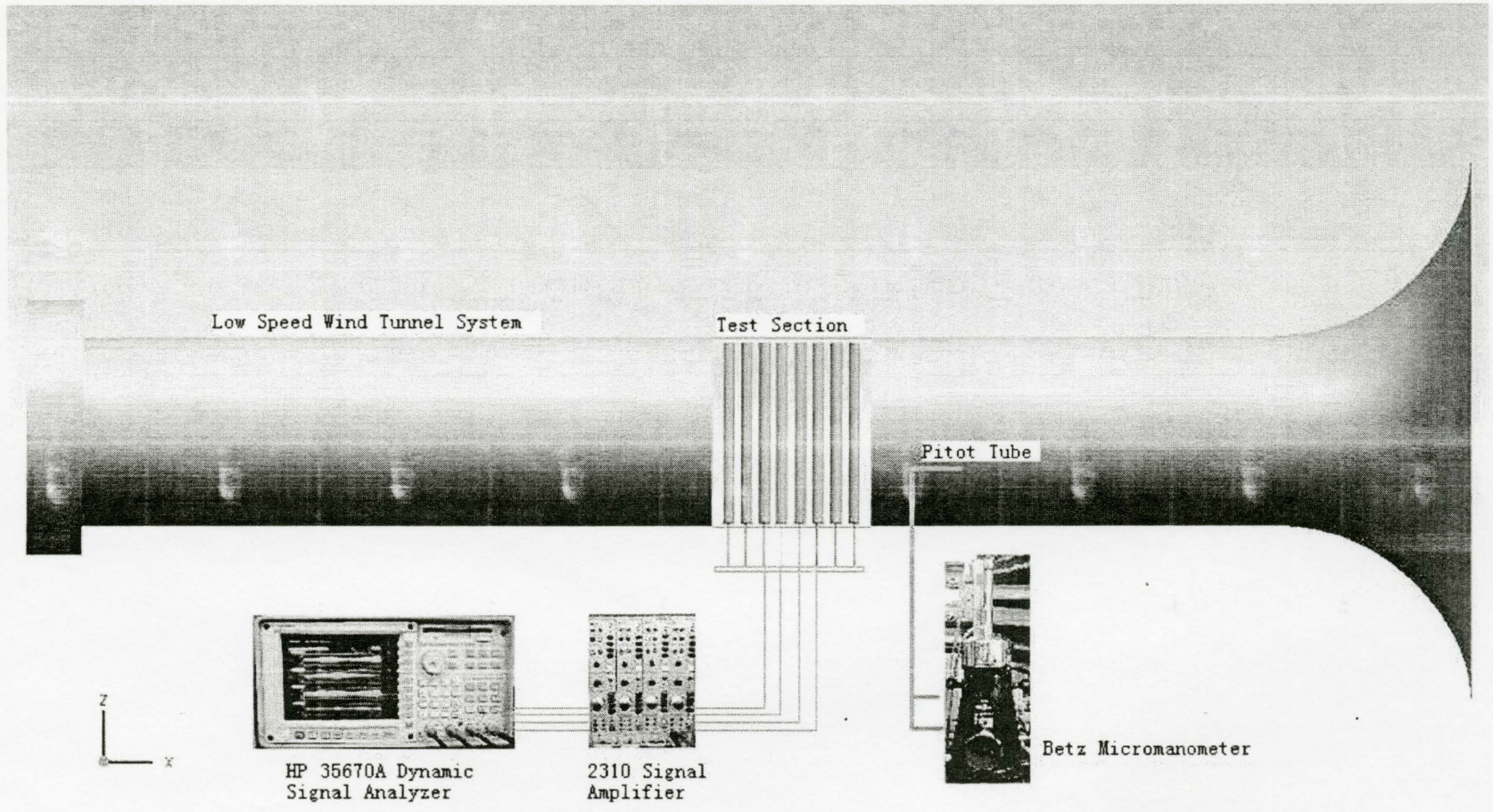


Figure 3-15 Wind Tunnel System for FEI

Chapter 4

RESULTS AND DISCUSSION

4.1 Experimental Results

The results for the normal triangle and parallel triangle arrays are presented in Figures 4-1 through 4-3. These plots are RMS amplitude/ D_{eff} versus reduced velocity (U_p/fD_{eff}) and are used to determine the critical velocity for fluidelastic instability. The legend in the figures showing G1 to G4 inclusive refer to calibrated data from the four strain gages as discussed in chapter 3. In some cases, experiments were repeated and the data are shown by a hyphen and experiment number. Thus, G3-2, for example, is the second experimental data for gage G3.

Bare Tubes

Figure 4-1 shows the typical flow induced response behavior of tube bundles in gas cross-flow. For the parallel array, all four of the monitored tubes change abruptly from small amplitude random turbulence response to large amplitude periodic response at a reduced velocity of about 25. This is taken as the fluidelastic stability threshold and is clearly defined. For the normal triangle array, the fluidelastic instability is reasonably well defined, the range of critical reduced velocity is from 52~62 with an average value of about 57.

Coarse Finned Tubes

Figure 4-2 shows the amplitude responses of coarse finned tubes (8.4mm/3.3fpi) in normal triangle and parallel triangle arrays to the reduced flow velocity. For the parallel array, the behavior of fluidelastic instability for each tube becomes complex in the post stable region. The amplitude response sometimes drops down and jumps up again. This is because during the test some tubes collided with each other and the response became modulated. However the periodic energy transfer portion of the dynamic response curve is still clearly defined as shown in the

circle of the figure. Thus, the critical reduced velocity can be identified as about 52.5. For the normal triangle array, the fluidelastic instability is clearly defined; the critical reduced velocity is approximately 70.

Fine Finned Tubes

Figure 4-3 shows the dynamic responses of fine finned tubes (4.2mm/5.7fpi) in normal triangle and parallel triangle arrays to the reduced flow velocity. For the parallel array, the critical reduced velocity is reasonably well defined, the range of critical reduced velocity is from 40~50, the average value approximately 45. For the normal triangle array, the fluidelastic instability is clearly defined and the critical reduced velocity is about 42.5. Table 4-1 lists the results of critical reduced velocity vs. damping parameter for all the tube arrangements as follows:

Table 4-1 Critical Reduced Velocity vs. Damping Parameter

	Normal Array		Parallel Array	
	Reduced velocity	Mass Damping	Reduced velocity	Mass Damping
BT	57	7.13	25	7.13
CFT	70	15.33	52.5	15.33
FFT	42.5	20.02	45	20.02

Mass Damping is defined by: $mass \ damping = \frac{m\delta}{\rho D_{eff}^2}$

4.2 Comparisons with World Data

The nuclear steam generator industry has been driving much of the research on fluidelastic instability, the vast majority of available data having tube pitch ratios between 1.3 and 1.5. The fossil fuel industry typically employs larger tube pitch ratios; hence the larger pitch ratio is used in the current study. In this study, the mass ratio, $m/\rho D_{eff}^2$, has been preserved and for practicality the tube pitch, P , was kept constant, which means P/D_{eff} changes. The experimental results for each array are compared with the world data on Weaver and Fitzpatrick's [9] stability maps (Figures 4-4 and 4-5). The data falls within or above the world data for the arrays tested; the plots have been adapted to U_g/fD_{eff} versus $m\delta/\rho D_{eff}^2$ to reflect the current study parameters.

Figure 4-1 RMS Amplitude/ D_{eff} vs. Reduced Velocity of Bare Tubes

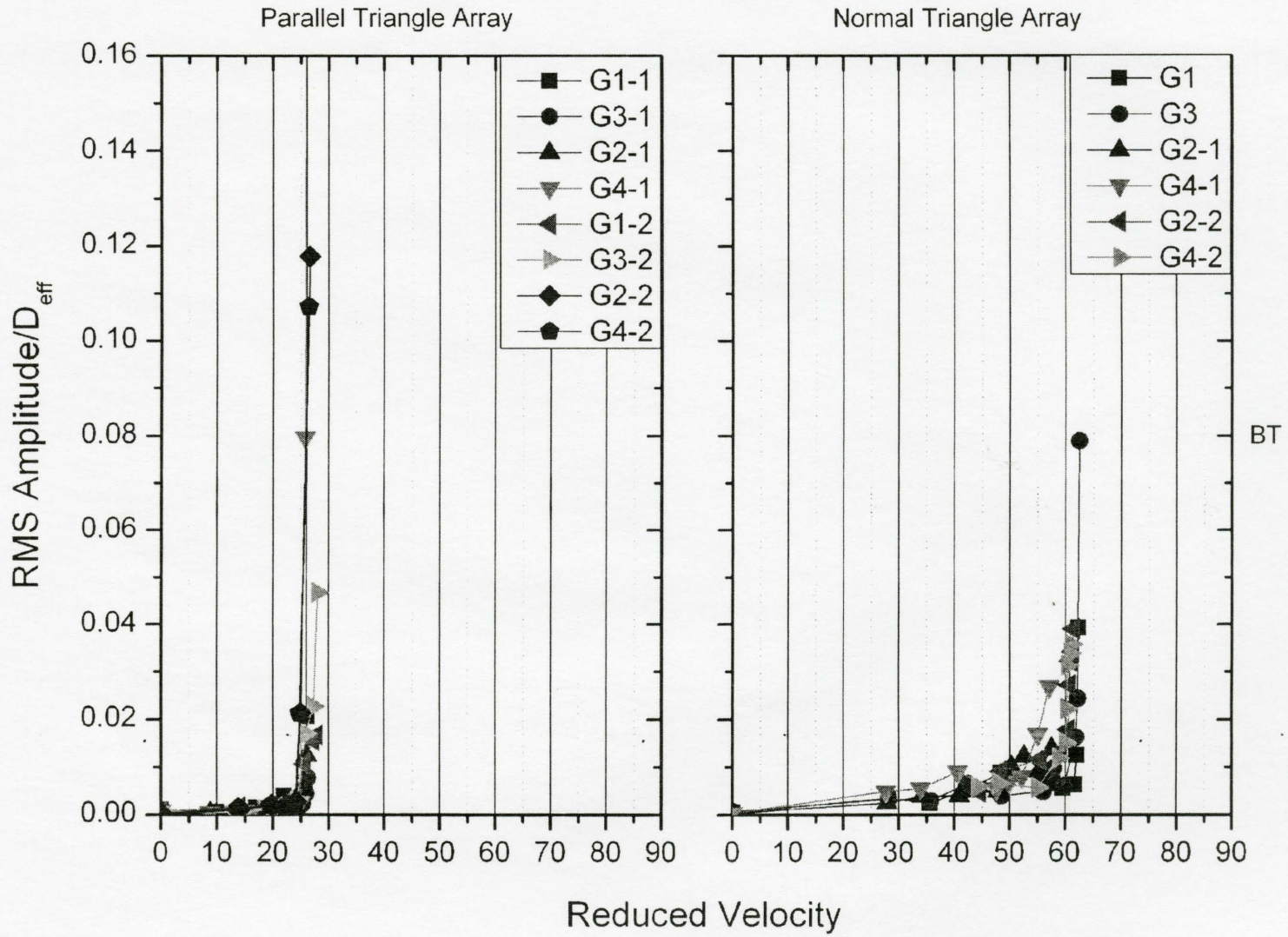


Figure 4-2 RMS Amplitude/ D_{eff} vs. Reduced Velocity of Coarse Finned Tubes

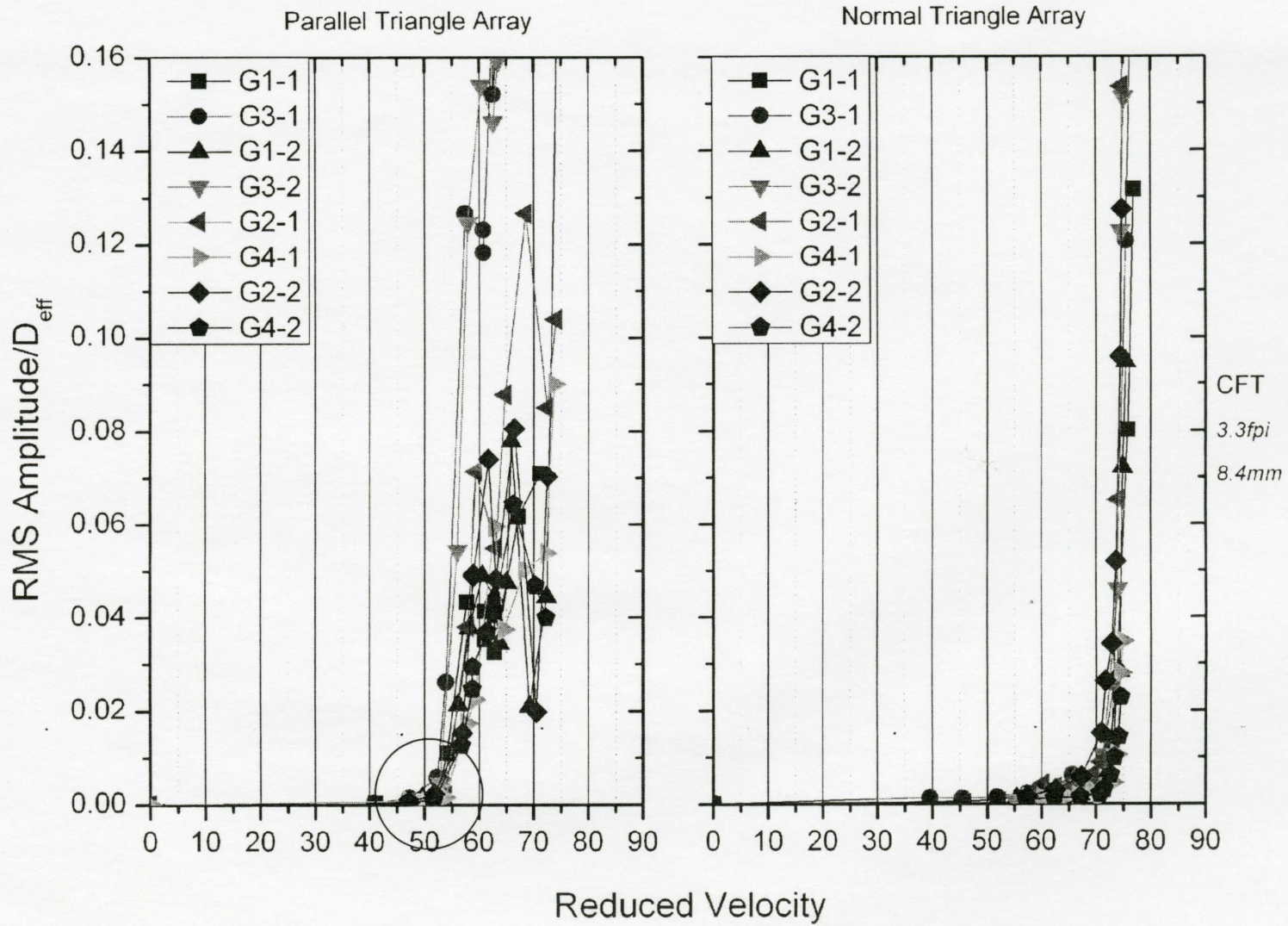
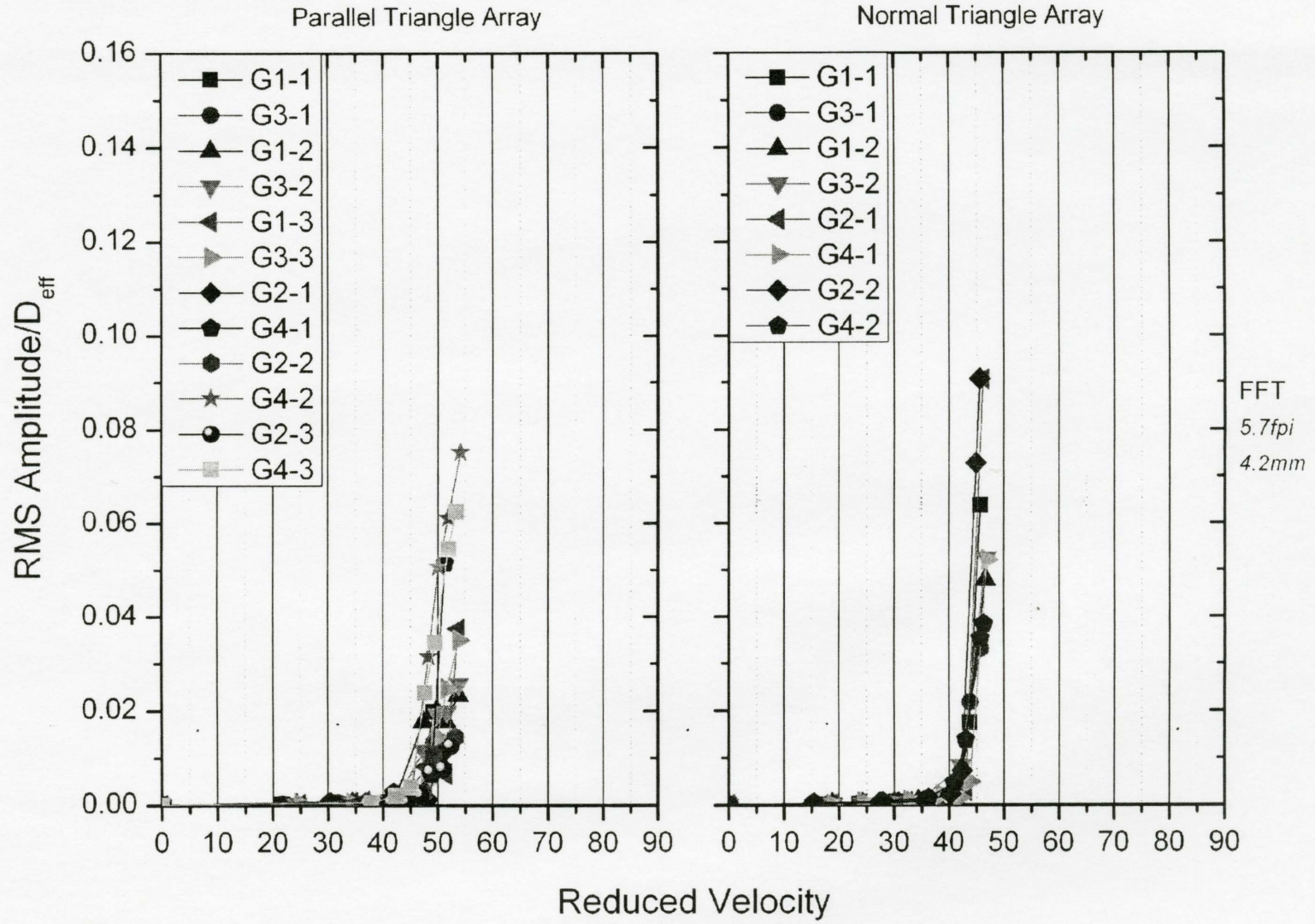


Figure 4-3 RMS Amplitude/ D_{eff} vs. Reduced Velocity of Fine Finned Tubes

Comparison with World Data: Normal Triangle Arrays

The bare tube data sits above the scatter of experimental data in Figure 4-4. In part this is likely because the current bare tube array has a tube pitch ratio much higher than the other data. The coarse finned tube array has a higher critical reduced velocity than the current bare tube array higher by 30% while the fine finned tube array has a lower reduced velocity which basically falls close to the upper end of the regular data cluster in this figure.

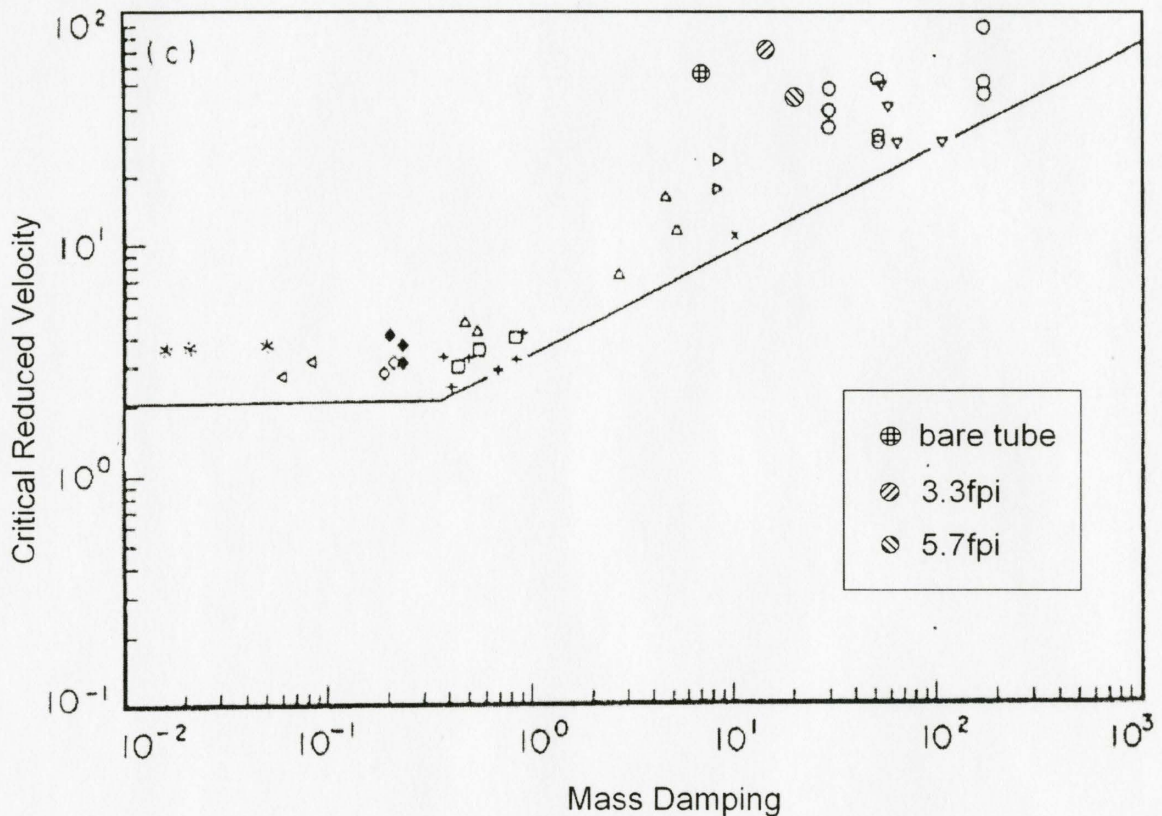


Figure 4-4 Normal Triangle Array in World Data

Comparison with World Data: Parallel Triangle Arrays

In Figure 4-5, the threshold values of all three tubes in the current study are higher than the corresponding data in literature [9]. For the bare tube, this is attributed to the larger pitch ratio. However for the finned tubes, their distinctly higher critical reduced velocities indicate that the effect of fins of parallel triangle arrays is to delay the critical velocity for fluidelastic instability.

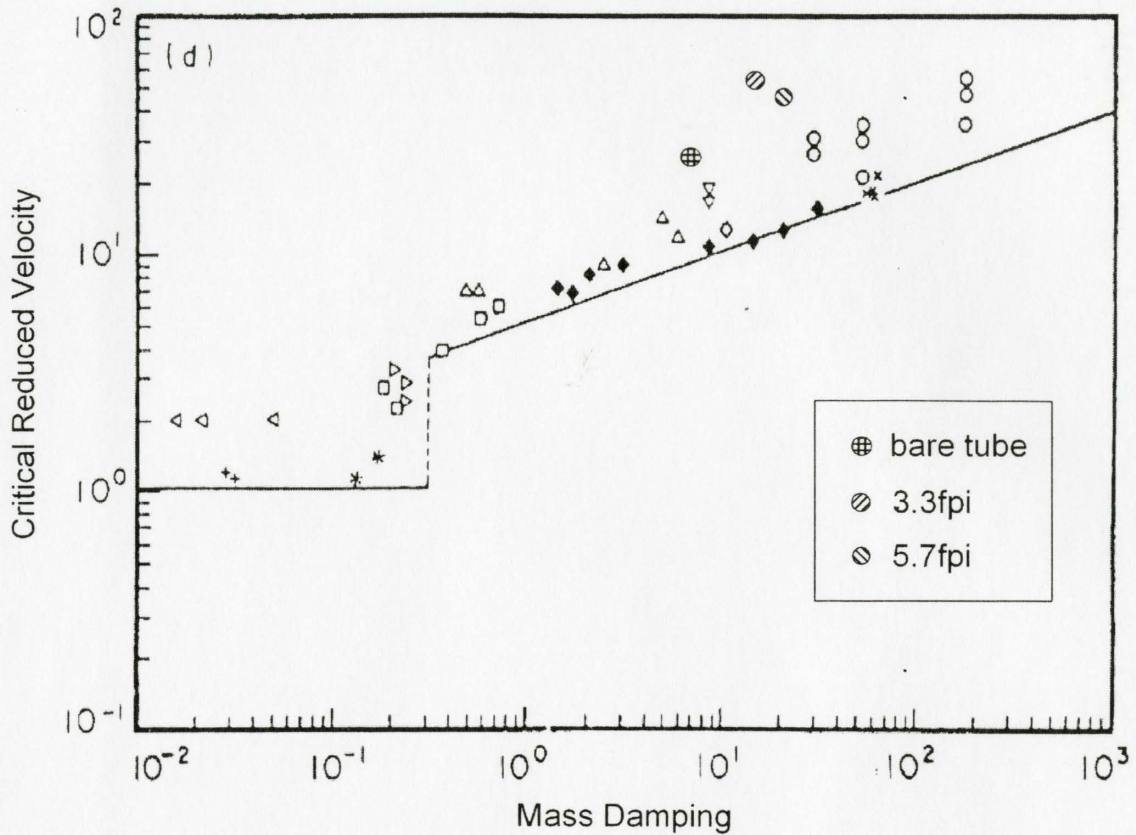


Figure 4-5 Parallel Triangle Array in World Data

Influence of Fin Structure

In the author's opinion, the fin structure has a strong influence on the fluidelastic stability of tube arrays regardless their geometry. Figure 4-6 shows the relationship between critical reduced velocity and effective pitch ratio which includes the fin geometries like fin height, fin thickness and fin pitch. Robert Lumsden's data ^[21] is also included here. The point A from his experiment is for the bare tube in the rotated square array, its critical velocity is not clearly defined due to the strain sensor failure. If not including this exception, generally, this figure shows that the fin structure tends to decrease the difference between the normal triangular arrangement and the parallel triangular arrangement in fluidelastic instability as the fin density increases. Moreover, it seems that there is an optimum fin pitch at which the finned tube array has the highest critical reduced velocity among the related tubes.

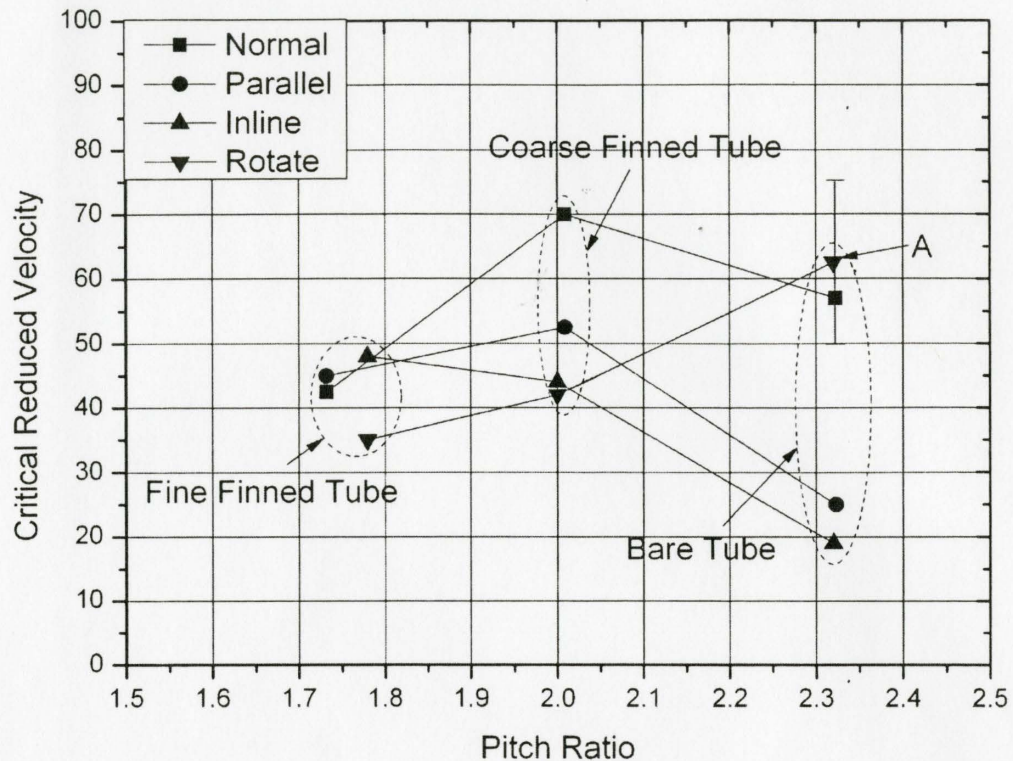


Figure 4-6 Critical Reduced Velocity vs. Effective Pitch Ratio

These judgments are reasonable because the actual finned tubes are quite different from their equivalent bare tubes in topologic structure. For an effective diameter, its minimum value is the base diameter of a finned tube if the fin density is equal to zero, while its maximum value is equal to the fin diameter if the fin density is close to infinity. The effective diameter of an actual finned tube will be between these two extreme conditions. There is evidence that may help to explain why a finned tube may respond differently from its equivalent bare tube. The schematic velocity profile of a finned tube is quite different from its equivalent bare tube as shown in Figure 4-7. The influence of this difference in velocity profile on the tube needs further investigation (CFD simulation is enough for the further study). Basically, the complex fin structure seems not to be captured by the concept of effective diameter.

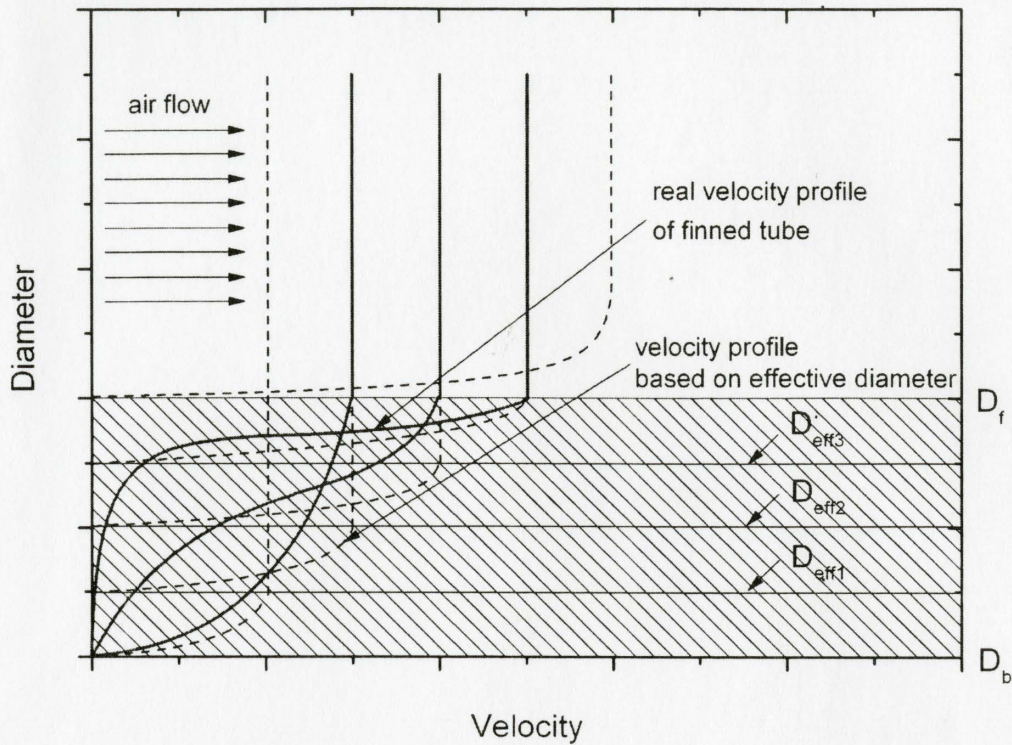


Figure 4-7 Schematic Velocity Profile of Finned Tube

On the other hand, only two data points (3.3fpi and 5.7fpi) between the two extreme boundary points (data points for bare tubes are assumed to be known) are available for the normal triangle and parallel triangle tube arrays in the current study. There is not enough data to make a solid conclusion here. More experimental investigations are needed to determine the influence of fin density on the velocity threshold.

Chapter 5

CONCLUSIONS AND RECOMMENDATIONS

In the course of this study, experiments were conducted to study fluidelastic instability in normal and parallel triangle finned tube arrays. For each array geometry, 8.4mm/3.3fpi and 4.2mm/5.7fpi finned tubes and bare tubes were considered. The tube pitch and mass ratio were kept constant. The principal conclusions are drawn as follows:

- 1) From the experiments, the critical velocities in normal and parallel triangle tube arrays for coarse finned tubes are substantially delayed by the addition of serrated fins, even though the addition of fins is to reduce the effective pitch ratio.
- 2) Compared with coarse finned tubes, the stability thresholds for fine finned tubes decrease as their fin density increases.
- 3) The fin structures strongly influence the fluidelastic stability of finned tube bundles, and they tend to delay the onset of instability.
- 4) The present experiments suggest that there exists an optimum fin pitch value at which a finned tube bundle has a higher critical reduced velocity than its corresponding bare tube bundle. More research is needed to establish this.

RECOMMENDATIONS

Experimental and numerical investigations are suggested to study the influence of the fin density on the fluidelastic instability of finned tube bundles.

REFERENCES

- 1) D.S. Weaver, S.Ziada, M.K.Au-Yang, S.S.Chen, M.P. Païdoussis, M.J. Pettigrew, "Flow Induced Vibrations in Power and Process Plant Components Progress and Prospects", *J. of Pressure Vessel Technology*, ASME, Vol. 122, pp339-348, 2000.
- 2) R. D. Blevins, "Flow Induced Vibration", Krieger Publishing Company, second edition, 2001.
- 3) H. J. Connors Jr., "Fluid elastic vibration of tube arrays excited by cross flow Flow-Induced Vibrations of Heat Exchangers", ASME, pp. 42-56, 1970.
- 4) J.H. Lever and D.S. Weaver, "On the stability of heat exchanger tube bundles, Part 1: Modified Theoretical Model", *J. of Sound and Vibration*, 107(3), 375-392, 1986.
- 5) S. S. Chen and J. A. Jendrzejczyk, "Flow velocity dependence of damping in tube arrays subject to liquid cross-flow". *Journal of Pressure Vessel Technology*, 103, pp. 130-135, 1981.
- 6) D. S. Weaver and M. ElKashlan, "On the number of tube rows required to study cross-flow induced vibrations in tube banks". *Journal of Sound and Vibration*, 75(2), pp. 265-273, 1981.
- 7) S. J. Price, "An Investigation on the Use of Connors' Equation to Predict Fluid elastic Instability in Cylinder Arrays", *Trans. of ASME*, Vol. 123, pp 448-453, Nov 2001.
- 8) D.S. Weaver and J.A. Fitzpatrick, "A Review of Cross Flow Induced Vibrations in Heat Exchanger Tube Arrays", *J. of Fluids and Structures*, (2), 73-93, 1988.
- 9) M. Yetisir and D.S. Weaver, "An unsteady theory for fluidelastic instability in an array of flexible tubes in cross-flow Part I: theory", *J. of Fluids and Structures*, 7, 751-766, 1993.
- 10) S.J. Price, "A review of theoretical models for fluidelastic instability of cylinder arrays in cross-flow", *J. of Fluid and Structures*, 9, 463-518, 1995.
- 11) K. Schröder and H. Gelbe, "New design recommendations for fluid elastic instability in heat exchanger tube bundles". *Journal of Fluids and Structures*, 13, pp. 361-379, 1999.
- 12) W.M. Rohsenow, J.P. Hartnett, and E.N. Gani, "Handbook of Heat Transfer Applications", McGraw-Hill, 2nd edition, 1985.

- 13) W.M. Kays and A.L. London, "Compact Heat Exchangers", McGraw-Hill, New York, 3rd edition, 1993.
- 14) D. R. Reid and J. Taborek, "Selection criteria for plain and segmented finned tubes for heat recovery systems". *Journal of Engineering for Gas Turbines and Power*, 116, pp. 406-410, 1994.
- 15) W.A. Mair, P.D.F. Jones, and R.K.W. Palmer, "Vortex shedding from finned tubes". *Journal of Sound and Vibration*, 39(3), pp. 293-296, 1975.
- 16) K. Hirota, T. Nakamura, H. Kikuchi, K. Isozaki, and H. Kawahara, "Fluid elastic and vortex induced vibration of a finned tube array", *ASME Proceedings of IMECE2002*, New Orleans, Paper No. 32793, 2002.
- 17) B.N. Ryu, K.C. Kim, and J.S. Boo, "The effect of serrated fins on the flow around a circular cylinder", *KSME International Journal*, 17(6), pp.925-934, 2003.
- 18) M. Kienböck, "Vibration characteristics of finned tubes with small fins". *VGB Kraftwerkstechnik*, 62(7), pp. 498-506, English translation, 1982.
- 19) H. Halle, B. L. Boers, and M.W. Wambsganss, "Flow-induced tube vibration thresholds in heat exchangers from shell side water tests". ASME Symposium on Flow-Induced Vibrations, Vol. 3, New Orleans, pp. 17-32. 1984.
- 20) R.H. Lumsden and D.S. Weaver, "Fluid elastic instability in finned tube bundles". Proceedings of CSME Forum 2006, Kananaskis Village, Alberta, Canada, May 21-24. 2006.
- 21) R.H. Lumsden and D.S. Weaver, "The Effect of Fins on Fluidelastic Instability in In-line and Rotated Square Arrays", Proceeding of ASME Pressure Vessels and Piping Division Conference, Texas, 2007.
- 22) User's Manual of HP 35670a Dynamic Signal Analyzer, 1992.
- 23) User's Manual of Origin pro 8.0, student version, 2008.
- 24) D.S. Weaver, S. Ziada, Z. Sun, and P.Feenstra, "The Effect pf Platen Fins on the Flow-Induced Vibrations of an In-Line Tube Array", *Journal of Pressure Vessel Technology*, Vol. 123, pp 437-441, 2001.

APPENDIX A

MODELING OF FLUIDELASTIC INSTABILITY IN FINNED TUBE BUNDLES IN STAGGERED ARRANGEMENT

A theoretical model is introduced to analyze the fluidelastic instability of finned tube bundles. The fins are not modeled in detail but rather accounted for as a bare tube with an "effective diameter". The author developed a mathematical model to predict the critical velocity of finned tube bundles in staggered arrangement.

This fluidelastic instability theory was transcribed from the author's project report for the course, Flow Induced Vibrations (ME723), at McMaster University in 2008. The origin of the methodology is from the semi-analytical model developed by Lever and Weaver^[4], but there are significant differences between these two models: in the new model all the tubes are flexible and oscillate only in transverse direction; the tube array is a staggered arrangement; the fluid flow channel is composed of several simple sub-domains where fluid flow is treated using different strategies; and tube fins are taken into account in terms of an effective diameter.

A1 One Dimensional Unstable Flow of Incompressible Ideal Fluid

The continuity equation in integral form, for a one dimensional unsteady flow of incompressible ideal fluid, is given by:

$$\oint_A \rho U = Q(t)$$

and the momentum equation is given by:

$$\int_0^l \frac{dU}{dt} dl + \int_0^l d \left(\frac{U^2}{2} + \psi + \frac{\tilde{P}}{\rho} \right) = C(t)$$

where ρ is fluid density, U is fluid velocity, \tilde{P} is pressure, ψ is gravity potential, A is the cross-section area, l_0 and l are the path-line initial point and ending point, Q is time-dependent

mass flux, and C is a time-dependent constant.

In the present study, the mass flux is assumed to be constant, i.e. $Q(t)=const$. The unsteady flow is defined fully by the unsteady boundary conditions. The gravity potential is zero since the fluid flow is assumed to be at the same level. Therefore, the equations can be rewritten as follows:

$$\oint_A \rho U = Q$$
$$\int_0^l \frac{dU}{dt} dl + \left(\frac{U^2}{2} + \frac{\tilde{P}}{\rho} \right) = C(t)$$

A2 Fluidelastic Instability Simulation

The derivation of this fluidelastic instability model for tube bundles is based upon the following basic assumptions:

1. A one dimensional unsteady flow of incompressible ideal fluid;
2. The incompressible fluid should abide by the fluid inertia assumption suggested by Lever and Weaver^[4] so the fluid can be equally distributed into each fluid channel;
3. According to the fluid inertia assumption, the inviscid flow doesn't change its direction;
4. All tubes in a tube array oscillate only in transverse direction except the fixed ones on the boundaries.

To simulate the fluidelastic instability of the tube bundle, it is assumed that there is an imaginary unit cell, as shown in Figure A-1. There are two smooth channels passing over the center tube, called the left and right channels. The ideal fluid is assumed to flow along these channels. In this cell, a center tube is surrounded by four tubes in a staggered arrangement. The two downstream tubes are assumed to have no influence on the center tube. It is sufficient for us to model the left and right hatched domains only.

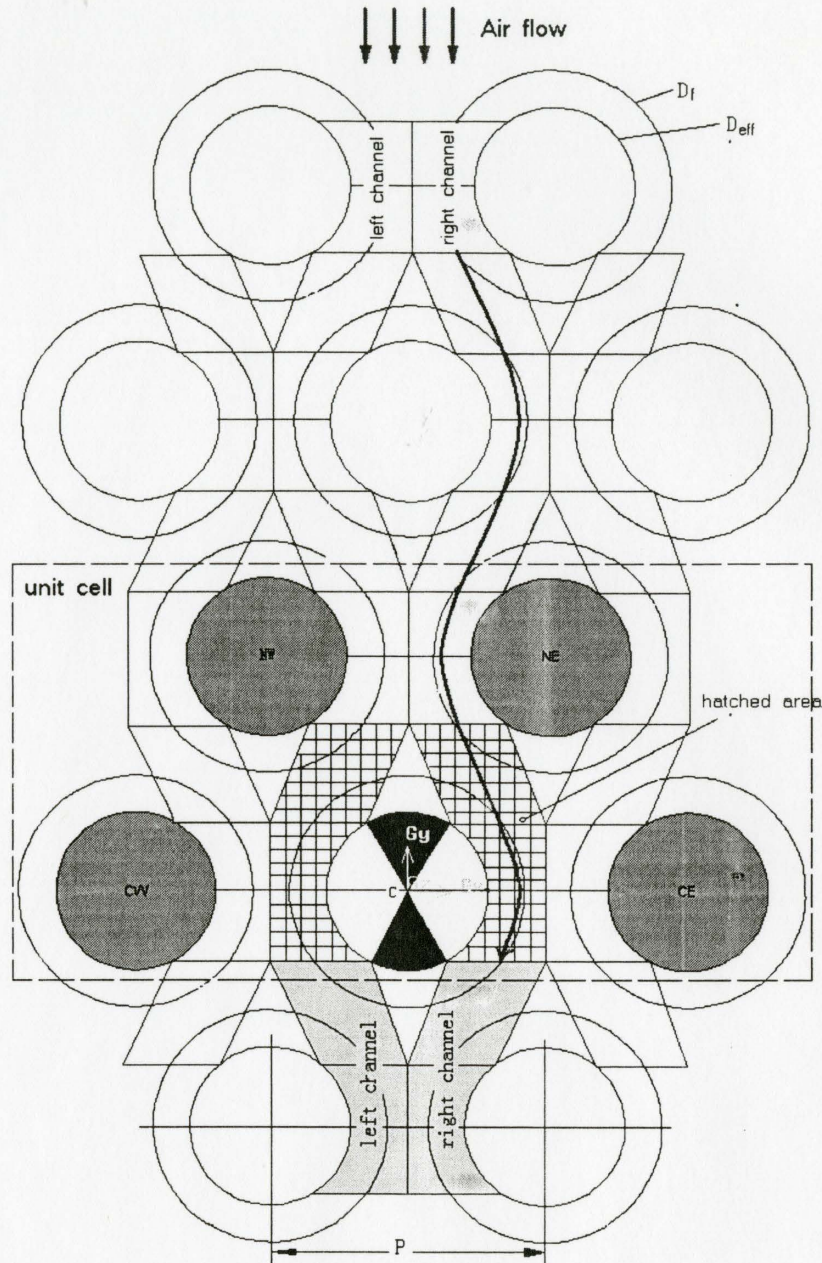


Figure A-1 Fluidelastic Instability Simulation

The left domain is further divided into several sub-domains as shown in Figure A-2. The upper sub-domain is in the form of a trapezium consisting of four points, p_1 , p_{NW} , W_2 , and p_{12} . This trapezium is transformable as the movements of related tubes. The lower sub-domain is in an arch form consisting of four points, W_2 , W_4 , p_{14} , and p_{12} . This sub-domain acts like a cylinder with a piston for it is compressed and expanded repeatedly as the center tube moves back and

forth in the transverse direction. The point p_1 is the separation point at the forked position of the left and right channels, and is the center point of line p_{NW} - p_{NE} . Similarly, the line W_2 - W_3 - W_4 is assumed to always make the neighboring fluid channels between the center tube and center-west tube in two equal sub-domains to keep the pressures in both sides balanced. The arc curve p_{12} - p_{13} - p_{14} is the zone for fluid-tube interaction, which is noted by the pressure acting angle 2θ . For the case of one dimensional flow, it is enough to know the normal velocity at several key areas, such as A_{11} , A_{12} , A_{13} , and A_{14} , among which A_{13} is the minimum cross-section area at the tube gap. The path-line is assumed to be composed by the line l_m and arc curve l_θ , which is located roughly in the center of the left channel. The magnitudes of the line l_m and arc curve l_θ , are calculated by computing their lengths before vibration. The right section is subject to the same conditions.

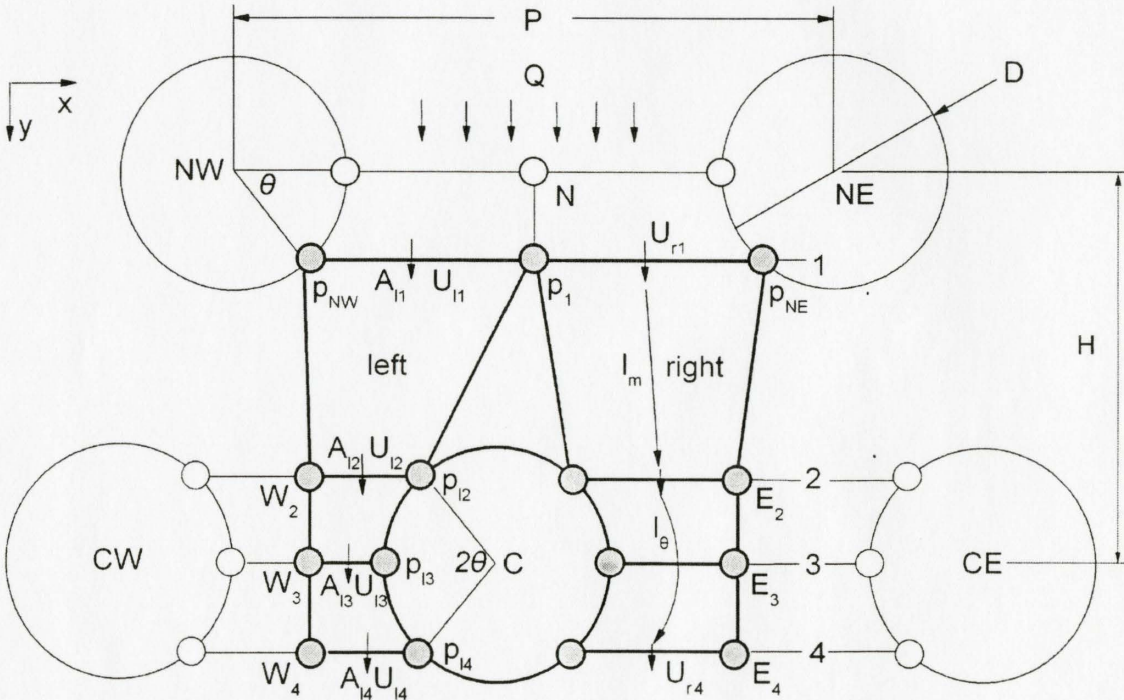


Figure A-2 Sub-domains of Left and Right Channels

The fluid flows in the left and right domains are assumed to be dominated by the above key variable areas due to the fluctuations in displacement of related tubes. However, since the

interactions of fluid-solid in the left and right lower sub-domains are crucial to define the fluidelastic instability, the calculations of the pressure distributions at the arc zone on both sides of the center tube should be carefully done. This will be discussed in the next section.

A3 Fluidelastic Vibration Equation (FVE)

Derivation of Fluidelastic Vibration Equation

Based on the above simplified assumptions regarding the imaginary cell, a mathematical model is built to predict tube stability. Since the tubes vibrate only in the x direction, the coordinates of each tube at its equilibrium position are noted as: $X_{NW}^0, X_{NE}^0, X_C^0, X_{CW}^0$, and, X_{CE}^0 .

To produce the initial random positions of tubes (which are important to solve the FEV equation numerically), the amplitudes of the tubes are assumed to be: $A_{NW}^0, A_{NE}^0, A_C^0, A_{CW}^0$, and, A_{CE}^0 , and the corresponding initial phases are: $\varphi_{NW}^0, \varphi_{NE}^0, \varphi_C^0, \varphi_{CW}^0$, and, φ_{CE}^0 .

The random positions of tubes at an initial time can be given by:

$$\begin{aligned} X_{NW} &= X_{NW}^0 + A_{NW}^0 \cos(\omega t + \varphi_{NW}^0) \\ X_{NE} &= X_{NE}^0 + A_{NE}^0 \cos(\omega t + \varphi_{NE}^0) \\ X_C &= X_C^0 + A_C^0 \cos(\omega t + \varphi_C^0) \\ X_{CW} &= X_{CW}^0 + A_{CW}^0 \cos(\omega t + \varphi_{CW}^0) \\ X_{CE} &= X_{CE}^0 + A_{CE}^0 \cos(\omega t + \varphi_{CE}^0) \end{aligned}$$

where ω is the circular frequency and t is the time.

The coordinates of three gap center points, W_3 , E_3 , and N around the center tube are noted to be: X_N, X_E, X_W , which can be calculated by:

$$\begin{aligned} X_N &= \frac{X_{NW} + X_{NE}}{2} \\ X_W &= \frac{X_{CW} + X_C}{2} \\ X_E &= \frac{X_{CE} + X_C}{2} \end{aligned}$$

For convenience, noting the displacement of each tube as:

$$\begin{aligned}
x_{NW} &= X_{NW} - X_{NW}^0 \\
x_{NE} &= X_{NE} - X_{NE}^0 \\
x_C &= X_C - X_C^0 \\
x_{CW} &= X_{CW} - X_{CW}^0 \\
x_{CE} &= X_{CW} - X_{CE}^0
\end{aligned}$$

The four key cross-section areas at the left channel are computed by:

$$\begin{aligned}
A_{l1} &= (X_N - X_{NW} - \frac{D \cos \theta}{2}) = \frac{P - D \cos \theta + x_{EN} - x_{NW}}{2} \\
A_{l2} = A_{l4} &= (X_C - X_W - \frac{D \cos \theta}{2}) = \frac{P - D \cos \theta + x_C - x_{CW}}{2} \\
A_{l3} &= X_C - X_W - \frac{D}{2} = \frac{P - D + x_C - x_{CW}}{2}
\end{aligned}$$

where P is the tube pitch, and D is the finned tube effective diameter.

The four key cross-section areas at the right channel are computed by:

$$\begin{aligned}
A_{r1} &= (X_{NE} - X_N - \frac{D \cos \theta}{2}) = \frac{P - D \cos \theta + x_{EN} - x_{NW}}{2} \\
A_{r2} = A_{r4} &= (X_E - X_C - \frac{D \cos \theta}{2}) = \frac{P - D \cos \theta + x_{CE} - x_C}{2} \\
A_{r3} &= X_E - X_C - \frac{D}{2} = \frac{P - D + x_{CE} - x_C}{2}
\end{aligned}$$

The cross-section areas within the lower sub-domain are a function of angle ϑ , which are:

$$\begin{aligned}
\text{Left domain: } A_{l\vartheta} &= (X_C - X_W - \frac{D \cos \vartheta}{2}) \\
&\text{where } -\theta \leq \vartheta \leq \theta \\
\text{Right domain: } A_{r\vartheta} &= (X_E - X_C - \frac{D \cos \vartheta}{2}) \\
&\text{where } -\theta \leq \vartheta \leq \theta
\end{aligned}$$

The pressure acting angle 2θ along which the fluid force acts on the tube surface is assumed to be fixed while the tube oscillates back and forth in the transverse direction. The mass flow rate in each channel is assumed to be the same, therefore, the continuity equations is:

$$\text{Left domain: } \rho U_l A_l = Q/2$$

$$\text{Right domain: } \rho U_r A_r = Q/2$$

Specifically, the velocity distributions along the left and right domains are

$$U_{11}A_{11} = U_{12}A_{12} = U_{13}A_{13} = U_{14}A_{14} = U_l(\mathcal{G})A_{l\mathcal{G}}$$

$$U_{r1}A_{r1} = U_{r2}A_{r2} = U_{r3}A_{r3} = U_{r4}A_{r4} = U_r(\mathcal{G})A_{r\mathcal{G}}$$

The unstable one dimensional inviscid momentum equations can be written as:

$$\text{Left domain: } \int \frac{dU_l}{dt} dx + \frac{U_l^2}{2} + \frac{\tilde{P}_l}{\rho} = C_l(t)$$

$$\text{Right domain: } \int \frac{dU_r}{dt} dx + \frac{U_r^2}{2} + \frac{\tilde{P}_r}{\rho} = C_r(t)$$

or:

$$\int_{\tilde{l}} \frac{dU_l}{dt} d\tilde{l} + \frac{(U_l)^2}{2} + \frac{\tilde{P}_l}{\rho} = \frac{(U_{l1})^2}{2} + \frac{\tilde{P}_{l1}}{\rho}$$

$$\int_{\tilde{l}} \frac{dU_r}{dt} d\tilde{l} + \frac{(U_r)^2}{2} + \frac{\tilde{P}_r}{\rho} = \frac{(U_{r1})^2}{2} + \frac{\tilde{P}_{r1}}{\rho}$$

where \tilde{l} is the total length of the center path line of fluid flow in the left domain consisting of a straight line, l_m is the length of the straight line before vibration which is regarded as its average length and is approximately regarded as a constant, and l_θ is an arc curve which can be considered to be a circular curve and roughly equal to $2r\theta$ in length, noting that r is the effective radius of the finned tube, $r=D/2$.

The pressure in the left domain can be rewritten as:

$$\tilde{P}_l = \left[\frac{\rho(U_{l1})^2}{2} + \tilde{P}_{l1} \right] - \frac{\rho(U_l)^2}{2} - \rho \int_{\tilde{l}} \frac{dU_l}{dt} d\tilde{l}$$

Therefore, the fluid force acting on the left arc zone of the center tube can be computed by integrating the pressure along the curve $p_{12}-p_{13}-p_{14}$.

$$\begin{aligned}
F_l(t) &= \int_{\theta} [\tilde{P}_l] \cos \vartheta dl_{\theta} \\
&= \int_{\theta} \left\{ \left[\frac{\rho(U_{11})^2}{2} + \tilde{P}_{11} \right] - \frac{\rho(U_l)^2}{2} - \rho \int_b^{\tilde{l}} \frac{dU_l}{dt} d\tilde{l} \right\} \cos \vartheta r d\vartheta \\
&= \int_{\theta} \left\{ \rho C_l - \frac{\rho}{2} \left(\frac{A_{11}}{A_{1\vartheta}} U_{11} \right)^2 - \rho \frac{d}{dt} \int_b^{\tilde{l}} \left(\frac{A_{11}}{A_{1\tilde{l}}} U_{11} \right) d\tilde{l} \right\} \cos \vartheta r d\vartheta \\
&= \int_{\theta} \rho C_l r \cos \vartheta d\vartheta - \frac{\rho}{2} (A_{11} U_{11})^2 \int_{\theta} \frac{r \cos \vartheta}{(X_c - X_w - r \cos \vartheta)^2} d\vartheta - \rho r \frac{d}{dt} \int_{\theta} \int_b^{\tilde{l}} \left(\frac{A_{11}}{A_{1\tilde{l}}} U_{11} \right) d\tilde{l} \cos \vartheta d\vartheta \\
&= 2\rho C_l r \sin \theta - \frac{\rho}{2} (A_{11} U_{11})^2 \int_{\theta} \frac{r \cos \vartheta}{(X_c - X_w - r \cos \vartheta)^2} d\vartheta \\
&\quad - \rho r \frac{d}{dt} \int_{\theta} \left\{ \int_b^m \left(U_{11} + \frac{U_{12} - U_{11}}{l_m} \tilde{l} \right) d\tilde{l} + \int_m^{\theta} \left(\frac{A_{11} U_{11}}{X_c - X_w - r \cos \vartheta} \right) d\tilde{l} \right\} \cos \vartheta d\vartheta \\
&= 2\rho C_l r \sin \theta - \frac{\rho}{2} (A_{11} U_{11})^2 \int_{\theta} \frac{r \cos \vartheta}{(X_c - X_w - r \cos \vartheta)^2} d\vartheta \\
&\quad - \rho r l_m \sin \theta \frac{d}{dt} (U_{11} + U_{12}) + \rho r \frac{d}{dt} \int_{\theta} \int_{\theta} \left(\frac{A_{11} U_{11}}{X_c - X_w - r \cos \vartheta} \right) r d\vartheta \cos \vartheta d\vartheta
\end{aligned}$$

where l_{θ} is the arc curve part of the center path-line, $2r\theta$, C_l equals to $\frac{(U_{11})^2}{2} + \frac{\tilde{P}_{11}}{\rho}$.

Velocity Profile along Arc Zone of the Pressure Acting Angle

Since the integration of the second and fourth terms is complex, a second order parabolic profile of U_l in the lower sub-domain is assumed by interpolation passing through three points, U_{12} , U_{13} , and U_{14} , to simplify the calculation. It is then supposed that: $U_l(r\vartheta) = a + b(r\vartheta) + c(r\vartheta)^2$.

Substituting the boundary conditions into this equation, we have:

$$\begin{aligned}
U_l(0) &= a_1 = U_{13} \\
U_l(-r\theta) &= a_1 - b_1(r\theta) + c_1(r\theta)^2 = U_{12} \\
U_l(r\theta) &= a_1 + b_1(r\theta) + c_1(r\theta)^2 = U_{14}
\end{aligned}$$

Hence $U_l(r\vartheta) = U_{13} + \frac{U_{12} - U_{13}}{(r\theta)^2} (r\vartheta)^2$. Then the forces can be rewritten as:

$$\begin{aligned}
F_l(t) &= \int_{-\theta}^{\theta} \left\{ \left[\frac{\rho(U_{11})^2}{2} + \tilde{P}_{11} \right] - \frac{\rho(U_1)^2}{2} - \rho \int_{\tilde{l}} \frac{dU_1}{dt} d\tilde{l} \right\} \cos \theta r d\theta \\
&= \int_{-\theta}^{\theta} \rho C_l r \cos \theta d\theta - \frac{\rho r}{2} \int_{-\theta}^{\theta} \left[U_{13} + \frac{U_{12} - U_{13}}{(r\theta)^2} (r\theta)^2 \right]^2 \cos \theta d\theta \\
&\quad - \rho r \frac{d}{dt} \int_{-\theta}^{\theta} \left\{ \int_m^m \left(U_{11} + \frac{U_{12} - U_{11} \tilde{l}}{l_m} \right) d\tilde{l} + \int_m^m \left[U_{13} + \frac{U_{12} - U_{13}}{(r\theta)^2} (r\theta)^2 \right] d\tilde{l} \right\} \cos \theta d\theta \\
&= 2\rho C_l r \sin \theta - \rho r U_{13}^2 \sin \theta - \rho r^3 \frac{U_{12} U_{13} - U_{13}^2}{(r\theta)^2} [(2\theta^2 - 4) \sin \theta + 4\theta \cos \theta] \\
&\quad - \rho r^5 \frac{(U_{12} - U_{13})^2}{(r\theta)^4} [(\theta^4 - 12\theta^2 + 24) \sin \theta + (4\theta^3 - 24\theta) \cos \theta] \\
&\quad - \rho r l_m \sin \theta \frac{d}{dt} (U_{11} + U_{12}) - \rho r \frac{d}{dt} \int_{-\theta}^{\theta} \left\{ \int_{\theta}^{\theta} \left[U_{13} + \frac{U_{12} - U_{13}}{(r\theta)^2} (r\theta)^2 \right] d(r\theta) \right\} \cos \theta d\theta \\
&= \rho r \left[\frac{2 \sin \theta C_l - \sin \theta U_{13}^2 - \frac{(2\theta^2 - 4) \sin \theta + 4\theta \cos \theta}{\theta^2} (U_{12} U_{13} - U_{13}^2)}{(\theta^4 - 12\theta^2 + 24) \sin \theta + (4\theta^3 - 24\theta) \cos \theta} (U_{12} - U_{13})^2 \right] \\
&\quad - \rho r l_m \sin \theta \frac{d}{dt} (U_{11} + U_{12}) - \rho r \frac{d}{dt} \int_{-\theta}^{\theta} \left\{ (r\theta) \frac{U_{12} + 2U_{13}}{3} + (r\theta) U_{13} + (r\theta)^3 \frac{U_{12} - U_{13}}{3(r\theta)^2} \right\} \cos \theta d\theta \\
&= \rho r \left[\frac{2 \sin \theta C_l - \sin \theta U_{13}^2 - \frac{(2\theta^2 - 4) \sin \theta + 4\theta \cos \theta}{\theta^2} (U_{12} U_{13} - U_{13}^2)}{(\theta^4 - 12\theta^2 + 24) \sin \theta + (4\theta^3 - 24\theta) \cos \theta} (U_{12} - U_{13})^2 \right] \\
&\quad - \rho r l_m \sin \theta \frac{d}{dt} (U_{11} + U_{12}) - 2\rho r^2 \theta \sin \theta \frac{d}{dt} \left(\frac{U_{12} + 2U_{13}}{3} \right)
\end{aligned}$$

Similarly, the force on the right side of the center tube is:

$$\begin{aligned}
F_r(t) &= \rho r \left[\frac{2 \sin \theta C_r - \sin \theta U_{r3}^2 - \frac{(2\theta^2 - 4) \sin \theta + 4\theta \cos \theta}{\theta^2} (U_{r2} U_{r3} - U_{r3}^2)}{(\theta^4 - 12\theta^2 + 24) \sin \theta + (4\theta^3 - 24\theta) \cos \theta} (U_{r2} - U_{r3})^2 \right] \\
&\quad - \rho r l_m \sin \theta \frac{d}{dt} (U_{r1} + U_{r2}) - 2\rho r^2 \theta \sin \theta \frac{d}{dt} \left(\frac{U_{r2} + 2U_{r3}}{3} \right)
\end{aligned}$$

$$E_1 = \sin \theta$$

Noting that:

$$E_2 = \frac{(2\theta^2 - 4)\sin \theta + 4\theta \cos \theta}{\theta^2}$$

$$E_3 = \frac{(\theta^4 - 12\theta^2 + 24)\sin \theta + (4\theta^3 - 24\theta)\cos \theta}{\theta^4}$$

$$E_4 = \theta \sin \theta$$

The total force on the tube is then computed by:

$$\begin{aligned} F_l(t) - F_r(t) = & \rho \left\{ 2E_1(C_l - C_r) - E_1(U_{l3}^2 - U_{r3}^2) - E_2[(U_{l2}U_{l3} - U_{r3}^2) - (U_{r2}U_{r3} - U_{r3}^2)] - E_3[(U_{l2} - U_{l3})^2 - (U_{r2} - U_{r3})^2] \right\} \\ & - \rho \left\{ l_m E_1 \frac{d}{dt} [(U_{l1} + U_{l2}) - (U_{r1} + U_{r2})] + 2r E_4 \frac{d}{dt} \left[\left(\frac{U_{l2} + 2U_{l3}}{3} \right) - \left(\frac{U_{r2} + 2U_{r3}}{3} \right) \right] \right\} \end{aligned}$$

where

$$U_{l2} = U_{l1} \frac{A_{l1}}{A_{l2}} = k_{l1-2} U_{l1}$$

$$U_{l3} = U_{l1} \frac{A_{l1}}{A_{l3}} = k_{l1-3} U_{l1}$$

$$U_{r2} = U_{r1} \frac{A_{r1}}{A_{r2}} = k_{r1-2} U_{r1}$$

$$U_{r3} = U_{r1} \frac{A_{r1}}{A_{r3}} = k_{r1-3} U_{r1}$$

and

$$k_{l1-2} = \frac{X_{NE} - X_{NW} - 2r \cos \theta}{X_C - X_{CW} - 2r \cos \theta} = \frac{P - D \cos \theta + x_{NE} - x_{NW}}{P - D \cos \theta + x_C - x_{CW}}$$

$$k_{l1-3} = \frac{X_{NE} - X_{NW} - 2r \cos \theta}{X_C - X_{CW} - 2r} = \frac{P - D \cos \theta + x_{NE} - x_{NW}}{P - D + x_C - x_{CW}}$$

$$k_{r1-2} = \frac{X_{NE} - X_{NW} - 2r \cos \theta}{X_{CE} - X_C - 2r \cos \theta} = \frac{P - D \cos \theta + x_{NE} - x_{NW}}{P - D \cos \theta + x_{CE} - x_C}$$

$$k_{r1-3} = \frac{X_{NE} - X_{NW} - 2r \cos \theta}{X_{CE} - X_C - 2r} = \frac{P - D \cos \theta + x_{NE} - x_{NW}}{P - D + x_{CE} - x_C}$$

and x_{NE} , x_{NW} , x_C , x_{CW} , and x_{CE} are the displacements of these tubes. Assuming the velocities across the area p_l - p_{NW} and p_l - p_{NE} are the same, i.e. $U_{l1} = U_{r1}$, and $C_l = C_r$, the gap velocity is given by:

$$U_g = \frac{Q}{\rho(P - D)}$$

Then, the relationship is further reduced to:

$$F_l(t) - F_r(t) = \frac{\rho D(P-D)^2 U_g^2}{2(P-D \cos \theta + x_{NE} - x_{NW})^2} \left\{ E_1(k_{l1-3}^2 - k_{r1-3}^2) + E_2[(k_{l1-2} - k_{l1-3})k_{l1-3} - (k_{r1-2} - k_{r1-3})k_{r1-3}] \right. \\ \left. + E_3[(k_{l1-2} - k_{l1-3})^2 - (k_{r1-2} - k_{r1-3})^2] \right\} \\ - \frac{\rho D^2 U_g}{2} \left\{ E_1 \frac{l_m}{D} \frac{d}{dt} \left[(k_{l1-2} - k_{r1-2}) \frac{(P-D)}{P-D \cos \theta + x_{NE} - x_{NW}} \right] + \right. \\ \left. E_4 \frac{d}{dt} \left[\left(\frac{k_{l1-2} - k_{r1-2}}{3} + 2 \frac{k_{l1-3} - k_{r1-3}}{3} \right) \frac{(P-D)}{P-D \cos \theta + x_{NE} - x_{NW}} \right] \right\}$$

Once the force is obtained, the motion of the tube could be computed by solving the following vibration equation

$$m \frac{\partial^2 x_c}{\partial t^2} + c \frac{\partial x_c}{\partial t} + kx_c = -(Dis + Vel)$$

where

$$Dis = \frac{\rho D U_g^2}{2} \frac{(P-D)^2}{(P-D \cos \theta + x_{NE} - x_{NW})^2} \left\{ E_1(k_{l1-3}^2 - k_{r1-3}^2) + E_2[(k_{l1-2} - k_{l1-3})k_{l1-3} - (k_{r1-2} - k_{r1-3})k_{r1-3}] \right. \\ \left. + E_3[(k_{l1-2} - k_{l1-3})^2 - (k_{r1-2} - k_{r1-3})^2] \right\} \\ Vel = \frac{\rho D^2 U_g}{2} \frac{d}{dt} \left\{ E_1 \frac{l_m}{D} (k_{l1-2} - k_{r1-2}) + E_4 \left(\frac{k_{l1-2} - k_{r1-2}}{3} + 2 \frac{k_{l1-3} - k_{r1-3}}{3} \right) \frac{(P-D)}{P-D \cos \theta + x_{NE} - x_{NW}} \right\}$$

U_g is the gap velocity of air flow, m/s (at the first row)

m is the mass per unit length of tube, kg/m

k is the stiffness or spring constant of tube per unit length, kg/m.s² or N/m²

c is the damping of tube, $c=2m\zeta\omega$, kg/m.s

ζ is the damping factor, $\zeta=\delta/2\eta$

δ is the logarithmic decrement of damping,

ω is the natural frequency of the tube in radians per second, $\omega=2\pi f=\sqrt{k/m}$, 1/s

f is the natural frequency, Hz

ρ is the density of fluid, kg/m³

Let x_{NE} , x_{NW} , x_c , x_{CW} , and x_{CE} be divided by $P-D$, and set time $t=\tau/\omega$; the vibration equation will be converted into dimensionless form:

$$\frac{\partial^2 \hat{x}_c}{\partial \tau^2} + 2\zeta \frac{\partial \hat{x}_c}{\partial \tau} + \hat{x}_c = -(\hat{Dis} + \hat{Vel})$$

where

$$\hat{D}is = \frac{\rho U_g^2}{2m\omega^2} \times \frac{D}{P-D} \times \left[\frac{E_1(\hat{k}_{l-3}^2 - \hat{k}_{r1-3}^2) + E_2[(\hat{k}_{l1-2} - \hat{k}_{l1-3})\hat{k}_{l1-3} - (\hat{k}_{r1-2} - \hat{k}_{r1-3})\hat{k}_{r1-3}] + E_3[(\hat{k}_{l1-2} - \hat{k}_{l-3})^2 - (\hat{k}_{r1-2} - \hat{k}_{r1-3})^2]}{\left(\frac{P-D\cos\theta}{P-D} + \hat{x}_{NE} - \hat{x}_{NW}\right)^2} \right]$$

$$\hat{V}el = \frac{1}{4\pi} \times \frac{U_g}{fD} \times \frac{\rho D^2}{m} \times \frac{D}{P-D} \times \frac{d}{d\tau} \left[\frac{E_1 \frac{l_m}{D} (\hat{k}_{l1-2} - \hat{k}_{r1-2}) + E_4 \left(\frac{\hat{k}_{l1-2} - \hat{k}_{r1-2}}{3} + 2 \frac{\hat{k}_{l1-3} - \hat{k}_{r1-3}}{3} \right)}{\frac{P-D\cos\theta}{P-D} + \hat{x}_{NE} - \hat{x}_{NW}} \right]$$

A new dimensionless number is defined as the dimensionless stiffness of fluid (physically, the ratio of fluid dynamic pressure head to tube stiffness):

$$\hat{k}_f = \frac{\rho U_g^2}{2m\omega^2} = \frac{\rho U_g^2}{2k}$$

\hat{k}_f indicates the elastic behavior of the gap fluid flow, and its stiffness can be changed by varying the fluid flow rate. In addition, we denote:

$$\hat{\alpha} = \frac{D}{P-D} \times \left[\frac{E_1(\hat{k}_{l-3}^2 - \hat{k}_{r1-3}^2) + E_2[(\hat{k}_{l1-2} - \hat{k}_{l1-3})\hat{k}_{l1-3} - (\hat{k}_{r1-2} - \hat{k}_{r1-3})\hat{k}_{r1-3}] + E_3[(\hat{k}_{l1-2} - \hat{k}_{l-3})^2 - (\hat{k}_{r1-2} - \hat{k}_{r1-3})^2]}{\left(\frac{P-D\cos\theta}{P-D} + \hat{x}_{NE} - \hat{x}_{NW}\right)^2} \right]$$

$$\hat{\beta} = \frac{D}{P-D} \times \frac{E_1 \frac{l_m}{D} (\hat{k}_{l1-2} - \hat{k}_{r1-2}) + E_4 \left(\frac{\hat{k}_{l1-2} - \hat{k}_{r1-2}}{3} + 2 \frac{\hat{k}_{l1-3} - \hat{k}_{r1-3}}{3} \right)}{4 \left(\frac{P-D\cos\theta}{P-D} + \hat{x}_{NE} - \hat{x}_{NW} \right)}$$

$\hat{\alpha}$ and $\hat{\beta}$ are concerned with the geometry of the tube array, the pressure acting angle, and the displacements of the five neighboring tubes in the model as shown in Figure 3-2. Since the geometry parameters of the tube array and the acting angle are assumed to be constant,

$\hat{\alpha}$ and $\hat{\beta}$ can be regarded as the generalized displacements of the tube array. Accordingly, $\frac{d}{d\tau}(\hat{\beta})$ can be regarded as the generalized velocity of the tube array. Finally, the dimensionless FVE reduces to:

$$\boxed{\frac{d^2 \hat{x}_C}{d\tau^2} + 2\zeta \frac{d\hat{x}_C}{d\tau} + \hat{x}_C = - \left[\hat{k}_f \times \hat{\alpha} + \frac{1}{\pi} \times \frac{U_g}{fD} \times \frac{\rho D^2}{m} \times \frac{d}{d\tau}(\hat{\beta}) \right]}$$

On the left hand side of the equation is the regular vibration equation with damping. On the right hand side of the equation are two terms: the first one can be defined as a fluid force produced by the relative displacements of the various tubes (fluid stiffness), the second one can be regarded as a force generated by the generalized velocity of the tubes, (fluid damping).

A4 Fluidelastic Instability in Finned Tube Bundle in Staggered Arrangement

Since the above equation combines the motions of five neighboring tubes together, it has to be solved for the whole tube array. However, before solving this equation, it is a good strategy to study a fixed tube array with a single flexible central tube so as to gain an insight into the fluid force generated by the tube displacement and the pressure produced by the tube velocity.

Influence of Damping Component on Tube Damping

For simplicity, assuming all other tubes in the model are fixed except the center tube, the general velocity term, $\frac{d}{d\tau}(\hat{\beta})$, is reduced to:

$$\frac{d}{d\tau}(\hat{\beta}) = \frac{D}{4(P-D)} \times \frac{d}{d\tau} \left[\left(E_1 \frac{l_m}{D} + \frac{E_4}{3} \right) \left(\frac{1}{\frac{P-D \cos \theta}{P-D} + \hat{x}_C} - \frac{1}{\frac{P-D \cos \theta}{P-D} - \hat{x}_C} \right) + \frac{2E_4}{3} \left(\frac{1}{1+\hat{x}_C} - \frac{1}{1-\hat{x}_C} \right) \right]$$

Noting that

$$a = \frac{D}{P-D}, \quad b = \frac{P-D \cos \theta}{P-D}$$

$$\hat{k}_{n-2} = \frac{b}{b + \hat{x}_c}$$

$$\hat{k}_{n-3} = \frac{b}{1 + \hat{x}_c}$$

Therefore

$$\hat{k}_{r1-2} = \frac{b}{b - \hat{x}_c}$$

$$\hat{k}_{r1-3} = \frac{b}{1 - \hat{x}_c}$$

and then:

$$\begin{aligned} \frac{d}{d\tau}(\hat{\beta}) &= \frac{a}{4} \times \left(E_1 \frac{l_m}{D} + \frac{E_4}{3} \right) \frac{d}{d\tau} \left(\frac{1}{b + \hat{x}_c} - \frac{1}{b - \hat{x}_c} \right) + \frac{aE_4}{6} \frac{d}{d\tau} \left(\frac{1}{1 + \hat{x}_c} - \frac{1}{1 - \hat{x}_c} \right) \\ &= - \left\{ \frac{a}{4} \left(E_1 \frac{l_m}{D} + \frac{E_4}{3} \right) \left[\frac{1}{(b + \hat{x}_c)^2} + \frac{1}{(b - \hat{x}_c)^2} \right] + \frac{aE_4}{6} \left[\frac{1}{(1 + \hat{x}_c)^2} + \frac{1}{(1 - \hat{x}_c)^2} \right] \right\} \frac{d\hat{x}_c}{d\tau} \\ &= -\beta^{-1} \frac{d\hat{x}_c}{d\tau} \end{aligned}$$

The FVE becomes:

$$\frac{\partial^2 \hat{x}_c}{\partial \tau^2} + \left(2\zeta - \frac{1}{\pi} \times \frac{U_g}{fD} \times \frac{\rho D^2}{m} \times \beta^{-1} \right) \frac{\partial \hat{x}_c}{\partial \tau} + \hat{x}_c = -\hat{k}_f \times \hat{\alpha}$$

According to the velocity mechanism, the fluidelastic instability is caused by negative damping. Therefore the critical equation for fluidelastic instability is:

$$2\zeta - \frac{1}{\pi} \times \frac{U_g}{fD} \times \frac{\rho D^2}{m} \times \beta^{-1} = 0$$

Therefore, the critical reduced velocity is given by:

$$\boxed{\begin{aligned} \left(\frac{U_g}{fD} \right)_{cr} &= \beta \left[\frac{m(2\pi\zeta)}{\rho D^2} \right] \\ \text{where } \beta &= \left\{ \frac{a}{4} \left(E_1 \frac{l_m}{D} + \frac{E_4}{3} \right) \left[\frac{1}{(b + \hat{x}_c)^2} + \frac{1}{(b - \hat{x}_c)^2} \right] + \frac{aE_4}{6} \left[\frac{1}{(1 + \hat{x}_c)^2} + \frac{1}{(1 - \hat{x}_c)^2} \right] \right\}^{-1} \end{aligned}}$$

It can be shown that the coefficient β is a variable coefficient which is dependent on the geometry of the tube array, the pressure acting angle of fluid, and the displacement or permitted amplitude of tube. Therefore, from the above equation it is seen that the tube displacement has a direct

influence on fluidelastic instability even though it may not be the primary cause. Obviously, the pressure term affects the damping of the vibration system and may take the net tube damping from positive to negative. Thus $\frac{d}{d\tau}(\hat{\beta})$ represents the velocity mechanism of fluidelastic instability.

Understanding the Negative Damping Mechanism in Tube Array

The negative damping item has been derived mathematically in the current theory. This section discusses the author's understanding on the negative damping produced by fluid flow in the tube array, which is physically a "lift effect" depending on the increment of the tube displacement per unit time or, in other words, the tube velocity.

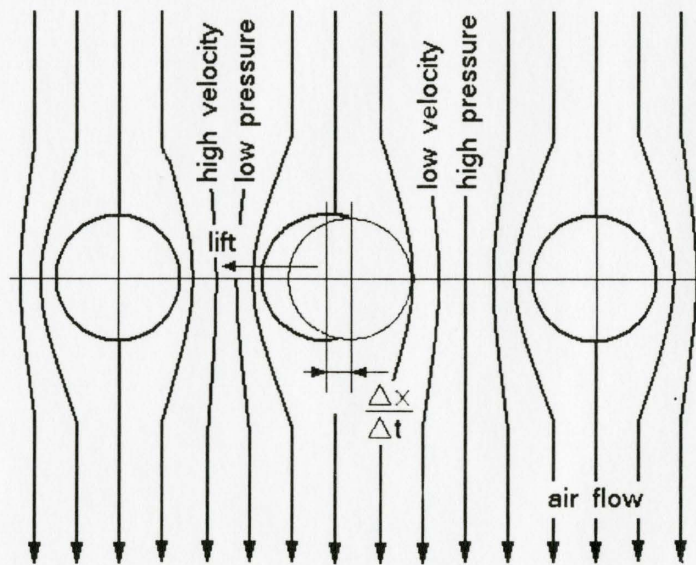


Figure A-3 Lift Effect Due to Tube Velocity

When there is an increment of the tube displacement at a unit timeslot as shown in Figure A-3, according to the fluid inertia assumption, the mass flux will keep constant in both the left flow channel and the right flow channel of the center tube. Accordingly, the high velocity and low pressure will be in the left channel and the low velocity and high pressure will be in the right channel. Therefore, the "lift effect" will be generated in accordance with Bernoulli principle. It

should be noted that the lift force and tube velocity are in the same direction. So this “lift effect” provides a negative damping for the tube. Obviously, the pitch flow velocity also has a strong influence on the magnitude of the “lift effect”. The fluidelastic instability occurs just because the “lift effect” is strong enough to overcome the structural damping of the tube as the pitch flow velocity reaches the critical velocity.

Influence of Tube Array Geometry on Coefficient β

The coefficient β can be rearranged as follows:

$$\beta = \left\{ \left(\frac{\sin\theta}{4} \sqrt{\left(\frac{H}{D} - \sin\theta\right)^2 + \frac{\cos^2\theta}{4}} + \frac{\theta\sin\theta}{3} \right) \left[\frac{\left(\frac{P}{D} - 1\right)}{\left(\frac{P}{D} - \cos\theta + \frac{x_c}{D}\right)^2} + \frac{\left(\frac{P}{D} - 1\right)}{\left(\frac{P}{D} - \cos\theta - \frac{x_c}{D}\right)^2} \right] + \frac{\theta\sin\theta}{6} \left[\frac{\left(\frac{P}{D} - 1\right)}{\left(\frac{P}{D} - 1 + \frac{x_c}{D}\right)^2} + \frac{\left(\frac{P}{D} - 1\right)}{\left(\frac{P}{D} - 1 - \frac{x_c}{D}\right)^2} \right] \right\}^{-1}$$

where θ is pressure acting angle, x_c/D is tube amplitude ratio, P/D is transverse tube pitch ratio, and H/D is streamwise tube pitch ratio.

Obviously, the pressure acting angle, tube amplitude ratio, transverse tube pitch ratio, and streamwise tube pitch ratio are four factors affecting the coefficient β . The pressure acting angle is an empirical constant which should be determined by experiments (here the author estimates roughly a range of angle $25^\circ \sim 45^\circ$).

The transverse tube pitch ratio and streamwise tube pitch ratio are relevant to the tube array geometry and tube diameter which are primary design parameters. The tube amplitude ratio is typically about 0.01 or less at instability. Assuming values for the amplitude ratio and pressure acting angle of 0.01 and 35° respectively, the effect of transverse and streamwise pitch ratio on the stability coefficient β can be determined. The normal triangular array of bare tubes in the present study is used as a reference point. The relationship of the transverse tube pitch and streamwise tube pitch against the coefficient β can be plotted as shown in Figure A-4.

The coefficient β will decrease as the transverse pitch ratio increases and increase as the streamwise pitch ratio increases. It is also shown that the coefficient will decrease when the permitted tube amplitude ratio increases.

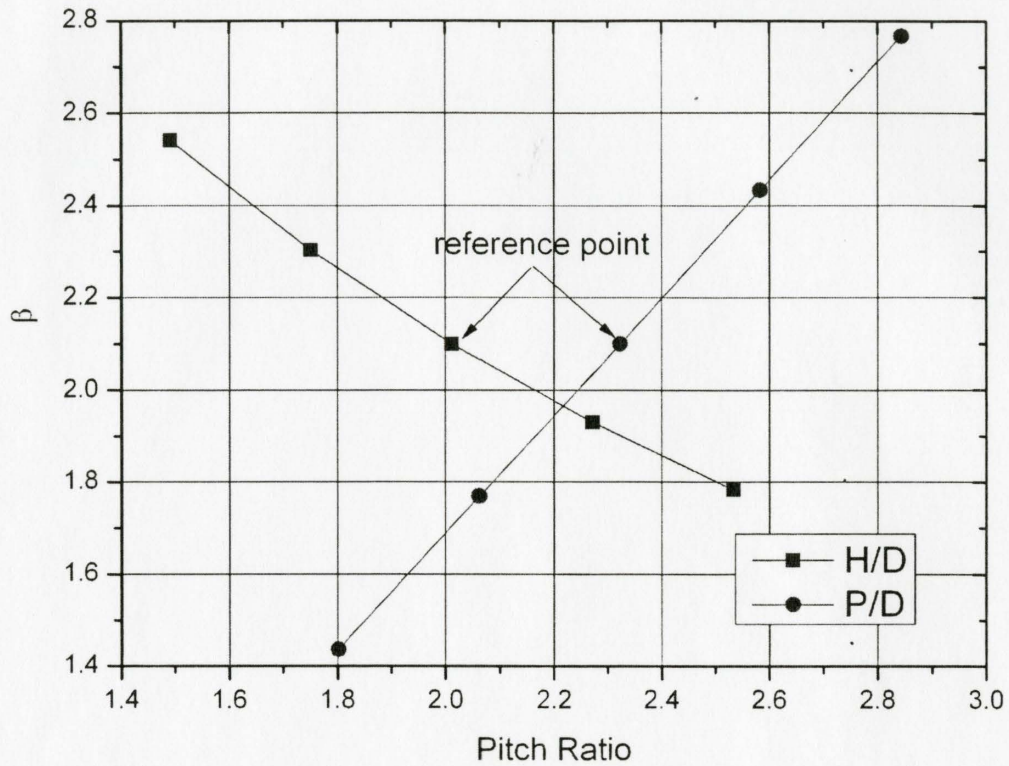


Figure A-4 Influence of Tube Array Geometry on Coefficient β
for $x_c/D=0.01$ and $\theta=35^\circ$

Influence of Fluid Stiffness Component on Tube Vibration

Similarly, one can investigate how the first term of the right hand side of the FVE influences the oscillation of a single flexible tube array. Assuming the net tube damping is close to zero due to the velocity mechanism, the FVE is further reduced to:

$$\frac{\partial^2 \hat{x}_c}{\partial \tau^2} + \hat{x}_c = -\hat{k}_f \times \hat{\alpha}$$

Noting that:

$$\hat{\alpha} = a \times \left\{ \begin{array}{l} E_1 \left[\left(\frac{1}{1+\hat{x}_c} \right)^2 - \left(\frac{1}{1-\hat{x}_c} \right)^2 \right] + E_2 \left[\left(\frac{1}{b+\hat{x}_c} - \frac{1}{1+\hat{x}_c} \right) \frac{1}{1+\hat{x}_c} - \left(\frac{1}{b-\hat{x}_c} - \frac{1}{1-\hat{x}_c} \right) \frac{1}{1-\hat{x}_c} \right] \\ + E_3 \left[\left(\frac{1}{b+\hat{x}_c} - \frac{1}{1+\hat{x}_c} \right)^2 - \left(\frac{1}{b-\hat{x}_c} - \frac{1}{1-\hat{x}_c} \right)^2 \right] \end{array} \right\}$$

Since \hat{k}_f is a very small parameter and $\hat{\alpha}$ is a function of \hat{x}_c , the above equation is typically a weakly nonlinear free vibration equation in the form of :

$$\frac{\partial^2 \hat{x}_c}{\partial \tau^2} + \hat{x}_c = sf(\hat{x}_c)$$

where s is a small real constant and $f(\hat{x}_c)$ is a nonlinear function of \hat{x}_c .

Methods for solving weakly nonlinear vibration equations include the perturbation method, mean method and KMD method, etc. The harmonic linearization method based on the mean method is briefly discussed here. For the above weakly nonlinear free vibration equation, the solution of its derivate system is given by:

$$\hat{x}_c = c \cos(\tau - \varphi) = c \cos \psi$$

$$\text{and } \frac{d\hat{x}_c}{d\tau} = -c \sin(\tau - \varphi) = -c \sin \psi$$

If c and φ are functions of time and s is small enough, according to the mean method, the differential equations for c and φ are given as follows:

$$\begin{aligned} \frac{dc}{d\tau} &= -\frac{s}{2} Q(c, \varphi) \\ \frac{d\varphi}{d\tau} &= \frac{s}{2c} P(c, \varphi) \end{aligned}$$

where P and Q are defined as:

$$\begin{aligned} P(c, \varphi) &= \frac{1}{\pi} \int_0^{2\pi} f(c \cos \psi) \cos \psi d\psi \\ Q(c, \varphi) &= \frac{1}{\pi} \int_0^{2\pi} f(c \cos \psi) \sin \psi d\psi \end{aligned}$$

If the higher harmonics are neglected, in accordance with the harmonic linearization method, the nonlinear function $f(\hat{x}_c)$ can be written as:

$$\begin{aligned} f &= P(c, \varphi) \cos \psi + Q(c, \varphi) \sin \psi \\ &= \frac{P(c, \varphi)}{c} \hat{x}_c - \frac{Q(c, \varphi)}{c} \frac{d\hat{x}_c}{d\tau} \end{aligned}$$

The weakly nonlinear free vibration equation can be linearized as:

$$\frac{\partial^2 \hat{x}_c}{\partial \tau^2} + \left[\frac{sQ(c, \varphi)}{c} \right] \frac{d\hat{x}_c}{d\tau} + \left[1 - \frac{sP(c, \varphi)}{c} \right] \hat{x}_c = 0$$

Since the nonlinear function in the present theory is complex, the procedure to obtain the solution of the linearized equation will not be discussed further. The solution for the weakly nonlinear free vibration for the fluidelastic force will be studied in the future.

A5 Numerical Method to FVE

To solve the FVE equation matrix analytically for the whole tube array is very difficult. Fortunately, a numerical method could be applied. However, the numerical algorithm should be carefully selected since the fluid force is nonlinear and the numerical solutions of the equation set are tricky in convergence. All explicit methods, including Runge-Kutta, Adams PECE, and Euler explicit method, etc., have been proven to diverge in this case. Only the modified Euler method can be applied to solve the equation set at present. Perhaps the additive semi implicit Runge-Kutta method could do so and have higher accuracy but it is much more complicated than the modified Euler method. So, personally, I believe the most stable and simplest numerical algorithm to solve the equation set is the modified Euler method, which is an implicit algorithm with the second order.

For a vibration equation:

$$\frac{\partial^2 x_c}{\partial t^2} + \frac{c}{m} \frac{\partial x_c}{\partial t} + \frac{k}{m} x_c = f(t, x_c, x'_c)$$

The second order differential equation can be converted into two first order equations by

defining:

$$y_1 = \frac{\partial x_c}{\partial t}$$

$$y_2 = x_c$$

Then, the vibration equation becomes:

$$\frac{\partial y_1}{\partial t} + \frac{c}{m} y_1 + \frac{k}{m} y_2 = f(t, y_1, y_2)$$

$$\frac{\partial y_2}{\partial t} = y_1$$

According to the modified Euler method, we have:

The Predictor:

$$\tilde{y}_1^{n+1} = y_1^n + dt \times \left[f(t, y_1^n, y_2^n) - \frac{c}{m} y_1^n - \frac{k}{m} y_2^n \right]$$

$$\tilde{y}_2^{n+1} = y_2^n + dt \times y_1^n$$

The Corrector:

$$y_1^{n+1} = y_1^n + \frac{dt}{2} \times \left\{ \left[f(t, y_1^n, y_2^n) - \frac{c}{m} y_1^n - \frac{k}{m} y_2^n \right] + \left[f(t, \tilde{y}_1^{n+1}, \tilde{y}_2^{n+1}) - \frac{c}{m} \tilde{y}_1^{n+1} - \frac{k}{m} \tilde{y}_2^{n+1} \right] \right\}$$

$$y_2^{n+1} = y_2^n + \frac{dt}{2} \times (y_1^n + \tilde{y}_1^{n+1})$$

In this case, the tubes in the first row are fixed, as well as the ones on both sides (See Figure A-5). The others are flexible and their displacements and phases are tiny random values initially in order to simulate the effect of turbulence. Then by solving the discrete vibration equation for each free tube, the velocities and displacements of these tubes are recorded under a given fluid flow rate. Increasing the flow rate until the critical reduced velocity is found. The relative parameters are listed in Table A-1. The C code is also attached as Appendix B. Some results are also shown in Figure A-6.

Table A-1 Specifications for Numerical Computation

θ	H	P	D	x_{cmax}	m	ρ	δ
60	0.07725	0.0892	0.0383	0.1D	4.204	1.225	0.006

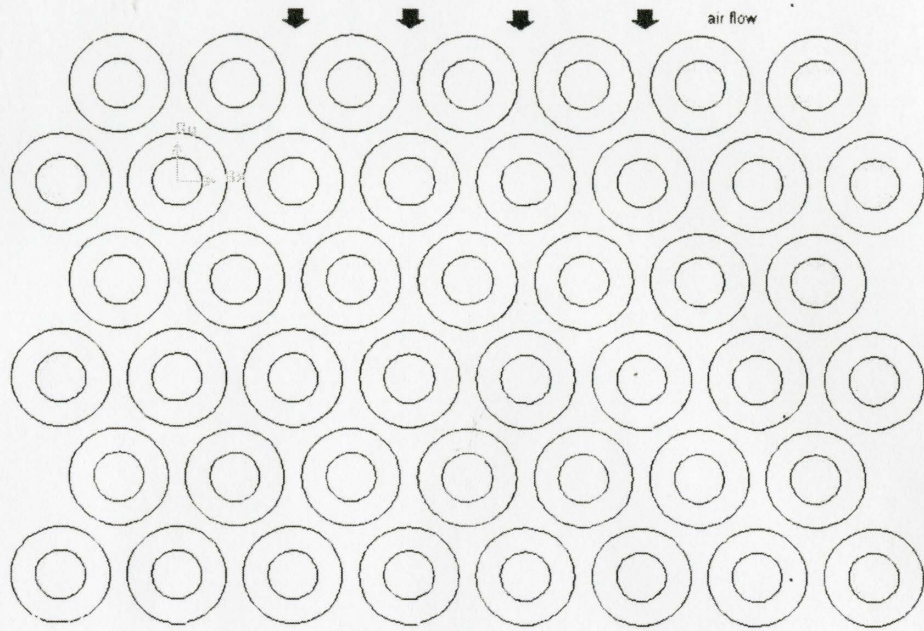
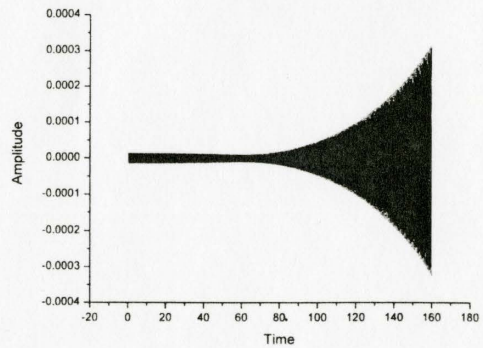
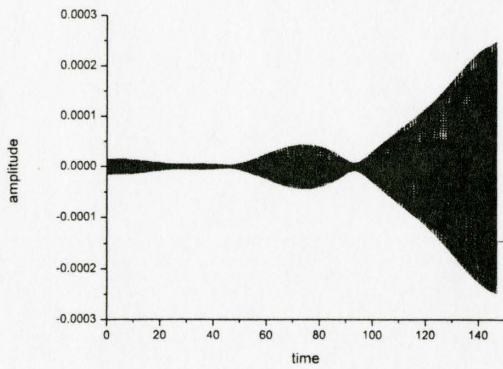
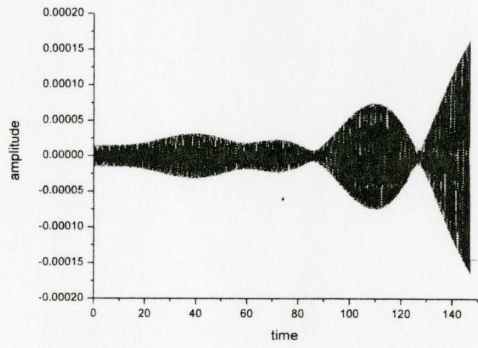
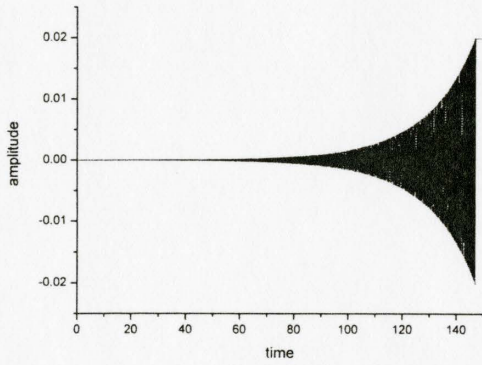
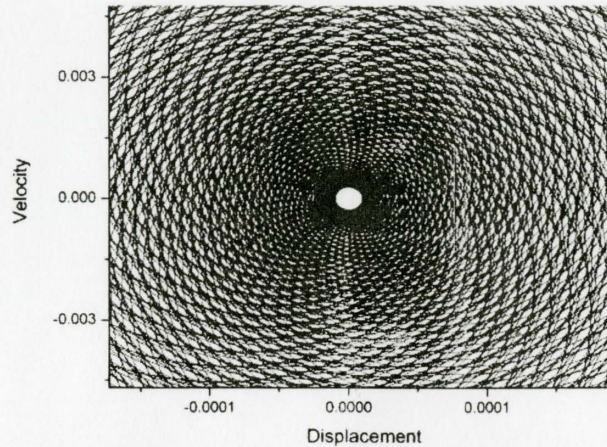


Figure A-5 Triangle Tube Array



Amplitude vs. Time



Velocity vs. Displacement

Figure A-6 Some Numerical Computation results

Since the time is limited, no more detailed insights into the numerical prediction of the critical reduced velocity are provided here.

A6 Comparisons with Present Analytical Model and Other Empirical Formulae

Finally we compare the experiment data with the new analytical model in the present study and with empirical equations recommended by Weaver and Fitzpatrick, as well as Connors. The empirical formula recommended by Weaver and Fitzpatrick ^[8] are for the lower bounds of tube instability shown here in Table A-2.

Table A-2 Equations for Prediction ^[8]

Array geometry	$m\delta_a/\rho d^2 < 0.3$	$m\delta_a/\rho d^2 > 0.3$
Square	$V_p/fd = 1.4$	$V_p/fd = 2.5 (m\delta_a/\rho d^2)^{0.48}$
Rotated square	$V_p/fd = 2.2$	$V_p/fd = 4.0 (m\delta_a/\rho d^2)^{0.48}$
Normal triangle	$V_p/fd = 2.0$	$V_p/fd = 3.2 (m\delta_a/\rho d^2)^{0.40} *$
Parallel triangle	$V_p/fd = 1.0$	$V_p/fd = 4.8 (m\delta_a/\rho d^2)^{0.30}$

Blevins recommended in his book ^[2] that

* There is a printing error. The exponent should be 0.46 not 0.40, according to Dr. D.S. Weaver.

$$\left(\frac{U_g}{fD}\right)_{cr} = \beta \left(\frac{m\delta}{\rho D^2}\right)^{1/2}$$

where β is 2.4 for 90% lower bound and 4.0 for mean value regardless of the tube arrangement.

The current analytical model is

$$\left(\frac{U_g}{fD}\right)_{cr} = \beta \left(\frac{m\delta}{\rho D^2}\right)$$

where

$$\beta = \left\{ \left(\frac{\sin\theta}{4} \sqrt{\left(\frac{H}{D} - \sin\theta\right)^2 + \frac{\cos^2\theta}{4}} + \frac{\theta\sin\theta}{3} \right) \left[\frac{\left(\frac{P}{D} - 1\right)}{\left(\frac{P}{D} - \cos\theta + \frac{x_c}{D}\right)^2} + \frac{\left(\frac{P}{D} - 1\right)}{\left(\frac{P}{D} - \cos\theta - \frac{x_c}{D}\right)^2} \right] \right\}^{-1} + \frac{\theta\sin\theta}{6} \left[\frac{\left(\frac{P}{D} - 1\right)}{\left(\frac{P}{D} - 1 + \frac{x_c}{D}\right)^2} + \frac{\left(\frac{P}{D} - 1\right)}{\left(\frac{P}{D} - 1 - \frac{x_c}{D}\right)^2} \right]$$

To apply the concept of effective diameter so that the comparisons are under the same mass damping parameter, set D equal to D_{eff} . The author can then compare the experimental data with model predictions in a practical way. The known conditions for the current analytical model are listed in Table A-3. For a given triangle tube array, the predictions of the critical reduced velocity given by the above relationship are shown in Table A-4.

Table A-3 Parameters for Current Analytical Model

	x_c / D_{eff}				H / D_{eff}	P / D_{eff}	θ (rad)	δ	m (kg/m)	ρ (kg/m ³)
BT	0.05	0.1	0.2	0.3	2.533	2.323	0.61	0.0031	4.059	1.195
CFT	0.05	0.1	0.2	0.3	1.740	2.009	0.61	0.0056	6.354	1.178
FFT	0.05	0.1	0.2	0.3	1.500	1.732	0.61	0.0075	8.314	1.175

Table A-4 Model Predictions

	mass damping	$\beta_{0.05}$	$\beta_{0.1}$	$\beta_{0.2}$	$\beta_{0.3}$	Current model			
BT	7.141	1.779	1.761	1.688	1.275	12.70	12.57	12.06	11.24
CFT	15.322	1.861	1.829	1.706	1.240	28.51	28.02	26.14	23.24
FFT	20.009	1.598	1.549	1.366	1.107	31.98	31.00	27.34	22.00

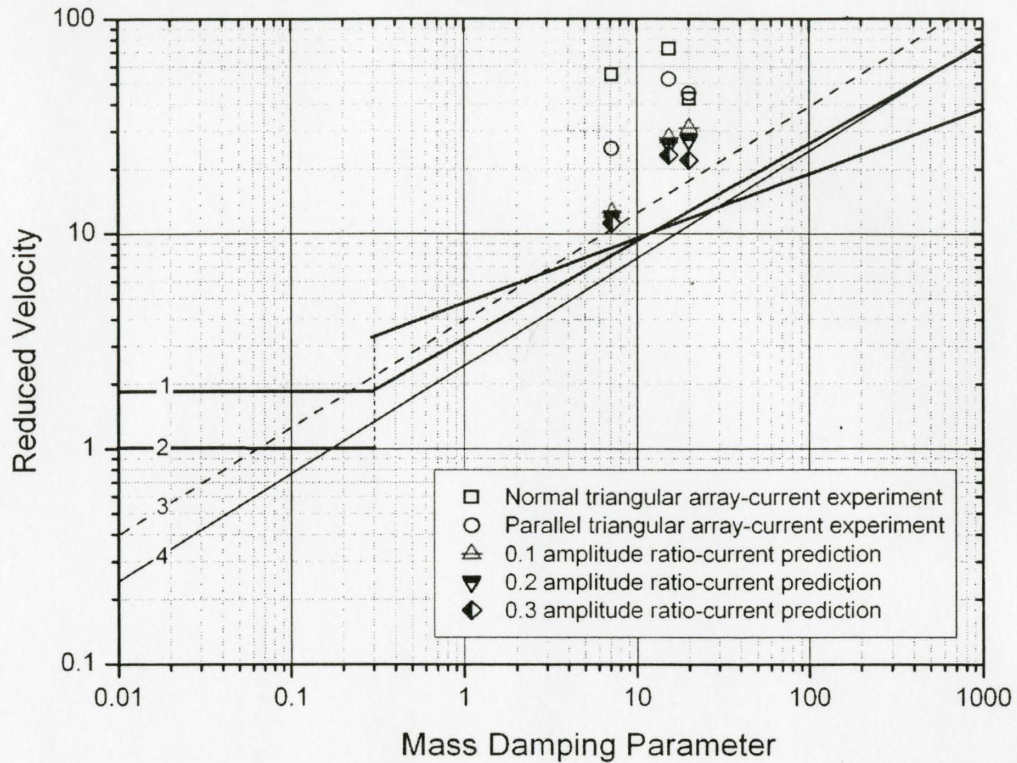


Figure A-7 Experimental Data vs. Analytical Model and Empirical Equations

The comparisons between the experimental data, the current model predictions, and other empirical equation results are shown in Figure A-7. The experimental data for normal triangle and parallel triangle arrays are put together in the same figure. Line 1 is for the lower bound of the normal triangle arrangement while line 2 is for the parallel triangle arrangement as recommended by Weaver and Fitzpatrick ^[8]. The dash line 3 is for the mean value of the world data for all arrays and Line 4 is recommended by Blevins ^[2]. It can be seen that the empirical predictions ^{[2][8]} are linear and much lower compared with the experimental results. The current predictions are higher than the mean value of the world data for all arrays, but lower than the current experimental data. The most interesting thing is that the current analytical prediction presents a nonlinear behavior especially when the amplitude ratio is larger than a value of 0.3, which shows a reasonable agreement with the experimental data.

A7 Lift Effect and Negative Damping Alleviation Experiments

As discussed above, the lift effect plays a vital role in the negative damping of the tube. It could be very beneficial if the relationship of the lift effect as a function of the pitch flow velocity could be determined by experiment. To do so, the author designed a "lift effect" experiment as shown in Figure A-8. Two wings are added to the tube to increase the lift effect, even though these wings are generally thought to increase the damping of the tube due to "windage effect". The plates in front of and behind the tube equally divide the flow channel into two parts. So, the mass fluxes in both sub-channels are the same. If the "lift effect" does work, the tube vibration response will increase as the air flow velocity increases, and it is expected that the critical velocity will be inversely proportional to the wingspan.

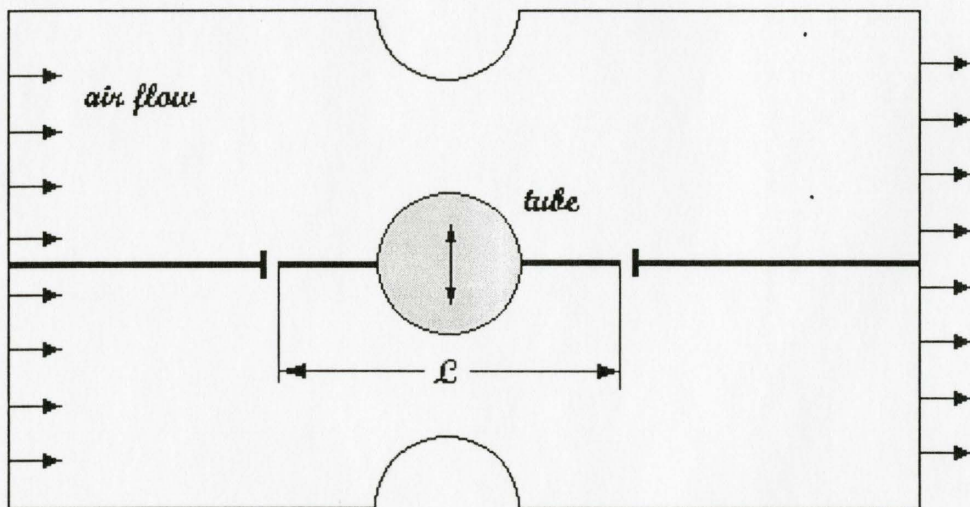


Figure A-8 Schematic Diagram of Lift Effect Experiment

Coincidentally, there is a published paper by Weaver and his coauthors ^[24] which conducted an experiment to test the effect of platen fins on the flow-induced vibrations of an in-line tube array. Figure A-9 shows the test section for the platen finned tube array. Figure A-10 shows the test results. The critical velocity of the platen finned tube array is significantly lower than the one of the smooth tube array. The vortex shedding vanishes due to the platen fin separating the flow

channel into two sub-channels. The turbulence buffeting can not induce the fluidelastic instability. The only explanation is the existence of "lift effect". Unfortunately, this experiment is not designed for the "lift effect". If the wingspan of the platen fin tube were able to be changed, the correlation of the "lift effect" against the wingspan would be obtained.

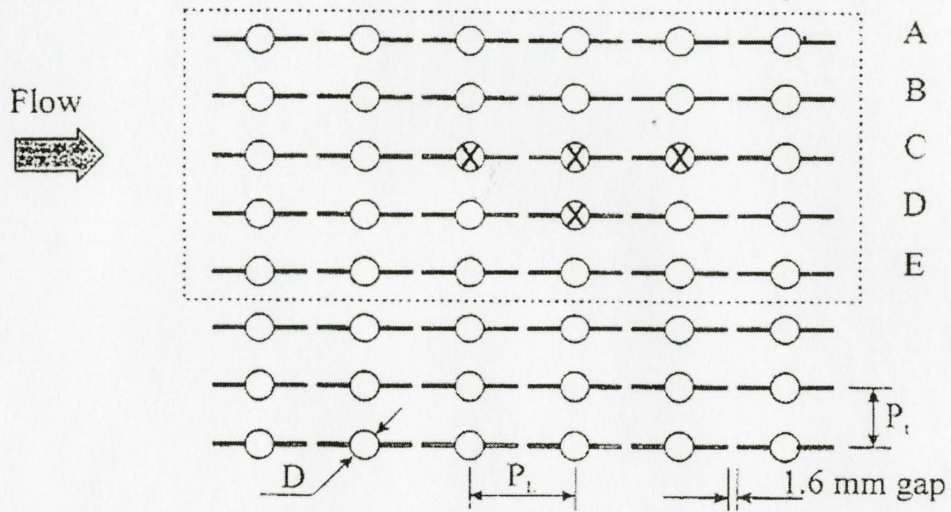


Figure A-9 Test Section of Platen Finned Tube Array [24]

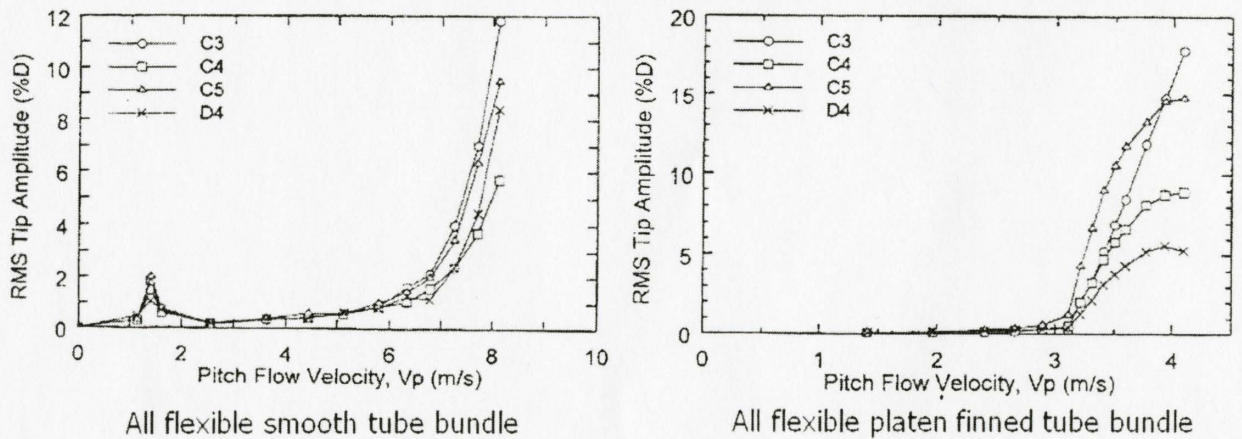


Figure A-10 Critical Velocities of Smooth Tubes and Platen Finned Tubes [24]

It is also important to alleviate the negative damping of the tubes in order to improve the fluidelastic stability of a tube bundle. Using energy of the oncoming flow with a position of it being passed through inner body ducts from leading to back surfaces is a possible method to reduce the lift force amplitude. Figure A-11 shows two possible duct designs to alleviate the

negative damping of the tube.

The sensitivity of the aerodynamics characteristics of bodies in crossflow to duct flow rate as well as to positions of jets ejected into the near flow wake needs detailed experimental and numerical investigations.

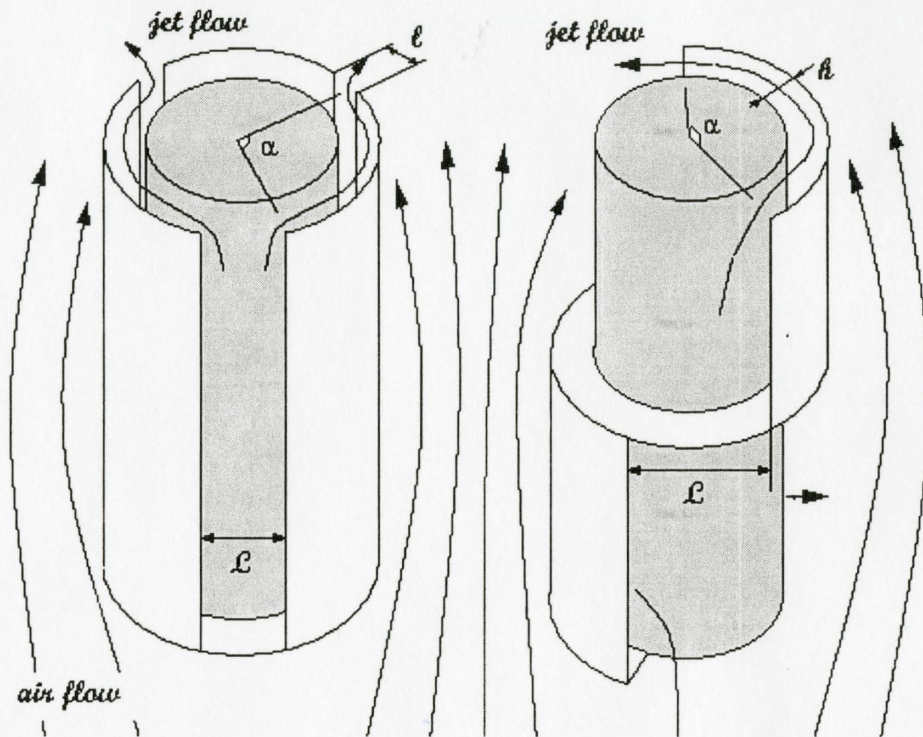


Figure A-11 Duct Jet Flow

A8 Conclusions and Recommendations

A mathematical model of fluidelastic instability in finned tube bundles was developed to predict the critical reduced velocity in the project. Some conclusions are drawn here

- 1) A fluidelastic vibration equation is obtained by the current theory and a new dimensionless number is defined as the dimensionless stiffness of fluid flow.
- 2) A new correlation of critical reduced velocity against mass damping parameter is obtained to

predict the fluidelastic instability of tube bundles in staggered arrangement. The correlation coefficient β depends on the tube transverse pitch ratio, streamwise pitch ratio, pressure acting angle, and tube amplitude ratio. The analytical results are in reasonable agreement with the current experimental data.

- 3) The modified Euler method was used to solve the FVE in the whole tube array. But more studies should be conducted to get more detailed results.

Recommendations

- 1) The weakly nonlinear free vibration equation for the fluidelastic force needs further investigation which may provide insights into the tube vibration behavior when the system damping is close to zero.
- 2) An experiment has been designed to investigate the “lift effect” of a tube in the future.
- 3) Experimental and numerical studies are also suggested to investigate the aerodynamics characteristics of duct jet flow which may alleviate the negative damping of the tube.

APPENDIX B

C Code for 2 D Fluid elastic Instability Prediction of Triangular Tube Arrays

```
/******  
2 degree Fluidelastic Instability Prediction of Triangular Tube Arrays  
modified implicit Euler method  
predictor: y[p]=y[n]+f(time[n],y[n])*dtime  
corrector: y[n+1]=y[n]+[f(time[n],y[n])+f(time[n+1],y[p])*dtime/2  
*****/  
#include <stdio.h>  
#include <stdlib.h>  
#include <string.h>  
#include <math.h>  
#define theta M_PI/3.0          /* angle at the seperation point */  
#define den 1.225              /* air density kg/m^3 */  
#define E 201e9                /* Young's Modulus of Elasticity of Tube, Pa */  
#define IXX 3.22e 10  
/* Geometrical Moment of Inertia of Tube, m^4, i.e. for a round section, it is given by PI*d^4/64,  
in this case, d is 9.0mm */  
#define Rho 4.204              /* Mass of Unit Length of Tube, kg/m */  
#define L 0.268                /* L is the tube rod length, which is 268mm in this case */  
#define Delta 0.003*2         /* Damping of Tube, which can be measured by test */  
#define K E*IXX/L/L/L  
/* Stiffness of Tube, kg/ms^2, i.e. for a cantilever, it is given by E*I/L^3.*/  
#define Wr 2*M_PI*4.5  
/* First Order Natural Frequency of Tube, rad/s, i.e. for a cantilever with a concentrated mass at  
its free end, it can be computed by sqrt(K/(M+0.2357ml)), where M is the concentrated mass and  
ml is mass of cantilever. if f is given, then Wr is given by 2*PI*f */  
#define Am 0.020              /* the maximum possible amplitude of tube, m */  
#define P 0.0892              /* tube pitch m */  
#define H 0.077249            /* longitude space m */  
#define D 0.0383              /* diameter of tube m */  
#define Ug 1.5                /* air flow velocity across the minimum gap m/s */  
/* the x coordinates of tube */  
static float  
CGC[28]={0.0,0.0892,0.1784,0.2676,0.3568,0.446,0.0446,0.1338,0.223,0.3122,0.4014,0.0,0.089  
2,0.1784,0.2676,0.3568,0.446,0.0446,0.1338,0.223,0.3122,0.4014,0.0,0.0892,0.1784,0.2676,0.35  
68,0.446,};  
static float Vel_pre[28];  
static float V_pre[28];  
static float X_pre[28];
```

```

static float F_pre[28];
/* Modified Implicit Euler Algorithm */
int MIEA(X,V,F,dt,k)
float X,V,F,dt;
int k;
{
    int i;
    float V_next,X_next,dF;
/* predictor */
    V_next=V+dt*(F V*Delta X*K)/Rho; /* f1=(fx x1*Delta/Rho x2*K/Rho) */
    X_next=X+dt*V; /* f2=x1 */
/* corrector */
    dF=F F_pre[k];
    for(i=0;i<3;i++){
        V_next=V+0.5*dt*((F V*Delta X*K)+(F+2.5*dF V_next*Delta X_next*K))/Rho;
        X_next=X+0.5*dt*(V+V_next);
        if(V_next>Wr*Am){
            printf("the amplitude is too big... the proceed is terminated!");
            return 1;
        }
    }
    V_pre[k]=V_next; X_pre[k]=X_next;F_pre[k]=F;
}
main()
{
    int i,j,rm,n=5;
    float time,dt;
    float *r,rs,ru,rv,s,am; /* generating random float_point values between [0,1] */
    float CGX[28],CGV[28],CGF[28]; /* displacement, velocity and force of tube array */
    float kl12,kl13,kr12,kr13; /* coefficients of vibrating displacement */
    float E2,E3,E4,E5,E6; /* angle coefficients */
    float NE,WN,CW,C,CE; /* the four vibrating displacements neighbouring to the centre tube */
    float Dis,Vel,DV,Q;
    char str[8];
    FILE *fp[28];
/* initializing time, displacement, velocity and force */
    time=0.0;dt=0.01;
    for(i=0;i<28;i++){CGX[i]=0.0;CGV[i]=0.0;CGF[i]=0.0;}
/* initializing the displacement and position of each tube */
    rs=65536;ru=2053.0;rv=13849.0;am=0.0001;
/* am is the assumed initial tiny amplitude of tube */
    for(i=0;i<28;i++){

```

```

s=2.; r=&s; /* to obtain different random seed r by changing s value */
*r=ru*(r)+rv;rm=(int)(r/rs);*r=*r rm*rs;
CGX[i]=am*cos(2*M_PI*(r/rs));
CGV[i]=am*sin(2*M_PI*(r/rs));
CGC[i]=CGC[i]+CGX[i];
}
/* constant coefficient calculations */
E2=sin(theta); /* E2 */
E3=((2*theta*theta 4)*sin(theta)+4*theta*cos(theta))/(theta*theta); /* E3 */
E4=((theta*theta*theta*theta 12*theta*theta+24)*sin(theta)
+(4*theta*theta*theta 24*theta)*cos(theta))/theta/theta/theta/theta; /* E4 */
E5=sqrt((H D*sin(theta))*(H D*sin(theta))+D*D*cos(theta)*cos(theta)/4)*sin(theta); /* E5 */
E6=D*theta*sin(theta); /* E6 */
/* gap mass flow rate */
Q=den*Ug*(P D);
/*open files*/
for(i=0;i<28;i++){
printf(str,"%d",i+1); strcat(str,".txt");
if((fp[i]=fopen(str,"a"))==NULL){printf("Cannot open the file!"); break;}
}
/* time step begin */
for(j=0;j<10000;j++){
/* Calculating the force on a tube */
for(i=0;i<28;i++){
/* first row */
if(i<6){
WN=0.0;NE=0.0;
if(i==0){CW=0.0;C=CGX[1];CE=CGX[2];}
else if(i==5){CW=CGX[4];C=CGX[5];CE=0.0;}
else {CW=CGX[i 1];C=CGX[i];CE=CGX[i+1];}
}
/* second row */
else if(i>5&&i<11){
WN=CGX[i 6];NE=CGX[i 5];
if(i==6){CW=0.0;C=CGX[6];CE=CGX[7];}
else if(i==10){CW=CGX[9];C=CGX[10];CE=0.0;}
else {CW=CGX[i 1];C=CGX[i];CE=CGX[i+1];}
}
/* third row */
else if(i>10&&i<17){
WN=CGX[i 6];NE=CGX[i 5];

```

```

    if(i==11){WN=0.0;CW=0.0;C=CGX[11];CE=CGX[12];}
    else if(i==16){NE=0.0;CW=CGX[15];C=CGX[16];CE=0.0;}
    else {CW=CGX[i 1];C=CGX[i];CE=CGX[i+1];}
}
/* fourth row */
else if(i>16&& i<22){
    WN=CGX[i 6];NE=CGX[i 5];
    if(i==17){CW=0.0;C=CGX[17];CE=CGX[18];}
    else if(i==21){CW=CGX[20];C=CGX[21];CE=0.0;}
    else {CW=CGX[i 1];C=CGX[i];CE=CGX[i+1];}
}
/* fifth row */
else {
    WN=CGX[i 6];NE=CGX[i 5];
    if(i==22){WN=0.0;CW=0.0;C=CGX[22];CE=CGX[23];}
    else if(i==27){NE=0.0;CW=CGX[26];C=CGX[27];CE=0.0;}
    else {CW=CGX[i 1];C=CGX[i];CE=CGX[i+1];}
}
kl12=(P D*cos(theta)+NE WN)/(P D*cos(theta)+C CW); /* kl1 2*/
kl13=(P D*cos(theta)+NE WN)/(P D+C CW); /* kl1 3*/
kr12=(P D*cos(theta)+NE WN)/(P D*cos(theta)+CE C); /* kr1 2*/
kr13=(P D*cos(theta)+NE WN)/(P D+CE C); /* kr1 3*/
Dis=0.5*Ug*(P D)*D/(P D*cos(theta)+NE WN)/(P D*cos(theta)+NE WN);
Dis=Dis*(E2*(kl13*kl13 kr13*kr13)+E3*((kl12 kl13)*kl13 (kr12 kr13)*kr13
+E4*((kl12 kl13)*(kl12 kl13) (kr12 kr13)*(kr12 kr13)));
Vel=(E5+E6/3)*(kl12 kr12)+2*E6*(kl13 kr13)/3;
Vel=0.5*Vel*D/(P D*cos(theta)+NE WN);
DV=(Vel Vel_pre[i])/dt; Vel_pre[i]=Vel;
CGF[i]= (Dis+DV)*Q; /* fluid force */
/* computing the displacement and velocity of tube */
rm=MIEA(CGX[i],CGV[i],CGF[i],dt,i);
if(rm== 1)break;
}
for(i=0;i<28;i++){CGV[i]=V_pre[i];CGX[i]=X_pre[i];CGF[i]=F_pre[i];}
/* write data file */
if(j==n){
    for(i=0;i<28;i++)fprintf(fp[i], "%f %f %f %f\n", time, V_pre[i],X_pre[i],F_pre[i]);
    n=n+2;
}
time=time+dt; }
for(i=0;i<28;i++)fclose(fp[i]); }

```

APPENDIX C

APDL Mac Code for Modal Analysis of Finned Tubes

```
/CLEAR
/BATCH
/COM,ANSYS RELEASE 10.0  UP20050718  11:19:36  06/18/2008
/input,menust,tmp, " ,,,,,,,,,,,,,,1
/GRA,POWER
/GST,ON
/PLO,INFO,3
/GRO,CURL,ON
/CPLANE,1
/REPLOT,RESIZE
WPSTYLE,,,,,,,,,0
!*
/NOPR
/PMETH,OFF,0
KEYW,PR_SET,1
KEYW,PR_STRUC,1
KEYW,PR_THERM,0
KEYW,PR_FLUID,0
KEYW,PR_ELMAG,0
KEYW,MAGNOD,0
KEYW,MAGEDG,0
KEYW,MAGHFE,0
KEYW,MAGELC,0
KEYW,PR_MULTI,0
KEYW,PR_CFD,0
/GO
!*
!* /COM,Preferences for GUI filtering have been set to display:
!*/COM,  Structural
!*
/PREP7
!*
ET,1,SOLID95
!*
ET,2,SOLID92
!*
MPTEMP,,,,,,,,
MPTEMP,1,0
```

```

MPDATA,EX,1,,2.05e8
MPDATA,PRXY,1,,0.27
MPTEMP,,,,,,,,
MPTEMP,1,0
MPDATA,DENS,1,,7800e-9
MPTEMP,,,,,,,,
MPTEMP,1,0
MPDATA,EX,2,,2.05e8
MPDATA,PRXY,2,,0.27
MPTEMP,,,,,,,,
MPTEMP,1,0
MPDATA,DENS,2,,7218e-9
!*
CYL4,0,0,8.2/2, , , ,230
CYL4,0,0,44.4/2, , , ,608
/VIEW,1,1,1,1
/ANG,1
/REP,FAST
FLST,3,1,6,ORDE,1
FITEM,3,2
VGEN, ,P51X, , , ,230, , ,1
/USER, 1
/VIEW, 1, 0.580036551737 , 0.460253656027 , -0.672104285630
/ANG, 1, 56.9178402033
/REPLO
CYL4,0,0,30.3/2, , , ,584-20
FLST,3,1,6,ORDE,1
FITEM,3,3
VGEN, ,P51X, , , ,242, , ,1
/VIEW, 1, 0.745290184201 , 0.634533961935 , -0.204717347787
/ANG, 1, 37.8091094399
/REPLO
VSBV, 2, 3
FLST,2,2,6,ORDE,2
FITEM,2,1
FITEM,2,4
VGLUE,P51X
LPLOT
/VIEW,1,,-1
/ANG,1
/REP,FAST

```

```

/AUTO,1
/REP,FAST
VPLOT
CM,_Y,VOLU
VSEL,, , 2
CM,_Y1,VOLU
CMSEL,S,_Y
!*
CMSEL,S,_Y1
VATT, 2, , 2, 0
CMSEL,S,_Y
CMDELE,_Y
CMDELE,_Y1
!*
CM,_Y,VOLU
VSEL,, , 1
CM,_Y1,VOLU
CMSEL,S,_Y
!*
CMSEL,S,_Y1
VATT, 1, , 1, 0
CMSEL,S,_Y
CMDELE,_Y
CMDELE,_Y1
!*
SMRT,6
SMRT,3
MSHAPE,1,3D
MSHKEY,0
!*
CM,_Y,VOLU
VSEL,, , 2
CM,_Y1,VOLU
CHKMSH,'VOLU'
CMSEL,S,_Y
!*
VMESH,_Y1
!*
CMDELE,_Y
CMDELE,_Y1
CMDELE,_Y2

```

```

!*
CM,_Y,VOLU
VSEL,,,, 1
CM,_Y1,VOLU
CHKMSH,'VOLU'
CMSEL,S,_Y
!*
VSWEEP,_Y1
!*
CMDELE,_Y
CMDELE,_Y1
CMDELE,_Y2
!*
/USER, 1
/VIEW, 1, 0.709104280551, -0.346523391917, -0.614078706811
/ANG, 1, -138.965361019
/REPLO
/ZOOM,1,SCRN,0.122393,-0.255195,0.229755,-0.302422
/UI,MESH,OFF
/AUTO,1
/REP,FAST
FINISH
/SOL
FLST,2,1,5,ORDE,1
FITEM,2,1
!*
/GO
DA,P51X,ALL,0
!*
ANTYPE,2
!*
MSAVE,0
!*
MODOPT,LANB,2
EQLV,SPAR
MXPAND,2,,0
LUMPM,0
PSTRES,0
!*
MODOPT,LANB,2,0,30,,OFF

```

APPENDIX D

Calibrations for Strain Gages

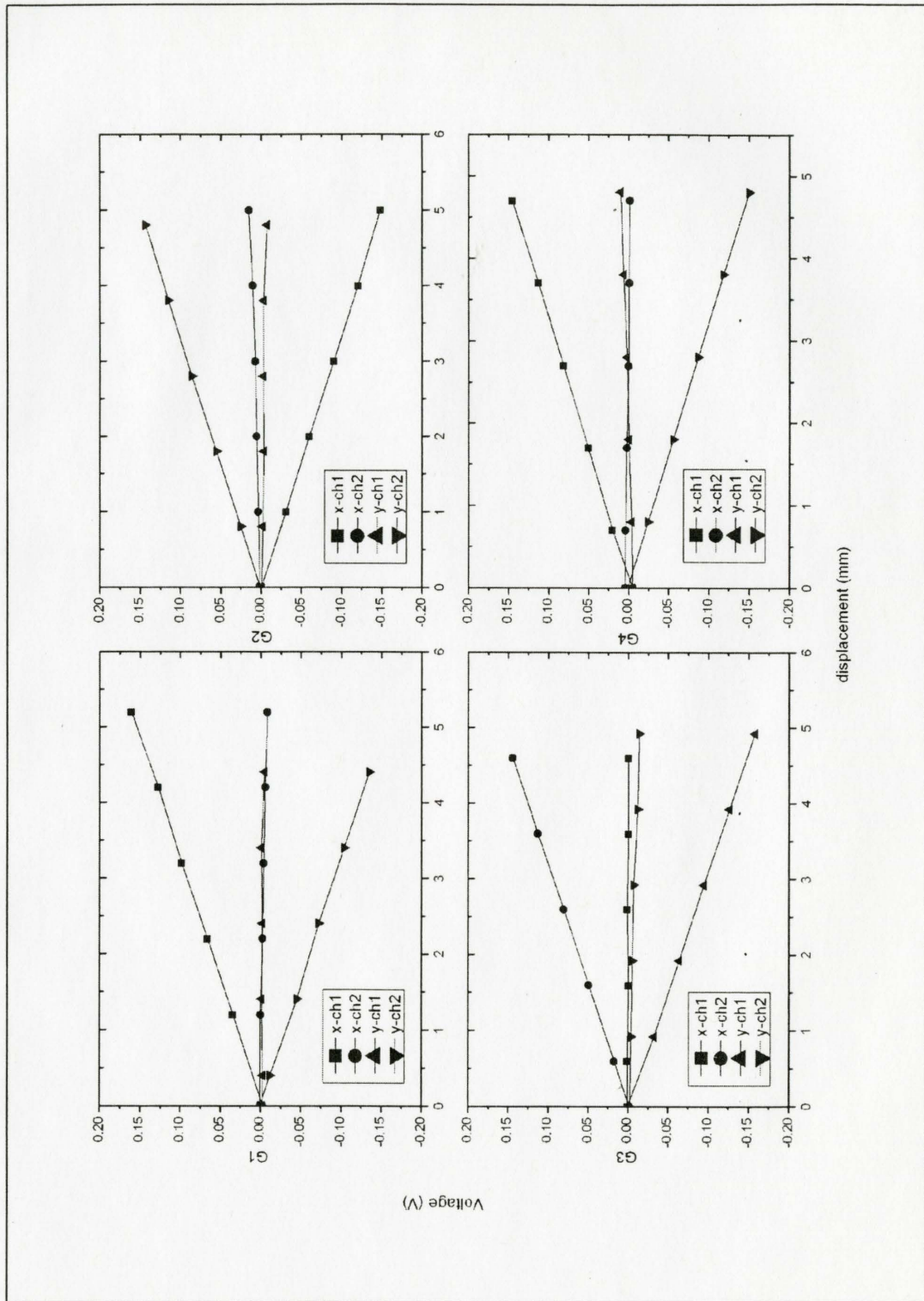


Figure D-1 Calibration of Strain Gages for Bare Tubes

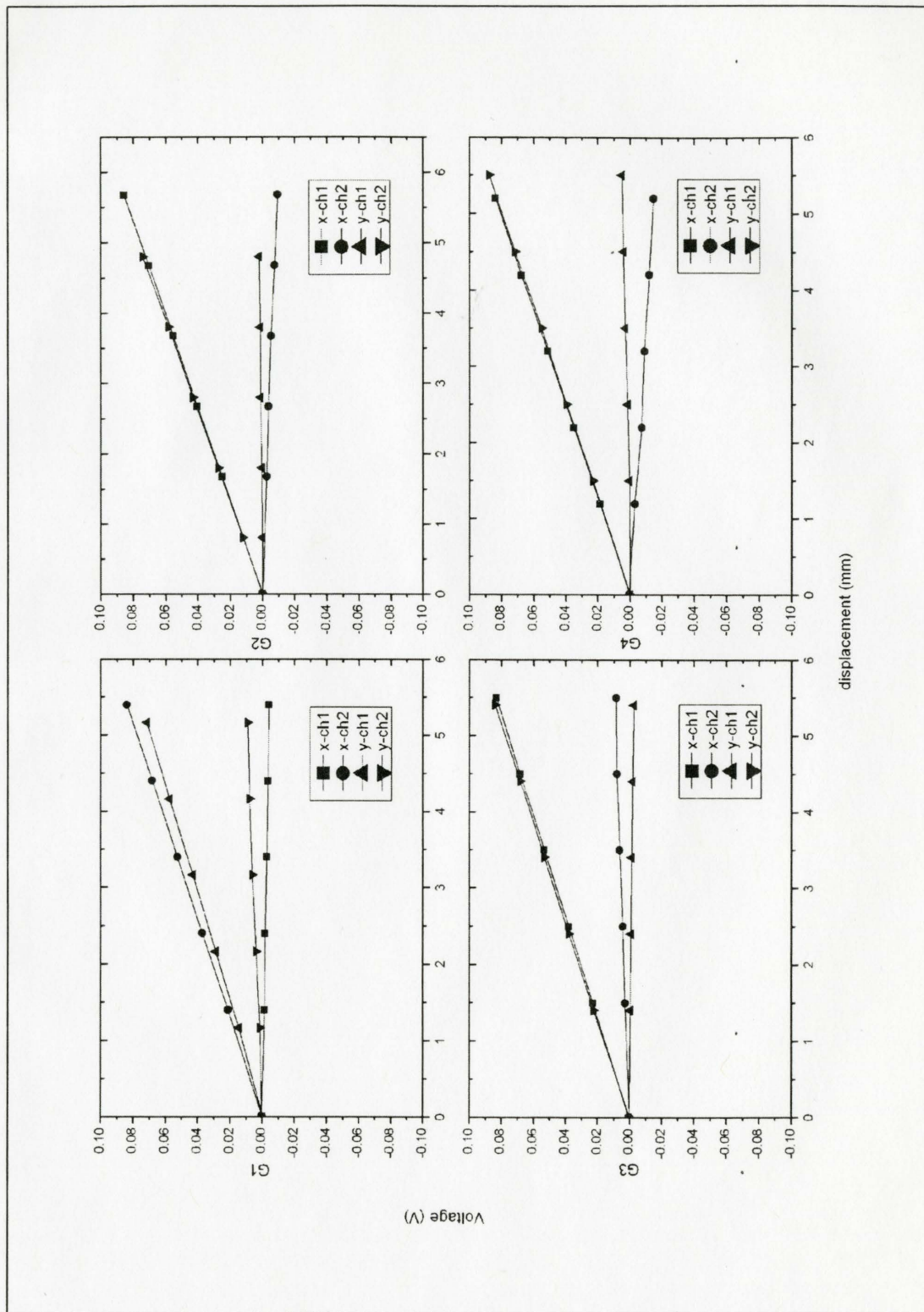


Figure D-2 Calibration of Strain Gages for Coarse Finned Tubes

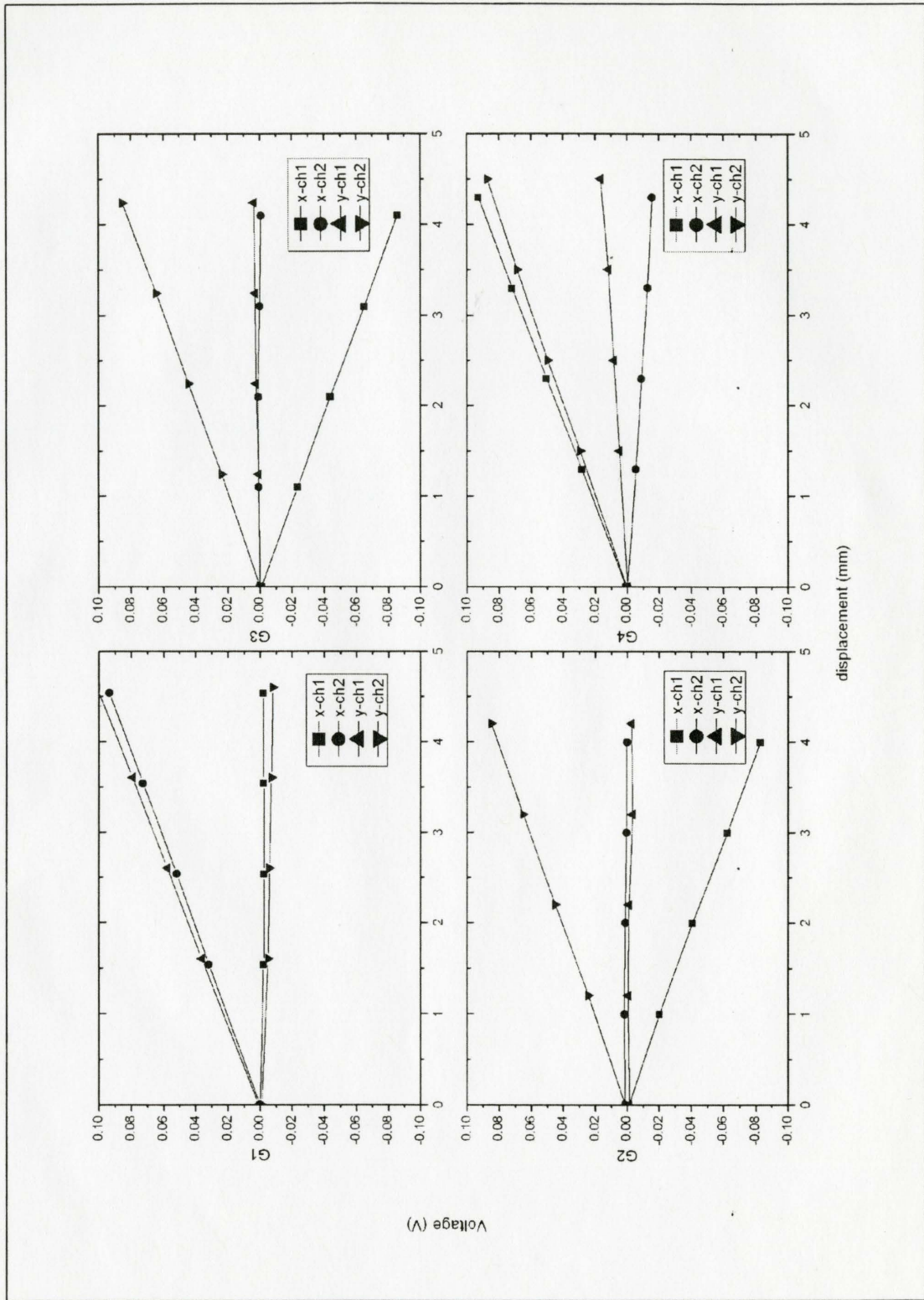


Figure D-3 Calibration of Strain Gages for Fine Finned Tubes